Nucleation at nano-structured substrates

vorgelegt von
Diplom-Physiker
Constans Mathias Weber
geboren in Berlin

Von der Fakultät II – Mathematik und Naturwissenschaften
der Technischen Universität Berlin
zur Erlangung des akademischen Grades
Doktor der Naturwissenschaften
Dr. rer. nat.

vorgelegte Dissertation

Promotionsausschuss:

Vorsitzender:	Prof. Dr. Reinhard Schomäcker
Berichter / Gutachter:	Prof. Dr. Regine von Klitzing
Berichter / Gutachter:	Prof. Dr. Dr. h. c. Helmuth Möhwald

Tag der wissenschaftlichen Aussprache: 17.07.2012

Berlin 2012

D83

Die vorliegende Arbeit wurde unter Anleitung von Herrn Dr. Hans Riegler am Max-Planck-Institut für Kolloid- und Grenzflächenforschung in Potsdam-Golm angefertigt.

Zusammenfassung

Die vorgelegte Arbeit beschreibt ein Verfahren zur Herstellung von Aggregaten mit vorgegebener Größe und Anordnung mittels Aufschleudern (Spin-casting) auf festen Oberflächen. Die Größen der Aggregate sowie deren Abstände sind im Bereich von Nanometern. Die physikalischen Eigenschaften der für diesen Prozess wichtigen Schritte werden in den einzelnen Kapiteln sorgfältig untersucht und beschrieben.

Zuerst wird der Prozess des Aufschleuderns detailliert diskutiert. Zum ersten Mal konnte eine analytische Lösung für die Höhenabnahme während des Abschleuderns gefunden werden. Diese Lösung wurde experimentell durch Reflektometrie bestätigt und für die Simulation des idealen Aufschleuderprozesses genutzt, wobei insbesondere auf die Entwicklung von Konzentrationsgradienten innerhalb des fluiden Films geachtet wurde. Einfache Skalierungsgesetze für die wichtigsten physikalischen Parameter wurden gefunden. Zusätzlich wurde der Aufschleuderprozess analytisch gelöst und mit den Simulationsergebnissen verglichen. Experimentelle Ergebnisse von aufgeschleuderten C_{60} Fullerenen zeigen eine deutliche bimodale Verteilung. Die theoretischen Ergebnisse können genutzt werden, um die gefundene Verteilung durch eine invertierte Keimbildung zu erklären.

Weiterhin wurde der Gleichgewichtszustand von Tropfen an ebenen Substraten tiefgehend analysiert. Eine einfache Formel für die Berechnung der reduzierten Dreiphasen-Hamaker-Konstante aus dem makroskopischen Kontaktwinkel wird hergeleitet. Es wird gezeigt, dass der Trennungsdruck (Disjoining Pressure) durch die Van-der-Waals-Kraft zu einer Abweichung von der klassischen Young-Gleichung, die größen*un*abhängige Kontaktwinkel beschreibt, führt. Stattdessen werden größen*ab*hängige Kontaktwinkel hergeleitet und mit dem semi-klassischen Ansatz der Linienspannung verglichen. Experimentelle Daten für verschiedene Oberflächen zeigen in der Tat variierende Kontaktwinkel. Die Messwerte von Rasterkraft- und Rasterelektronenmikroskopie sind konsistent. Die Ergebnisse werden im hergeleiteten theoretischen Rahmen diskutiert und die resultierende effektive Hamaker-Konstante berechnet.

Zuletzt werden die Ergebnisse des Aufschleuderns und der Aggregatstabilität genutzt um die Anwendung von Nanometer großen Oberflächenmodifikationen für die Beeinflussung von Keimbildungsprozessen zu zeigen. Die optimalen Bedingungen für Größe und Abstand der Modifikationen für die nahezu perfekte Aggregation an den vorgegebenen Stellen werden dargelegt.

Abstract

In this thesis a possibility to impose a certain size and arrangement upon aggregates grown and deposited from a spin-casting solution is presented. The sizes of the obtained aggregates and their distances are in the nanometer range. The important physical properties of the involved states are analyzed and described thoroughly in individual chapters.

First the process of spin-casting is discussed in detail. For the first time an analytical solution was found for the temporal height change during the spin-casting process. This solution is verified experimentally by reflectometry and applied to simulate ideal spin-casting processes. Special attention is paid to the development of concentration gradients within the spinning film. Scaling laws for the most relevant physical entities are provided. Additionally an analytical solution of the equations describing the spin-casting process is provided and compared to the simulation. Experimental data from spin-casted C_{60} fullerenes show a distinct bimodal distribution. The theoretical results are employed to explain the experimental findings in the scope of an inversed nucleation.

Further the equilibrium shape of sessile nanoscopic droplets on planar substrates is discussed in depth. A simple formula to calculate the reduced three-phase Hamaker constant from the macroscopic contact angle is provided. The disjoining pressure due to Van-der-Waals forces is shown to cause a deviation from the classical Young equation which predicts size-*in*dependent contact angles. Instead size-*de*pendent contact angles are derived and compared to the semi-classical approach of a specific line tension. Experimental data for different substrates indeed show deviating contact angles. The findings are consistent for Atomic Force Microscopy and Scanning Electron Microscopy. These results are discussed in the provided theoretical framework and the resulting effective Hamaker constant is obtained.

Finally the findings of spin-casting and aggregate stability are employed to show the application of surface modifications on a nanometer length scale to influence nucleation. The optimal conditions for shape and distance of the modification for a most perfect aggregation in a predetermined formation are provided.

Table of Contents

1 Introduction

The presented work deals with the common process of deposition of solid material out of a fluid phase on a solid substrate by spin-casting. Prior to the application for the production of well-defined arrays of solid aggregates the process of spin-casting and the equilibrium condition of nanometer sized droplets are presented in individual chapters.

Nucleation is typically the first step in a phase change which makes it a common phenomenon in both nature and technology. Therefore it is broadly investigated[1–5]. Maybe the most important occurrence of nucleation at all is the formation of rain clouds when water vapor condensates. The effects of nucleation processes can be dramatic as in volcano eruptions (sudden formation of gas bubbles in the magma causes explosion)[6], dangerous as in the case of decompression illness (nitrogen bubble formation in blood)[7] or even funny as in the Diet Coke and Mentos reaction[8]. Other more scientific fields of nucleation are for example cloud chambers[9] for the detection of cosmic radiation or the explanation of the origin of black holes[10]. Commercial applications include pharmaceutical production of drugs[11], metallurgical uses where the quality of the obtained metal or alloy depends on the granularity[12] and electronics where single crystals of semiconductors are needed. Even though nucleation and growth is a two step process the comprehension of the nucleation process is quintessential to influence and alter the outcome of the phase transition. The consecutive growth process is less interesting as it preserves the physical properties and is (in case of a single crystal) just a scale-up of the tiny nucleus as any further phase change would require a new nucleation process. Some refreshing examples of “vanishing polymorphs” are collected by Dunitz and Bernstein[13] where a once stable crystal type A could not be obtained anymore once crystal type B was introduced to the laboratory. This effect is attributed to tiny particles dispersed by the air in the laboratory. Once the new form is present in the laboratory atmosphere its otherwise undetectable particles have an enormous effect on the outcome of the experiments. These examples show the importance of the first stable particle, be it from seeding or nucleation, as it dominates the growth process. Therefore the nucleation process and the possibilities to influence it have to be understood a fortiori in order to obtain the desired outcome.

The process of nucleation is typically described with the classical nucleation theory[14]. It is based on the balance of the gain in energy due to the formation of a new bulk phase

and the energy loss due to the creation of a new phase. It describes the typical cases of nucleation in the bulk (homogeneous) and at an interface (heterogeneous). On one hand this theory is qualitatively rather successful as it predicts that the initial formation of the nucleus is hindered by an enthalpy barrier which has to be overcome in order to build a stable nucleus. This leads to phenomena as undercooling and overheating. On the other hand its quantitative predictions are often very inaccurate. For example a discrepancy of 20 orders of magnitude was found for the prediction of the nucleation rate of Argon[15]! The same holds true for the attempts to influence the weather by providing artificial seeds[16]. It should be rather easy to bring the seeds in the right height of the atmosphere but these undertakings were only partially successful[17].

In this thesis different ways to influence nucleation are presented. Chapter 4 provides a thorough analysis of spin-casting. Though widely employed for the formation and deposition of particles the most important processes are not yet understood quantitatively. Anyway this is quintessential for the understanding when, where and how nucleation takes place. Therefore the temporal height change during the spin-casting process was solved analytically and verified experimentally by reflectometry. The equation is then applied to simulate ideal spin-casting processes. In particular the concentration gradient across the film is investigated. Easy scaling laws for the most relevant physical entities are provided. The obtained results are compared to an analytical solution of the process. It turns out that spin-casting is a perfect tool to locally supersaturate solutions on a predefined time scale. Spin-casting is therefore the perfect tool to investigate nucleation and growth processes. This is shown by experimental data from spin-casted C_{60} fullerenes exhibiting a distinct bimodal distribution which turns out to be the consequence of different nucleation processes.

Classical nucleation theory predicts a strong dependence on the contact angle of the new phase at the involved interface. The contact angle is typically calculated with the classical Young equation which predicts the contact angles to be size-*in*dependent. Instead size-*de*pendent contact angles are derived in chapter 5 by discussing the equilibrium shape of small droplets. The disjoining pressure due to Van-der-Waals forces is shown to cause a deviation from the classical Young equation and size-dependent contact angles are obtained. The result is compared to the semi-classical approach of a specific line tension. Experimental data indeed showing deviating contact angles are provided for different systems and discussed in the provided theoretical framework.

In technical applications nucleation is influenced in both ways. It might be increased in order to obtain phases of many but monodisperse entities or it might be decreased in order to obtain either single crystals or to inhibit phase changes at all. A third route to manipulate nucleation is to limit its spatial occurrence to well-defined positions in order to end up with an array of selectable dimensions. The latter way is followed in Chapter 6 in order to impose a certain size and arrangement upon aggregates grown and deposited from a spin-casting solution. The sizes of the obtained aggregates and their distances are in the nanometer range.

2 Scientific Background

2.1 Contact Angle in Incomplete Wetting and Young's Equation

The equilibrium shape of interfaces is determined by the involved surface and interfacial energies γ. Interfacial energies are always positive as molecules at the surface lack some bonds to molecules of the same phase compared to molecules in the bulk. If a liquid or gaseous phase is attached to a flat solid interface it might wet completely, partially or not wet at all. This depends on the surface energies of the involved phases. If for example the droplet (phase 2, in Figure 1) immersed in a vapor (phase 1) spreads on a flat solid substrate (phase 3) the macroscopic contact angle θ_∞ formed by the droplet and the surface is given by Young's equation

$$\cos\theta_\infty = \frac{\gamma_{13} - \gamma_{23}}{\gamma_{12}}. \qquad (1)$$

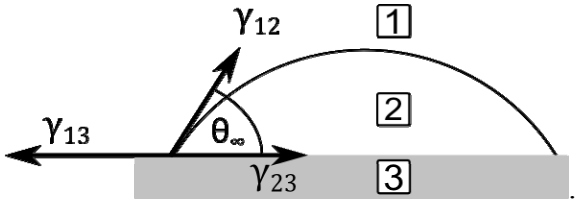

Figure 1: Scheme of a droplet with contact angle θ on a solid substrate and Young's equation.

This equation can be understood from the balance of the forces acting at the three-phase contact point. The classical Young equation is valid independent of the size of the involved droplet and does not distinguish between microscopic and macroscopic contact angle.

2.2 Nucleation

The origins of classical nucleation theory date back to Gibbs. A phase change at given concentration and pressure occurs spontaneously if the free enthalpy G is reduced. The new phase gains enthalpy during growth due to newly formed bonds. This contribution is proportional to the volume (r^3 for spherical particles) and negative. The new phase

involves the creation of a new interface in the system which contributes with its positive surface energy to the total energy. For a spherical nucleus without elastic contributions the total free enthalpy is the sum of the enthalpy contributions of the bulk and the enthalpy loss due to the creation of the new interface.

$$\Delta G_{\text{hom}} = \Delta G_V + \Delta G_S = \frac{4}{3}\pi r^3 \Delta g / v + 4\pi r^2 \sigma \tag{2}$$

Δg is the (negative) difference in molar free enthalpy of the two phases, the molar volume v and the interfacial energy σ. The formation of nuclei in the interior of uniform phases is called *homogeneous* nucleation. The free enthalpy of the newly formed system is shown as function of the nucleus radius in Figure 2. During nucleus growth the total free enthalpy initially rises with the radius up to the critical radius r^*. The maximal enthalpy at this radius which has to be overcome is the critical enthalpy of formation ΔG^*. Using the equilibrium condition of the thermodynamic potentials the contributions from volume and surface for the critical radius reduce to[18]

$$\Delta G^*_{\text{hom}} = \frac{1}{3} A_{nuc}\sigma = \frac{4\pi r^{*2}}{3}\sigma \,. \tag{3}$$

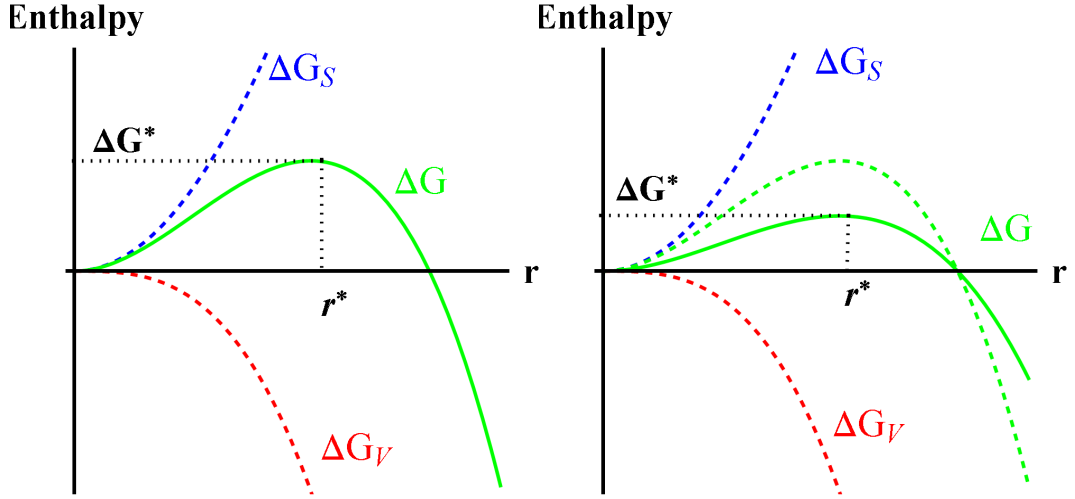

Figure 2 Left: Free enthalpy ΔG (green) of a nucleus formed in bulk (homogeneous nucleation). Right: Free enthalpy ΔG (green) of a nucleus formed at an interface (heterogeneous nucleation). The contributions of the volume and the surface are shown in red and blue, respectively. The critical enthalpy of nucleus formation ΔG^* of a heterogeneously formed nucleus is lowered.

The more common case of nucleation is heterogeneous nucleation where a wetting surface is involved. Instead of spherical nuclei in the bulk, spherical cap shaped nuclei are formed at the wetting interface. The enthalpy is again calculated from the contributions of the volume and interfaces. By employing the Gibbs-Thompson relation the volume term can be substituted by the involved surface energies. Purely geometrical calculations and the force balance of the surface tensions of a partially wetting droplet then show that the free enthalpy of homogeneous formation is reduced by a function of the contact angle[3,18].

$$\Delta G^*_{het} = \Delta G^*_{\text{hom}} f(\theta) \quad (4)$$

$$f(\theta) = \left(\frac{1}{2} - \frac{3}{4}\cos\theta + \frac{1}{4}\cos^3\theta \right) \quad (5)$$

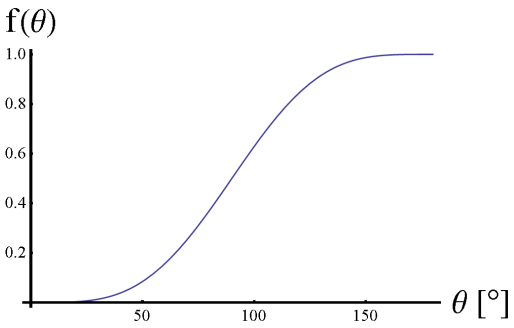

Figure 3: Change of the nucleation enthalpy due to an interface as a function of the contact angle.

This relation depicted in Figure 3 shows how the free enthalpy of nucleus formation is reduced for wetting surfaces while the critical radius remains the same. This is shown in the right graph of Figure 2. Therefore the heterogeneous nucleation is usually favored over homogeneous nucleation.

2.3 Van-der-Waals Interaction

The appearance of matter is governed by the forces between its atoms or molecules. Ignoring gravity, these interactions have their origin in the fundamental electromagnetic force. Derived of this force are interactions as ionic or covalent bonding and electrostatic or magnetic forces. Furthermore matter can attract or repel each other due to the interaction of permanent dipoles (Keesom force), permanent dipoles and polarisable particles (Debye force) as well as spontaneously polarized multipoles in molecules (London dispersion force). The sum of the latter three forces is known as Van-der-Waals force. As atoms consist of a positively charged nucleus and negatively charged electrons the attractive London dispersion force is always present and is thus the most important contribution to the Van-der-Waals force[19]. Keesom and Debye forces are present in most but not all molecules. The strength of the dispersion force for dissimilar molecules is

$$w(r) = -\frac{3}{2}\frac{\alpha_1\alpha_2}{(4\pi\varepsilon_0)^2 r^6}\frac{h\nu_1\nu_2}{(\nu_1+\nu_2)} = -\frac{C}{r^6} \quad (6)$$

with the distance between the molecules r, the polarizability of the molecules α and the frequencies of the orbiting electron ν. This theory was generalized by McLachlan[20] and Lifshitz[21] in order to cope with three shortcomings of the initial theory: 1.) molecules may have more than one absorption frequency, 2.) the behavior might change with the surrounding media e.g. solvent and 3.) the assumed additivity. By replacing the polarizabilities α with the excess polarizabilities in a medium $\alpha(\nu)$ and integrating over the frequency ν it is possible to compute the strength of the attraction due to dispersion from the absorption spectrum. The force between two bodies has been solved for different geometries and the substance dependent parameters are usually combined in the Hamaker constant[22]

$$A_{12} = \pi^2 C \rho_1 \rho_2 \quad (7)$$

with the densities ρ where the indices indicate the involved substances 1 and 2.

3 Materials and Methods

3.1 Atomic Force Microscopy

3.1.1 General

Atomic Force Microscopy (AFM) is a scanning probe technique that allows for very high resolution up to 1000 times better than the optical diffraction limit. The probe used to scan the sample is a flexible cantilever with a very sharp tip. The cantilever is usually made of silicon or silicon nitride. The tip may be of the same material, coated (e.g. diamond like carbon, DLC) or glued to the cantilever. The tip radius is typically less than 10 nm but super sharp tips with radii of 2 nm (SSS-NCH, Nanoworld AG, Switzerland) were mostly used in the experimental sections. Scanning electron microscopy images of a cantilever and tip are shown in Figure 4.

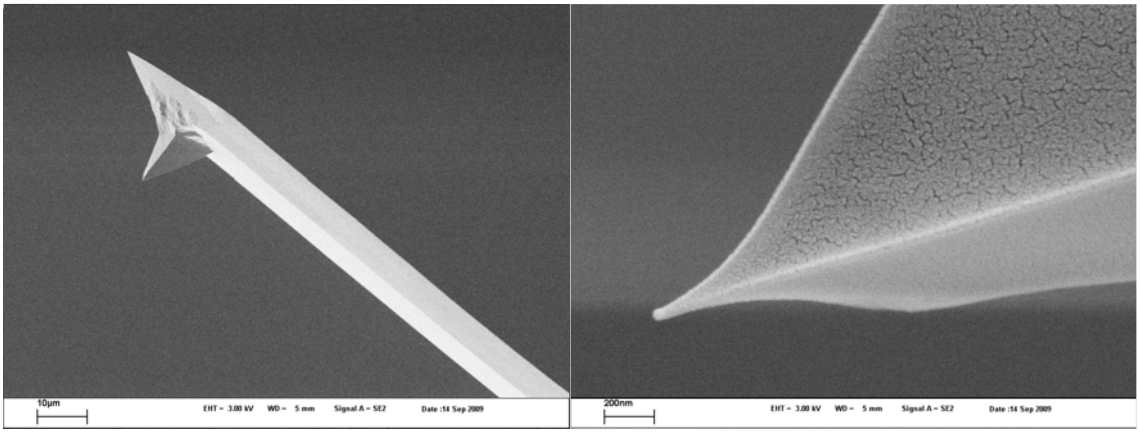

Figure 4: SEM images of SSS-NCH AFM tips.

For the measurement a laser spot is positioned on the backside of the cantilever and reflected on a four-field photo diode as seen in Figure 5. The cantilever is scanned over the sample surface (in some setups the sample is moved under the immobile tip) and due to the deflection of the cantilever the position of the reflected laser on the diode moves. This signal is monitored, and combined with the *XYZ*-signal of the piezo scanner the

surface of the sample can be reconstructed. For a stable scanning process the piezo scanner is used to keep one physical quantity constant. Typical quantities are the vertical laser position on the diode (contact mode), the horizontal position on the diode (friction mode) or the amplitude of an oscillating cantilever (tapping or non-contact mode). Further modes are possible when special tips (asymmetric, conductive, transparent or glued to tuning fork) are used.

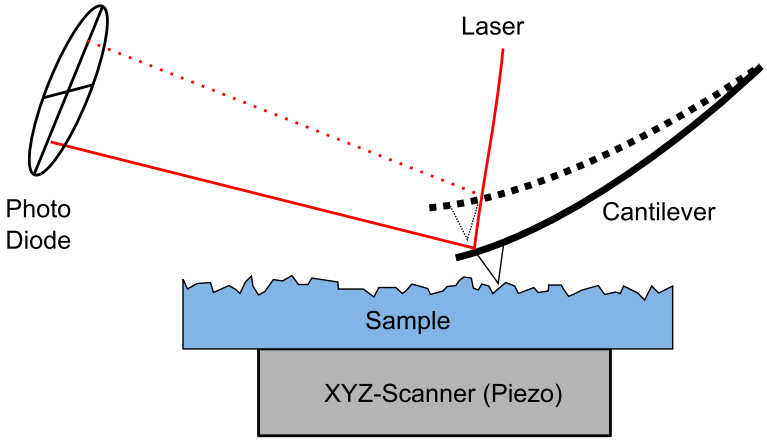

Figure 5: Schematic setup of an AFM. A laser is positioned on a cantilever and reflected on a four-field photo diode. The sample is scanned under the tip, and the diode signal is used for the feedback.

3.1.2 Imaging and Analysis

The surface aggregates were investigated by Atomic Force Microscopy (NanoWizzard III, JPK, Berlin, Germany and Multimode IV, Bruker ASX inc., USA) using super-sharp silicon tips with a tip radius of 2 nm. The images were usually taken with a pixel resolution of the tip radius. All images were taken in non-contact or tapping mode with minimal possible force transmitted on the sample in order to investigate an as much as possible undisturbed sample. The images were flattened up to ninth order and analyzed using the Particle and Pore Analysis module of SPIP (Image Metrology, Denmark). A height of 1 nm was used as a threshold for the detection and different filters were applied. For the analysis of the contact angle the minimum diameter was set to 10 nm and the roundness ($\frac{4 \cdot Area}{\pi d_{\max}^{\ 2}}$, d_{max} longest extension) of not less than 0.8 was set. This process excludes for example the features from the Si_3N_4 TEM grid automatically. Furthermore aggregates of obviously not spherical cap shape and those sitting on apparent surface defects were manually removed. The contact angle is calculated by assuming a spherical cap[23] with the measured volume and radius as

$$\theta = \arccos\left(\frac{3R^4\pi^{\frac{4}{3}} - 7R^2\pi^{\frac{2}{3}}(\sqrt{R^6\pi^2 + 9V^2} - 3V)^{\frac{2}{3}} + 3(\sqrt{R^6\pi^2 + 9V^2} - 3V)^{\frac{4}{3}}}{R^4\pi^{\frac{4}{3}} - 3R^2\pi^{\frac{2}{3}}(\sqrt{R^6\pi^2 + 9V^2} - 3V)^{\frac{2}{3}} + (\sqrt{R^6\pi^2 + 9V^2} - 3V)^{\frac{4}{3}}}\right) \quad (8)$$

3.1.3 Surface Scratching

Besides the application for the characterization of surfaces the experimental setup of an AFM allows for precise manipulations on a nanometer scale. Contrary to the scanning microscopy where the force is minimized as much as possible it is possible to exert forces locally with accuracy below 100 pN. This can be used e.g. to move molecules on a surface or measure forces of chemical bond when ruptured purposefully (molecular workbench[24]). Another application is to structure solid surfaces by indentation or scratching. Most AFMs offer the opportunity to press the tip at the surface with a preselected bending of the cantilever. If the load is high enough this results in an indent on the surface or a scratch if the tip is moved while pressed on the surface. In this thesis this was done with AFM tips with diamond-like carbon coating (Tap300DLC, tip radius < 15 nm, Budgetsensors, Bulgaria). These tips are harder than silicon oxide and can penetrate its surface.

3.2 Spin-casting

For spin-casting (Figure 6) a planar substrate is mounted on a spinning disk and a drop of liquid is deposited onto the spinning substrate (a). Radial forces rapidly spread the drop into a planar film of uniform thickness (b). After this transient step the film thickness is continuously decreasing. Radial forces continuously spin-off sideways portions of the liquid. Within the film a quadratic velocity profile forms due to the friction with the substrate (no slip) and the movement of the free surface (c). Due to the steep increase of viscous forces upon film thinning the amount of spun-off liquid rapidly decreases as the film gets thinner. Simultaneously the film is thinned by evaporation which only occurs at the top surface. If the deposited liquid consists of a mixture of volatile and nonvolatile components (solvents and solutes) then the nonvolatile components remain as deposited film (substrate coating) after spin-casting (e).

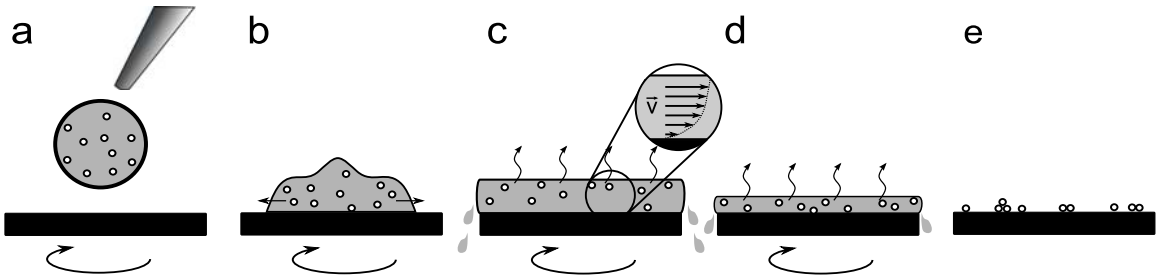

Figure 6: Typical spin-casting sequence for a liquid solution consisting of volatile and nonvolatile components: a) drop deposition, b) spreading, c) and d) film thinning, and e) residual deposited film (nonvolatile component, e.g., solid aggregates in the depicted case). Evaporation of the volatile component occurs during all steps a) through d). Steps a) and b) are transient and b) is fast compared to the longer lasting film thinning c) and d).

A commercially available spin coater (Headway Research, Texas, USA) was used for the casting experiments and a speed adjustable drill was used for reflectometrically controlled spinning. Typical spinning speed was 3000 rpm.

3.3 Reflectometry

The film thinning during spin-casting was measured by interferometry as described previously in the literature[25–27]. The spinning substrate was positioned in an ellipsometric setup (Optrel Multiskop) in a specular configuration with the measurement spot on the rotational axis (see Figure 7).

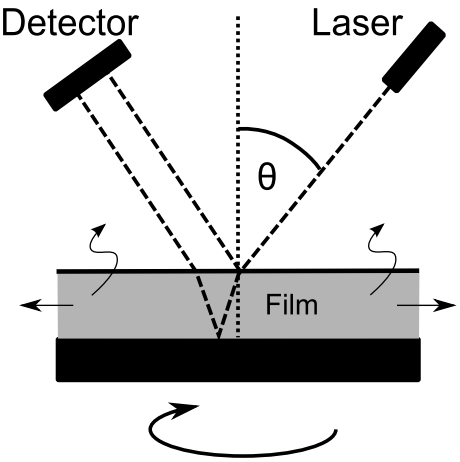

Figure 7: Schematic setup of the measurement of the film thickness during spin-casting.

During spin-casting the spinning film appears to be alternating bright and dark. This effect originates from interfering light reflected at both interfaces, the film surface and the film/substrate interface, respectively. This allows the determination of the change in film thickness ΔH

$$\Delta H = \frac{\lambda}{2\left(\sqrt{n^2 - \sin^2\theta}\right)}. \tag{9}$$

The measurements were performed at an angle of θ = 21° with a wavelength of λ = 632.8 nm, and a refractive index n = 1.497 for toluene. The analyzing polarizer was removed from the ellipsometer setup. The reflected signal was monitored before, during and after the spin-casting process with an acquisition time per data point of 0.04 ms. This is sufficient to record a typical spin-casting process of 1 s with 25 000 data points.

3.4 Materials

3.4.1 Substrates

Five different surfaces were used in the experiments. Four substrates were wafers: TiO_2, SiC, Al_2O_3 (MTI Corporation, USA) and SiO_2 (200nm oxide layer, Silchem, Germany), whereas Si_3N_4 is a TEM grid (Plano, Germany). All except the Al_2O_3 substrates are amorphous. However, even for the potentially crystalline Al_2O_3 surface epitaxial effects are not observed. Al_2O_3, SiC, Si_3N_4 and SiO_2 were cleaned with piranha treatment (H_2SO_4

+ H_2O_2, 2:1) and all substrates including TiO_2 were repeatedly rinsed and sonicated in ultrapure water.

The substrates were investigated by AFM after cleaning but prior to aggregate deposition. Representative scans and cross-cuts of the different surfaces used in the experiment are shown in Figure 8. The surfaces are molecularly smooth. SiC shows some grooves and on the Si_3N_4 surface some features presumably from the manufacturing process are visible. Both features are excluded in the analysis process. The obtained root-mean-square values of the surface roughnesses are given in Table 1.

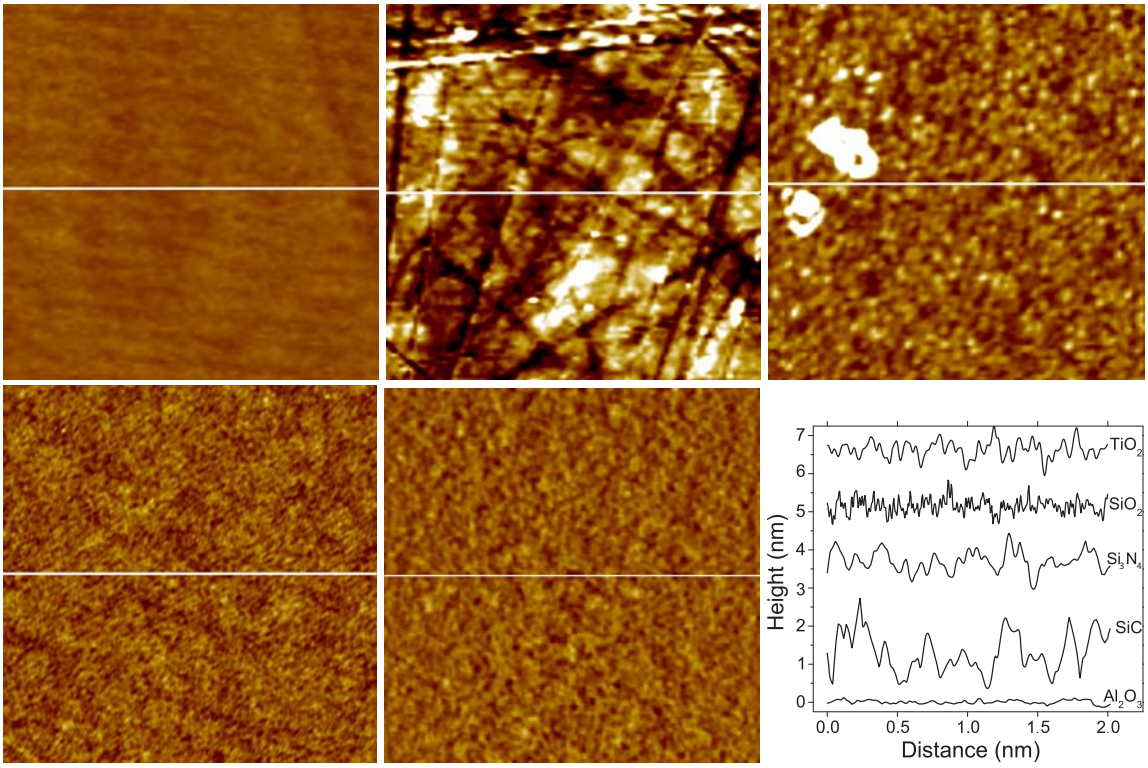

Figure 8: Bare substrates from top left to bottom right: Al_2O_3, SiC, Si_3N_4, SiO_2 and TiO_2. The sizes are always 2 µm with a color scale of -1 to 1 nm from dark brown to white. The white lines represent crosscuts displayed in the graph.

Table 1: Roughnesses of substrates.

Substrate	RMS / nm
Al_2O_3	0.07
SiC	0.77
Si_3N_4	0.54
SiO_2	0.22
TiO_2	0.35

3.4.2 TEM Grid for Scanning Electron Microscopy

Copper TEM grids with SiO_2 film (Plano, Germany) were employed for electron microscopy. Due to the fragile film no wet cleaning with hydrophilization was possible and the substrates were used as obtained.

3.4.3 Chemicals

High purity C_{60} fullerene (99.9+%, Alfa Aesar) was employed. For preparation a stock solution in toluene (Chromasolv Plus for HPLC, 99.9+%, Sigma-Aldrich) was prepared. Lower concentrated solutions were prepared via a solution series.

3.4.4 Sample Preparation

The fullerene droplets were prepared by spin-casting (3000 rpm, room temperature) molecularly smooth substrates with toluene solutions of different concentrations (typically $< 10^{-3}$ mol/l). The toluene evaporates and the non-volatile fullerenes precipitate at the surfaces.

Great precautions were taken to minimize atmospheric contaminations (spin-casting in a dust free-flow hood and minimum time between substrate cleaning and fullerene deposition). After spin-casting a large number of cap shaped aggregates covering the substrate surface is found. The droplets are rather stable against AFM tip deformation and we find that the droplet shape is independent from the time of investigation after preparation. However, the resolubility depends on the time after preparation. After typically more than 1 hour in ambient conditions it is not possible to redissolve the droplets in toluene even under sonication, whereas right after preparation the rinsing of the substrates with toluene leads to a full redissolution. This is attributed to the fact that toluene needs a certain time to diffuse out of the aggregates and that the aggregates are deformable as long as toluene is present. Within this time the aggregates can adopt a minimal energy shape which is a spherical cap. Therefore the concept of liquids and sessile droplets is reasonable for the chosen system. Once the toluene diffused out of the fullerene aggregate the C_{60} molecules might cross-link in the presence of oxygen. Nevertheless experimental indications[28] from Raman spectroscopy show that the aggregates remain amorphous if not too large. The investigated aggregates can therefore be regarded as frozen droplets.

4 Nucleation processes during spin-casting[a]

4.1 Summary

In this chapter a thorough analysis of spin-casting is presented. An analytical solution for the height decrease with time is deduced for the first time. The obtained formula is verified experimentally and evaporation rates for different common solvents are obtained. The result is then used to simulate the ideal spin-casting process of a volatile solvent and a non-volatile solute as a combination of hydrodynamic spin-off, evaporation and diffusion. Special attention is devoted to the developing solute concentration profile in the film. It is found that for certain experimental parameters rather large concentration differences in the film can be obtained. General relations for the dependence of these differences on the involved parameters are found and simple power laws are presented. The obtained relations are verified by analytically solving the spin-casting process. The theoretical results are applied to explain in particular the observed bimodal size distributions of fullerene aggregates produced by spin-casting. It is shown that the nucleation order can be inversed and the aggregation of C_{60} fullerenes happens as well as at the top and at the bottom of the spinning film for certain spin-casting conditions.

4.2 Introduction

Spin-casting[30] (spin-coating) is a highly-utilized technique for both, fundamental research and industrial production, for the uniform deposition of material. The reasons for the widespread use of spin-casting are: 1.) its rather rapid formation of a comparatively large area of uniformly thick films, 2.) its good reproducibility, 3.) its simple technological

[a] The results of the analytical solution are submitted to PRL[29].

setup and 4) its dependence on rather easily measurable or even controllable parameters such as the rotational speed, the viscosity and the evaporation rates. These advantages make it a very versatile tool that is extensively used for the preparation of films of uniform thickness from polymers[31,32], electron resists[33], integrated circuits[34], photovoltaic cells[35] and for the deposition of particles[36] and colloids[37] even on large scales[38,39]. Consequently spin-casting has been investigated extensively and a broad list of academic literature is available. Due to the technological importance of polymer coatings most detailed studies focus on peculiarities such as friction[40], fingering of the droplet[41–43], non-Newtonian liquid behavior[42,44,45], convection[46] or crust formation[47,48].

Nevertheless important details are still unknown. This includes the exact height evolution of ideal spinning films, the total process time and especially the axial spatio-temporal evolution of the component concentrations during film thinning. The latter is in particular important as spin-casting offers a well-defined way to supersaturate solutions in the presence of a solid surface. As the available material for deposition can be limited, the process can be stopped right after the nucleus formation. The obtained aggregates/crystallites are deposited on the surface and can then be investigated by microscopic techniques[36,49,50]. The presented analysis and simulation are therefore the basis for the presented and future applications of the spin-casting process in the context of nucleation and growth.

4.3 Film Thinning During Spin-casting

The time evolution of the film topology and film thinning during spin-casting caused only by fluid-dynamic forces without evaporative losses was first analyzed by Emslie et al.[51] in 1958. An ideal Newtonian, viscous liquid with typical idealized fluid dynamic boundary conditions (no evaporation, no slip, etc.) was assumed. The time evolution of the height H of a rotating film of uniform thickness is then described by:

$$\frac{dH}{dt} = -2KH^3 . \tag{10}$$

K includes the density ρ and the dynamic viscosity η according to:

$$K = \frac{\omega^2 \rho}{3\eta} = \frac{4\pi^2 f^2 \rho}{3\eta} \tag{11}$$

with the angular frequency ω and the frequency f. For a typical organic solvent (ρ = 800 kg/m³, $\eta = 10^{-4}$ Pa s) typical values are given in Table 2.

Table 2: Typical values of the spinning parameter *K* for organic solvents.

ω in RPM	185	585	1850	5850
K in $(\mu m^2 s)^{-1}$	0.001	0.01	0.1	1

The analytical solution of equation (10) regarding the evolution of the film thickness is:

$$H(t) = \frac{H_0}{(1 + 4 \cdot K \cdot {H_0}^2 \cdot t)^{1/2}} \tag{12}$$

with the initial height H_0 at $t = 0$ s. A few years later Acrivos[52] extended the approach by Emslie et al. and presented an analytical solution for non-Newtonian liquids. Both, Emslie and Acrivos did not take into account evaporation. However evaporation is a quintessential factor in spin-casting as equation (12) never reaches zero height and only thins the film with constant concentration. Practical application of spin-casting involves the enrichment and deposition of the solute which is caused by evaporation. The effect of evaporation was first addressed by Meyerhofer[53]. He added a constant evaporation rate E to equation (10).

$$\frac{dH}{dt} = -2KH^3 - E \tag{13}$$

The assumption of a constant evaporation rate is reasonable because the evaporating area does not change once the substrate is completely wet by the thinning film. Meyerhofer did not present an analytical solution for equation (13). He solved it numerically and could show that, at the start, the outflow dominates. Later evaporation is the main cause for film thinning. Subsequent publications by other authors present in even more detail the relation between film thinning and rotational speed[54], solvent evaporation[55,56], viscosity[56–58], heat transfer[59], molar mass[60] or initial solution concentration[61].

Despite ample research activities focusing on spin-casting, an analytical solution of equation (13) has never been presented in the literature as it is nonlinear and inhomogeneous. However, the relation between height and time is strictly monotonous and therefore bijective. Hence the differential equation can be inverted.

$$\frac{dt}{dH} = \frac{1}{-2KH^3 - E} \tag{14}$$

The inversion transfers equation (13) into an ordinary linear differential equation of zeroth order. Its solution can be found in advanced integral lists or with algebraic software.

$$t(H) = \frac{1}{6 \cdot \sqrt[3]{2 \cdot E^2 \cdot K}} \cdot \left[\left(2\sqrt{3} \cdot \operatorname{atan}\left(\frac{1 - 2 \cdot \sqrt[3]{\frac{2K}{E}} \cdot H}{\sqrt{3}} \right) + \log\left(1 - \frac{3H\sqrt[3]{2EK}}{\left(\sqrt[3]{E} + \sqrt[3]{2K} \cdot H \right)^2} \right) \right) - \frac{\pi}{\sqrt{3}} \right] \tag{15}$$

Equation (14) describes the time evolution $t(H)$ of the height H of a fluid film during spin-casting as function of the evaporation rate E and of K, with K defined by equation (11). The solution reflects the asymptotic solutions for small film heights (linear) and for pure spinning of ($E = 0$, c.f. equation (12)). The integration constant was chosen so that

$$t(0) = 0 \,. \tag{16}$$

This is reasonable as in experiments $t = 0$ s and $H = 0$ µm are the two unique values that can be accurately identified. As a result of equation (16) the spin-casting process occurs during *negative* times and ends with a film of formally thickness $H = 0$ µm at $t = 0$ s. This unusual choice turns out to be most practical. For the asymptotic height $H \to \infty$ a finite time $t(\infty)$ is found

$$t(\infty) = -\frac{2^{2/3}\pi}{3\sqrt{3}\sqrt[3]{E^2 K}} \tag{17}$$

which is specific for the system. Its amount is the time period needed to spin-cast an infinite thick film: $t_\infty = |t(\infty)|$. Equation (17) can be used to estimate the evaporation rate by just measuring the total time of the spin-casting process.

$$E = \frac{2\pi^{2/3}}{9 \cdot 3^{1/4}\sqrt{K \cdot t_\infty^3}} \tag{18}$$

If the evaporation rate is known, an upper limit of the amount of solute N that is deposited on the substrate per area A can be estimated by assuming that the whole deposition process is only caused by evaporation during the time t_∞.

$$N/A \approx c_0 E \cdot t_\infty \tag{19}$$

This approximation ignores the non-uniform spin-off across the film due to the vertical velocity profile. Its influence will be discussed later.

Due to the choice of the integration constant (cf. equation (16)) real spin-casting begins somewhere between t_∞ and $t = 0$ with a large but finite height H_0 at $t < 0$.

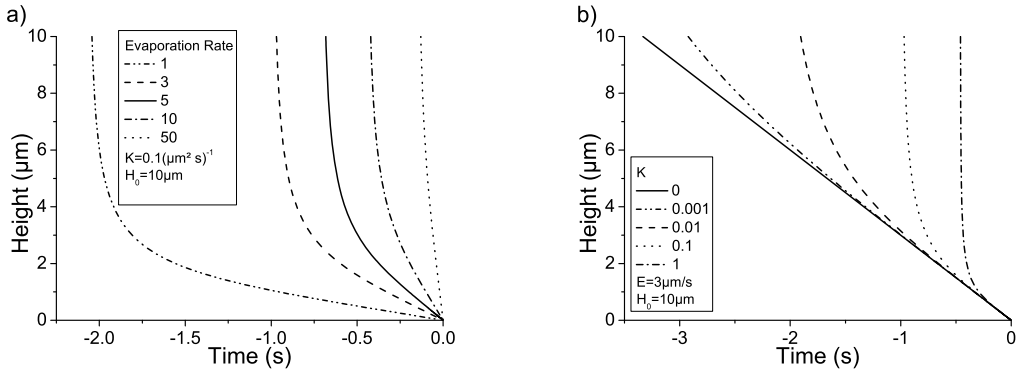

Figure 9: Analytical solutions for the film thinning calculated according to Equation (15). a) shows the film thinning behavior for a constant $K = 0.1$ (µm²s)$^{-1}$ and different evaporation rates E. b) shows the film thinning for a constant evaporation rate $E = 3$ µm/s and different K.

Figure 9 shows how the thickness H of the film changes with time t according to equation (15) for different evaporation rates E and spinning parameters K. In the end of the process a linear decrease of the film height is found that indicates the region when the film thinning is dominated by evaporation and the contribution of the spreading is negligible. Therefore the slope of the final part increases with the evaporation rate. Furthermore the

total process time decreases with increasing evaporation. In the case of constant evaporation rate and variable rotational speed the slope of the final linear part is the same for all curves as seen in b). Again the total process time decreases with increasing K in agreement with equation (17). With decreasing rotational speed (decreasing K) the curve approaches the line of pure evaporation.

4.4 Experimental Results on the Film Thinning

The obtained theoretical result for film thinning was tested experimentally by performing the spin-casting process while measuring the film height with reflectometry. The setup is described in chapter 3.3. Figure 10 a) presents a typical interferogram as it is obtained with the setup depicted in Figure 7 during spin-casting for a pure volatile liquid. The time scale is already shifted according to Equation (16). Figure 10 b) depicts the conversion into the decrease of the film thickness. It also shows a fit of the experimental data according to equation (15).

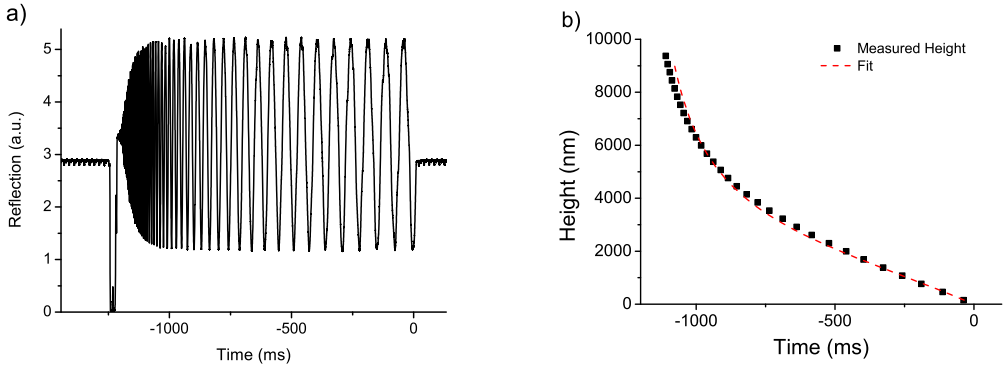

Figure 10: a) Reflected intensity vs. time during a spin-casting process (pure toluene on a planar silica surface (SiO_2), f = 3000rpm, n = 1.497). b) Evolution of the film height as derived from the measured interference pattern (squared dots). The red dashed line is a fit assuming literature values for K.

The optical reflectogram of Figure 10 a) shows four distinctly different sections:

1.) For t up to ≈ -1250 ms the reflected signal is rather constant, with only slight modulations. This is the signal before any liquid is deposited. The weak modulations of the signal are caused by a small imbalance of the rotating substrate (used to calibrate the rotational speed).

2.) At ≈ -1250 ms the reflected signal drops to virtually zero. This is the moment when the liquid drop is deposited on the substrate surface. The intensity decreases to zero due to scattering of the light in all directions. After a few tens of milliseconds interferences of increasing amplitude emerge. The drop spreads and a (not yet uniformly planar) film forms.

3.) The reflected amplitude is constant between $t \approx$ -1000 ms and t = 0 s. During this time segment the liquid forms a planar film of uniform and decreasing thickness. Its rate of

change in film height is reflected in the increase of the times between the interference extremes. At $t = 0$ s the film is completely vanished according to Equation (15).

4.) After $t = 0$ s the reflected intensity attains the same value and behavior as prior to the liquid drop deposition before $t = -1250$ ms. All liquid has evaporated.

The measured thinning of the film (squared data points in Figure 10 b) was fitted with (15) assuming a spinning parameter K based on literature data and on the rotational speed. The only fit parameter is the evaporation rate E. The obtained evaporation rates are given in Table 3. For toluene ($\eta = 5.9 \cdot 10^{-4}$ Pa·s, $\rho = 866.9$ kg/m³) an evaporation rate of 3.22 ± 0.07 µm/s was obtained by the fit and 3.06 µm/s is found with Equation (18). Both values are reasonably close to the literature value of 2.8 µm/s[62]. Besides the different laboratory conditions the higher value might be a consequence of the spinning that leads to a constant stream at the free surface and might result in higher evaporation rates as for solvents at rest. The film thinning behavior is identical for ideal mixtures respectively solutions with low solute concentrations. This was proven experimentally with low concentration solutions of fullerenes ($c < 10^{-3}$ M) in toluene.

Table 3: Evaporation rates of different solvents obtained by reflectometry.

Solvent	*Evaporation Rate [µm/s]*
Toluene	3.22 ± 0.07
Acetone	17.5 ± 0.4
Water	0.57 ± 0.02
TFA	0.52 ± 0.02
Acetic Acid	1.03 ± 0.03

4.5 Simulation of Spin-casting

4.5.1 Simulation Model[b]

The analytical solution of the film thinning behavior was used to simulate the whole spin-casting process including spreading, evaporation and diffusion as well as the evolution of the concentration within the film. It is also assumed that both spin-casting parameters K (cf. equation (11)) and the evaporation rate E are constant. That implies a Newtonian behavior of the solvent, an ideal mixture and concentration independent parameters. Also collective effects due to the intermolecular interactions (solidification, cross-linking, gel

[b] The simulation was developed in cooperation with Andreas Vetter and John Berg.

formation, etc.) are ignored in this approach. Figure 11 shows the model for the simulation of the axial spatio-temporal compositional changes within a thinning film that consists of a binary solution of a nonvolatile solute and a volatile solvent.

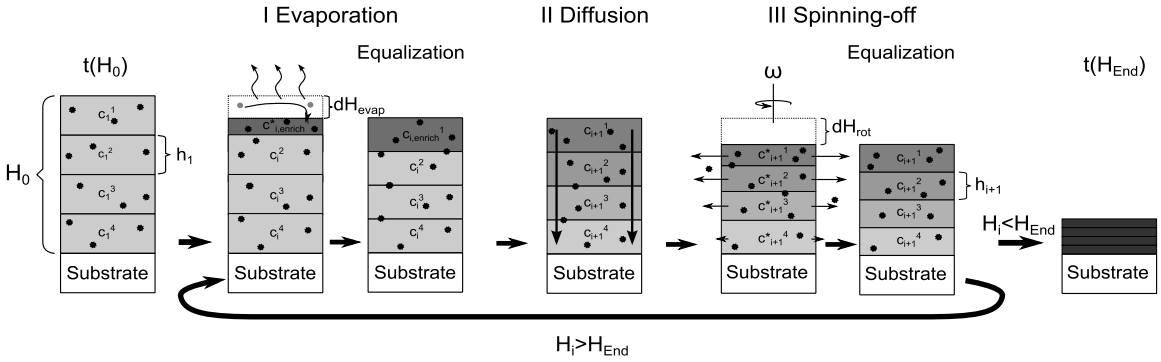

Figure 11: Model for the simulation of the spatio-temporal distribution of the solute concentration *c* within a thinning film of height *H* during spin-casting of a binary mixture of a volatile solvent and nonvolatile solute. The film gets continuously thinner due to evaporation of solvent at the surface and the fluid dynamics (spinning-off). At the same time the evaporation from the surface at a rate *E* leads to a local solute enrichment close to the surface. This local enrichment is continuously decreased by diffusive transport into the film. In the simulation these simultaneous processes are separated into three steps that are calculated sequentially. Spinning-off (quadratic velocity profile due to no slip condition) and evaporation (top layer) result in unequal heights of the individual layers. This is corrected with an equalization step.

The simulation begins after the initial drop deposition. It is assumed that the liquid has already formed a flat film (c.f. Figure 6 c), page 8). Within the thick flat film, the solute concentration is assumed to be homogeneous and identical to the initial concentration prior to drop deposition. This is reasonable because the formation of a (thick) flat film occurs very rapidly after drop deposition[51] (Figure 6 a)+b)). In addition any evaporative solvent loss is small compared to the rather large volume and the liquid flow during film formation will equalize local enrichments.

For the technical implementation of the simulation it is assumed that the film of total thickness H_i at time t_i consists of a number, J, of segments. These segments h_i^j have two indices, i for the time and j for the height. At the beginning of every loop the segments are of identical thickness, $h_i^j = H_i/J$, $H_i = \sum_{j=1}^{J} h_i^j$. The last step is possible as all segments have the same height. The simulation starts with a large but finite initial thickness H_0. Theoretically H_0 should be infinite but for computational implementation is assumed equal to or larger than ten micrometers. This is in agreement with the typical experimental initial thicknesses right after the drop has spread to a film of uniform thickness (see Figure 10 b)). It is assumed that the composition of the initial film is homogeneous. The height change is implemented according to the theoretical behavior that was calculated for spin-casting of a pure volatile liquid (equation (15)).

During this film thinning three processes occur at the same time 1.) evaporation, 2.) diffusional transport within the film, and 3.) spinning-off. Both, evaporation and spinning-off change the height of the segments non-uniformly. As further steps need equidistant vectors (all segments have the same height) an additional equalization step is included. This projects the concentration profile with non-equal element heights on a vector with equidistant element heights. This step is neutral in respect to particle amount and total concentration. In the simulation the three simultaneously occurring processes

are approximated by sequential loops describing the individual processes (Figure 11). The shorter the time interval dt_i for a loop, the better the approximation reflects reality. As the loss in height is not linear with time, the interval time dt_i is not assumed constant. Instead it is calculated from a chosen fractional loss in height per interval, $dH_i = H_I / F$, $F > J$, with $dt_i = t(H_i) - t(H_i - dH_i)$ by using Equation (15).

During the evaporation step (step I. in Figure 11) the film with total film thickness H_i decreases by $dH_{evap} = Edt_i$. The enrichment of non-volatile solute due to the evaporation in time dt_i is assumed to accumulate during this step only in the top segment of the film.

$$c_i^1 \rightarrow c_i^1 \cdot h_i / dH_{evap} \tag{20}$$

Then the non-equidistant vector (smaller top segment) is projected on an equidistant vector with the same amount of elements.

In the following diffusion step (step II. in Figure 11) the diffusive dilution of this solute enrichment from the top layer segment into the layer segments below is calculated for the given time interval dt_i according to

$$\frac{\partial c(\vec{x},t)}{\partial t} = D \cdot \nabla^2 \cdot c(\vec{x},t) \tag{21}$$

.

D is the diffusion constant and diffusion occurs only between neighboring segments. As a result of this simulated diffusion process the solute concentration will be different for each segment. The solute concentration will decrease from the top to the bottom layer segments in a way specific for the system parameters and system time (c_i^j to c_{i+1}^j).

In the following spinning step (step III. in Figure 11) film thinning solely occurs via volume loss through spinning-off: $dH_{rot} = dH_i - dH_{evap}$. The change of height for every segment can be derived from the radial volumetric flux, the continuity equation and the spin-off. The height change of the segments is a result of the advective part of the flux[63].

$$\Delta h_i^j = \frac{3}{2}\frac{dH_{rot} h_i}{H^3}\left(h_i H(2j-1) - j^2 h_i^2 + j h_i^2 - \frac{h_i^2}{3} \right) \tag{22}$$

The solute concentration c_i^j in each segment remains unchanged during this step. Again the vector with elements of non-equidistant heights is projected on an equidistant vector.

These simulation cycles are repeated until finally a certain pre-selected final film thickness H_{End} is reached (typically a few tens of nanometers). The model was implemented in Matlab (The Mathworks, Inc., Natick, MA v 7.12) using a standard finite element approach to calculate the partial differential equation for the diffusive transport (Equation (21)).

The consistency and validity of the simulation process were tested extensively by: 1.) varying the number of layer segments, J, 2.) varying dH_i by changing the fraction F of the reduction of the total film in each cycle respectively simulation step, 3.) variation of the initial film thickness H_0, 4.) commuting the sequence (spinning-off, evaporation,

diffusion) in the loop, and 5.) varying the final film thickness H_{End}. It turns out that consistent results are obtained for typical parameters, $1000 > E > 0$ µm/s, $1000 > D > 0.01$ µm²/s and $10000 > f > 0$ rpm if the simulation parameters were: $J = 50$, $H_0 >= 10$ µm, $H_{End} = 10$ nm, $F = 250$. This corresponds to ms > dt_i > µs, for large or small H_i, respectively.

4.5.2 General Evolution of the Solute Concentration in the Spin-casted Film

Figure 12 shows schematically the time evolution (as it is obtained from the simulations) of the film height and of the solute concentration profile within the film for an ideal binary mixture of a nonvolatile solute and a volatile solvent. In addition to the film height H, the scheme focuses on the time evolution of the solute concentrations c_{LV} and c_{LS} at the liquid-vapor- and liquid-solid-surfaces, respectively, and on their difference Δc_i at time t_i (cf. inset of Figure 12 for definition of the parameters).

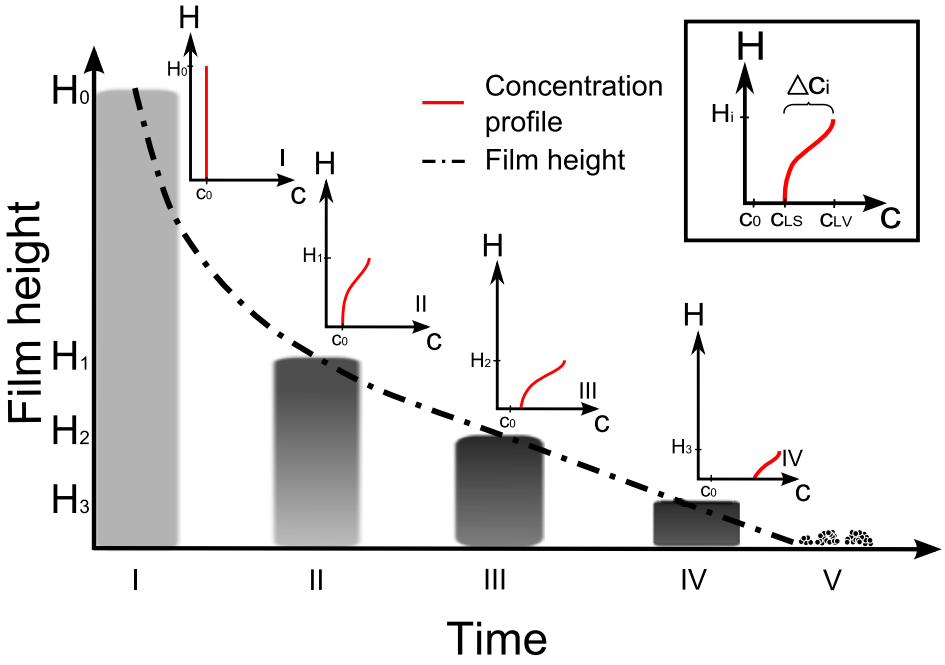

Figure 12: Evolution of the film height H and of the internal solute concentration profile $c(H,t)$ of a binary solution with a nonvolatile solute and a volatile solvent. The framed inset shows the definitions of various characteristic solute concentrations at time t_i that correspond to film height H_i. c_0 is the initial solute concentration, c_{LV} is the solute concentration at the liquid-vapor-interface, c_{LS} is the solute concentration at the liquid-solid-interface, Δc_i is the solute concentration difference between c_{LV} and c_{LS}. The cartoon depicts five characteristic stages of the internal solute concentration during spin-casting: (I) initially the film has a height H_0 and the internal solute concentration is homogeneous with a value c_0, (II) as the film height has decreased to H_1, both, c_{LV} and Δc_i increase but c_{LS} remains close to c_0, (III) c_{LV}, c_{LS} and Δc_i increase, $c_{LS} > c_0$, (IV) c_{LV} and c_{LS} increase further but Δc_i decreases again because diffusive equilibration is very effective (low film height H_3), $c_{LS} >> c_0$ (V) all solvent has evaporated and the solute is deposited on the substrate surface.

The simulated spin-casting process starts with an already flat film of height H_0 and homogeneous initial concentration c_0 (stage I). Then the height decreases due to spinning-off (volume loss of solution) and evaporation (selective loss of solvent from the surface segment). Initially the spinning-off is rather effective and dominates the film

thinning. While the spin-off is concentration neutral the evaporation enriches solute in the top layer of the film resulting in a difference in concentration between top and bottom layer (stage II). This enrichment is counteracted by the diffusion that transports the enrichment to lower layers and eventually reaches the surface (stage III). When the film is rather thin the diffusion is more efficient than the enrichment due to evaporation and both concentrations, top and bottom, approach and the difference vanishes (stage IV). Finally, when the solvent is completely evaporated, only the solute remains at the substrate (stage V).

4.5.3 Comparison of the Concentration Evolution With and Without Spinning-off

For the understanding of the peculiarities of spin-casting the simulation is employed to compare the solute concentrations of dry-casting ($K = 0$ $(\mu m^2 s)^{-1}$, no rotation, only evaporation) and spin-casting. Figure 13 shows quantitatively the spatio-temporal evolution of the obtained solute concentrations with $c_0 = 1$ %, $D = 1$ $\mu m^2/s$, $E = 3$ µm/s and $H_0 = 10$ µm.

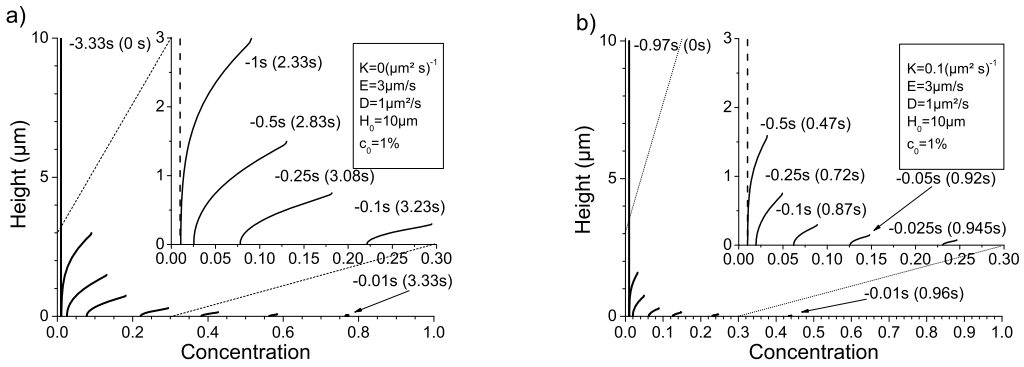

Figure 13: Solute concentration profiles at different film heights and different times resulting from simulations with $c_0 = 1$ %, $D = 1$ µm²/s, $E = 3$ µm/s, and $H_0 = 10$ µm for pure evaporation (a) and for $K = 0.1$ $(\mu m^2 s)^{-1}$ (b). For better insight, both, the times till complete evaporation (negative values) and those elapsed since the start of the process (positive values, in brackets) are presented.

The figure presents the solute concentration profiles for different film heights. In addition also the time for each profile is shown in two ways: 1.) according to equation (15) with the origin of time at $H = 0$ (negative values) and 2.) the time elapsed since the start of the process with $t = 0$ s for $H = H_0$ (positive values, in brackets). The latter is not universal as it changes with the initial height H_0. In general the relations between height and solute concentration are rather similar for both simulations. The decrease in film height is accompanied by a general increase of the concentration and the originally homogeneous concentration becomes heterogeneous with persistently higher solute concentrations at the liquid-vapor surface. Still some significant differences are observed. First the total process time is higher without spinning. This was expected as all solvent in the film has to evaporate and no solution is lost due to spin-off. The same argument holds for the total concentration. This is considerably higher in the case of pure evaporation as can be seen by comparing the (little) curves at -0.01 s which means 10 ms before the solvent is completely evaporated. In both cases the remaining film will basically completely

evaporate as the film height is only some nanometers. The spinning of such a thin film is very inefficient (cf. Figure 9 b), page 15). As the concentration for pure evaporation is already higher (78 % vs. 45 %) the final coverage of the substrate will be higher. The inserts reveal in particular different behaviors for both cases regarding the concentration profiles. In the case *without* spinning the solute concentration remains rather homogeneous for roughly the first second and then a profile with a rather pronounced concentration difference $\Delta c/c_0$ evolves (the first profile shown in Figure 13 a) is after 2.33 s). In the case *with* the spinning-off the enrichment is as fast as before due to the same evaporation rate. As the film reaches smaller heights more rapidly pronounced, solute concentration profiles appear faster after the start of the simulation. However, compared to the case without rotation, $\Delta c/c_0$ is generally smaller and it vanishes more rapidly as the film approaches complete drying. This can be attributed to the combination of the volume loss by spinning-off causing a faster thinning of the film (not affecting the concentration) which in turn results in a more efficient diffusional transport and thus in a relatively smaller $\Delta c/c_0$.

4.5.4 Quantitative Details on the Spatio-temporal Evolution of the Solute Concentration

The time evolution of the various normalized local concentrations, c_{LV}, c_{LS}, the solute concentration differences $\Delta c/c_0$ (= $(c_{LV} - c_{LS})/c_0$) are investigated in detail and shown as logarithmic plots in Figure 14. Simulated curves are shown for three different evaporation rates (1, 3 and 10 µm/s). The other parameters are $K = 0.1(\mu m^2 s)^{-1}$, $D = 100\ \mu m^2/s$, $H_0 = 10\ \mu m$ which are typical values for molecules in organic solvents.

For all three evaporation rates c_{LV} increases continuously as soon as the process starts (indicated by the vertical dashed lines). The concentrations at the liquid/solid interface, c_{LS}, also increase continuously with time but the increase is delayed by typically ≈ 0.1 s compared to the start of the increase of c_{LV}/c_0. This is caused by the delayed arrival of the solute transported by diffusion to the liquid-solid interface. This behavior of c_{LV} and c_{LS} is representative and will not be displayed in further graphs. The delay in the beginning of the increase of the interfacial concentrations is reflected by the (very) steep increase of $\Delta c/c_0$ at the very beginning of the process. When the diffusing solute reaches the substrate c_{LS} increases and the local enrichment at the liquid-vapor surface is efficiently drained as the diffusion gets more efficient when smaller film heights have to be crossed. Consequently the difference $\Delta c/c_0$ decreases continuously. The maximum values for $\Delta c/c_0$ reach ≈ 20 %, 7 % and 2 % of the initial concentration for $E = 10$ µm/s, $E = 3$ µm/s, and $E = 1$ µm/s, respectively. A further parameter of the curves is the time t_{max} when the maximum solute concentration is reached compared to the time of the total process t_∞ (cf. equation (17)). t_{max} changes from 5 over 10 to 22% of the respective t_∞ for the given evaporation rates. The relevant parameters are investigated individually in the following.

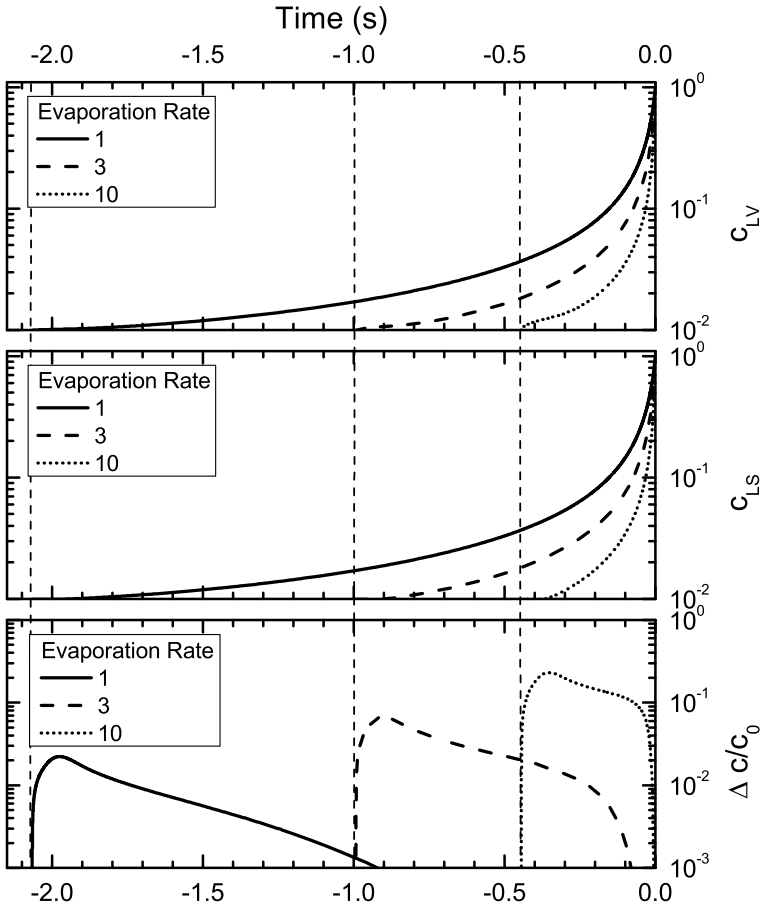

Figure 14: Time evolution of the various concentrations for a typical spin-casting process (D = 100 µm²/s, H_0 = 10 µm, K = 0.1 (µm²s)$^{-1}$, c_0 = 1%).

4.5.5 Initial Height

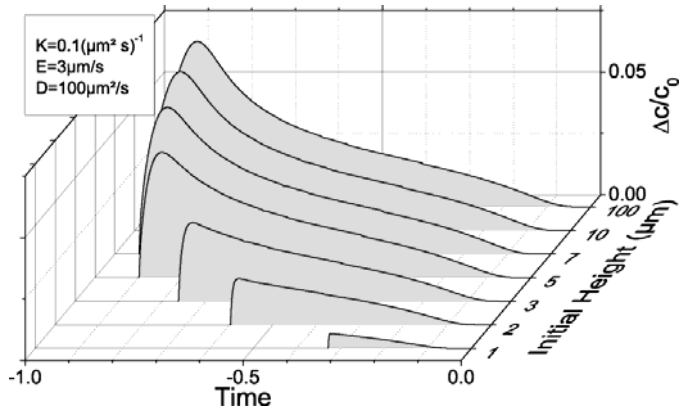

Figure 15: Evolution of Δc/c0 for a given set of parameters as a function of the initial film height at the start of the simulation.

The influence of the initial film height is presented in Figure 15. The *Δc/c0* curves for very small initial heights seem to be cropped out of the curves for higher initial films. When H_0 increases, *Δc/c*0 reaches a saturation value. It barely changes when the initial height increases by a factor of 10 from 10 to 100 µm and the total process time is barely

influenced. This is a confirmation that Equation (15) was correctly implemented as the film height diverges at t_{∞}, and close to this time even dramatic changes in height do not influence the total time a lot. Obviously, with H_0 exceeding 10 µm, most of the liquid is spun-off without any impact on the solute concentration profiles.

In Figure 16 $(\Delta c/c_0)_{max}$ (i.e., the maximum values of $\Delta c/c_0$) is plotted as a function of the initial height for sets of various parameters.

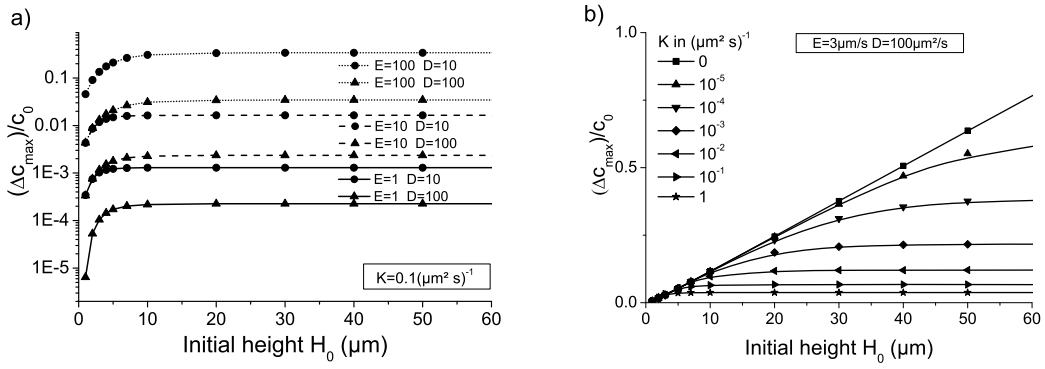

Figure 16: $(\Delta c/c_0)_{max}$ (maximum of $\Delta c/c_0$) as function of H_0: a) for different sets of D and E and b) as function H_0 for different K. $K = 0$ corresponds to pure evaporation without spinning.

Figure 16 a) shows again that $(\Delta c/c_0)_{max}$ is rather independent from the initial film height H_0 as soon as H_0 exceeds a certain critical thickness H_{eff}. This H_{eff} is rather independent from the evaporation rate E and diffusion constant even though the value of $(\Delta c/c_0)_{max}$ changes with both parameters. In contrast Figure 16 b) shows that the spinning parameter K has a significant influence on the concentration gradient in the film. This is due to the fact that the radial forces rapidly form a uniformly high, planar film from any deposited drop. As long as this initial film is thicker than H_{eff}, its thickness decrease is largely dominated by spinning-off. For sufficiently large K, H_{eff} is sufficiently small, so that usually the deposited drops, however different their individual deposition process may be, spread into an initial planar film with a height exceeding H_{eff}. If spun at typical frequencies ($\omega > 600$ rpm, $K > 0.01$ (µm²s)$^{-1}$ the influence of the initial height is only obvious below 20 µm. If a drop of 1 mm radius is placed on a rotating wafer of 1 cm² the deposited volume corresponds to a film of 42 µm. Therefore the condition of sufficient high initial film is fulfilled for standard casting set-ups. Furthermore this explains why spin-casting is reproducible and little sensitive to the details of the drop deposition prior to the film formation. On the other hand spin-casting becomes less reproducible for small K, i.e., typically low rotational speeds or pure evaporation. This is the case e.g. for drop-casting or spray-coating. Then two effects play a role: 1.) no homogeneous film is formed and the lateral distribution of deposited material can vary dramatically (influences of Marangoni flow, coffee rings, etc.) and 2.) pure evaporation leads to very high concentration differences that might result in scenarios where concentration dependent effects play a role (aggregation, nucleation and growth, crust-formation, etc.). Therefore spin coating is justly the preferred technique when homogeneous coatings are requested.

4.5.6 Final Coverage

Another important parameter in spin-casting is the coverage or amount of deposited material. The amount of solute present in the spinning film is shown in Figure 17 as double logarithmic plots. The temporal progression of the curves is from top right to bottom left. Initially the particle number decreases linearly with the film height as the spinning-off is most efficient and basically all material in this stage is lost for the process.

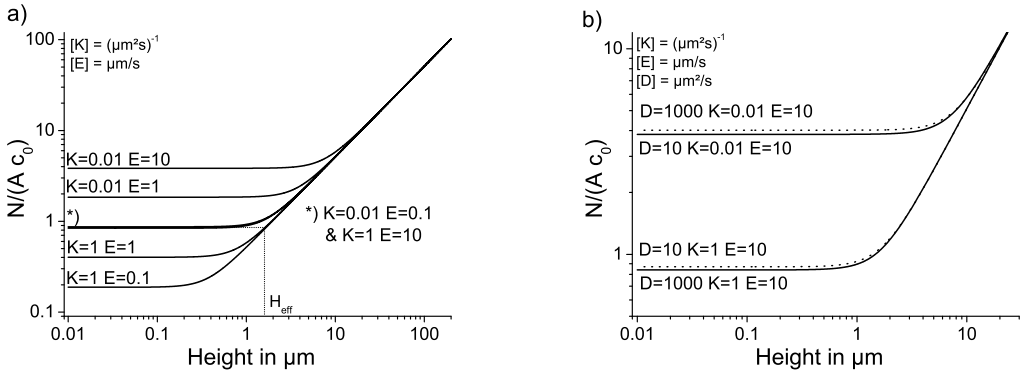

Figure 17: Amount of solute per area present in spinning film as a function of film height for a) different evaporation rates and spinning parameters and b) different diffusion constants. The cross-over of the two straight lines indicates the effective height Heff exemplary indicated in a).

Once the film is rather flat the spinning-off is not dominating anymore and the loss in film height is due to evaporation which does not affect the amount of particles present in the film. Again it is obvious why the initial height H_0 has to be higher than H_{eff} (cf.. Figure 17 a) where it is exemplarily indicated). Above this height the solution and with it the solute is basically completely spun off whereas below this height the evaporation dominates and the volume loss is dominated by evaporation which is specific for the solvent. Therefore the amount of solute in the film stays constant. The film height H_{eff} when the evaporation dominates depends on both, the evaporation rate and the spinning parameter K whereas the diffusion constant D plays a very minor role. As the film of height H_{eff} evaporates completely it is proportional to the amount of solute finally deposited on the substrate. It can be seen that the final coverage can be chosen as the influence of E can be compensated by adjusting K (two curves marked with * in Figure 17 a) with different evaporation rates). This graph does not provide any information about the time of the process, and the two processes with identical coverage occur on different time scales.

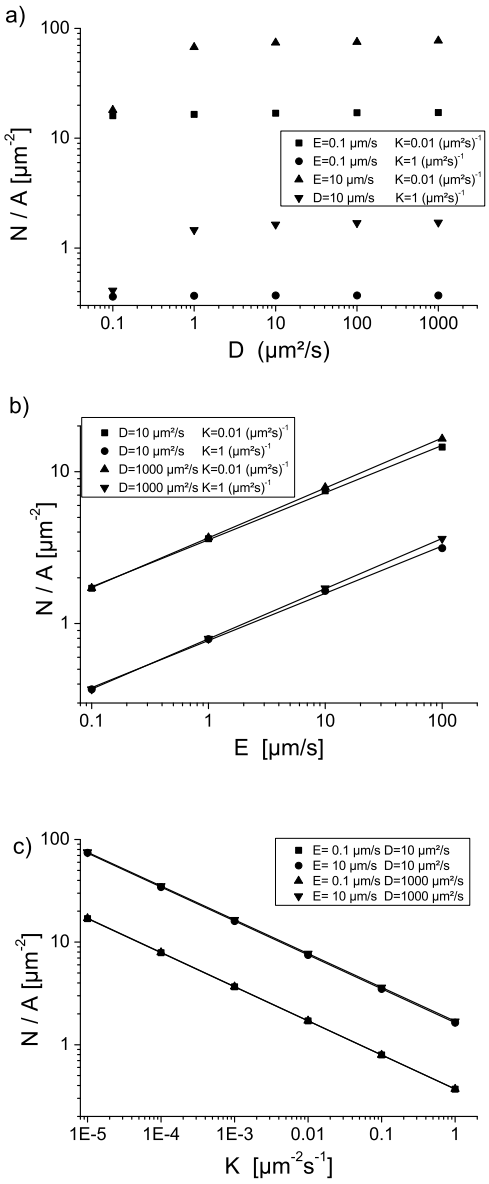

Figure 18: Final coverage (amount of solute per area) as a function of diffusion constant D, evaporation rate E and spinning parameter K. The solid lines are linear fits.

The dependency of the coverage on the three parameters D, E and K is presented in Figure 18. The diffusion constant plays only a very minor role if higher than 1 µm²/s for typical parameters of E and K. A very important property of the spinning system is whether the *Stefan condition* is fulfilled. The Stefan condition determines a diffusional transport from the surface as fast as the enrichment caused by the evaporation. If it is not fulfilled the solute enriches at the surface and is completely spun-off. In non-ideal cases as e.g. crust formation for polymers this might not be true as the crust might be stable enough to stay intact at the surface and compete the spinning-off. For the dependence of the coverage on the evaporation rate and spinning parameter simple power laws (double logarithmic plots) are found.

The obtained relation for the final coverage is:

$$\frac{N}{A} \cong 0.8 \cdot c0 \cdot K^{-1/3} \cdot E^{1/3}. \quad (23)$$

4.5.7 Evolution of Solute Concentration Differences

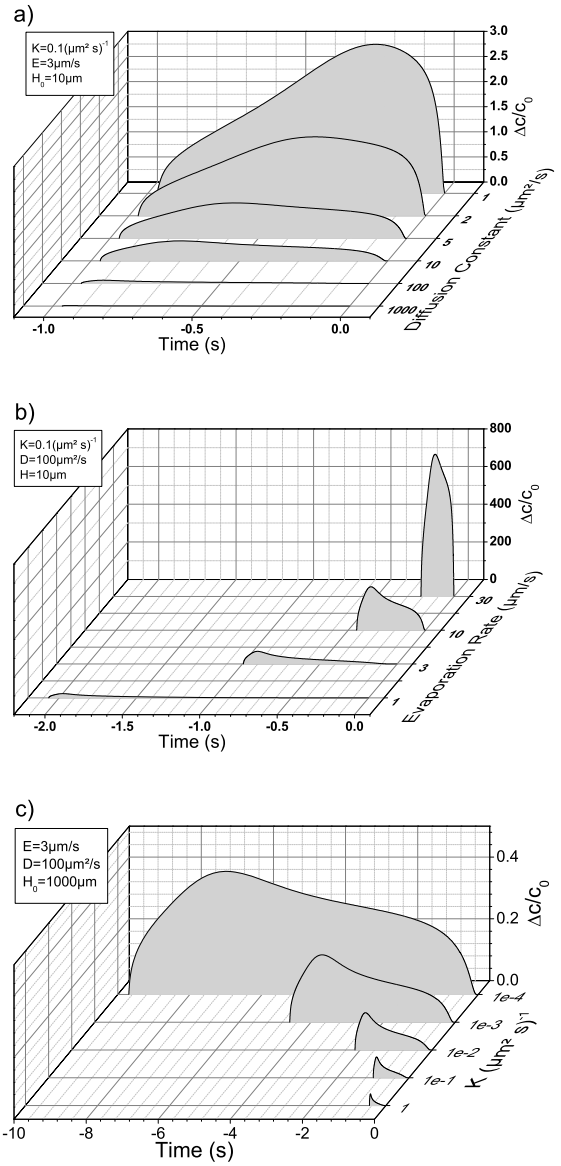

Figure 19: Evolution of the differences in solute concentration between surface and interface as a function of a) the diffusion constant *D*, b) the evaporation rate *E* and c) the spinning parameter *K*.

Figure 19 shows the time evolution of the difference in concentration across the film $\Delta c/c_0$, for various parameters. Figure 19 a) shows the dependence on the diffusion constant D in the range from 1 to 1000 µm^{2}s. According to the Stokes-Einstein equation this corresponds e.g. to particles with diameters of 0.8-800 nm in toluene. As D does not influence the film thinning behavior (cf. equation (15)) the process time for complete solvent evaporation is identical for all cases. However, the increase of $\Delta c/c_0$ starts much steeper for the lower diffusion coefficients due to the competition between evaporative local enrichment and the diffusive dilution. Whereas Δc remains rather small ($< 0.2\, c_0$) for $D >= 100$ µm²s, $\Delta c/c_0$ can become quite large for small D (i.e., for large molecules or aggregates). Furthermore the time t_{max} for the maximum of $\Delta c/c_0$ shifts quite remarkably to later times as D decreases. This means that for high diffusion constants the diffusion wins over the enrichment from the evaporation earlier and thus at far thicker films.

The influence of the evaporation rate can be seen in Figure 19b. The rates from 1 to 30 µm/s roughly relate to TFA, toluene, acetone and methylene chloride. Except for the evaporation rate the parameters are kept at the same values as before. According to equation (15), the total time of the film thinning becomes shorter as the evaporation rate increases. The plot is displayed in the time convention $t = 0$ s at $H = 0$ µm. If E is very high, the film thinning proceeds rapidly but also the local enrichment at the liquid-vapor surface is strong. The diffusional transport through the thinner film does not sufficiently compensate the enrichment and causes a strong increase in the top layer of the film. As a result $\Delta c/c_0$ is much larger and the maximum is reached later compared to the total spin-casting time for larger evaporation rates.

The variation of the parameter K that includes the system parameters viscosity and density as well as the spinning velocity (cf. equation (11)) and can hence be chosen rather freely. For a solvent with the dynamical viscosity 10^{-3} Pa/s and a density of 800 g/l the range 1 to 10^{-4} $(\mu m^2\ s)^{-1}$ corresponds to spinning speeds of roughly 6000 to 60 rpm. K influences the film thinning and the spatial-temporal concentration as depicted in Figure 19c. The initial height H_0 was set to 1000 µm to avoid influences from limited initial film heights (cf. Figure 16 b)). With increasing K the film thinning due to spreading proceeds faster and the total process time reduces dramatically. With slower spinning the evaporation gains more and more influence. Obviously, with larger K, the rather effective spinning-off results in faster film thinning and increases the efficiency of the diffusional transport towards the end of the process and thus lowers $\Delta c/c_0$ more rapidly than for low K.

The influence of the initial solute concentration is not displayed as it is only a factor without physical relevance for the process. Nevertheless this parameter is important to shift the concentration difference in regions that are relevant for processes like nucleation, aggregation or precipitation and final coverage.

All curves have some prominent points. These involve the maximal height of the concentration difference, the top concentration when the difference is highest, the film height in the moment of maximal concentration difference and the time of the maximum. All these features are discussed in detail in the following and for some simple mathematical relations are provided.

4.5.8 Maximum Concentration Difference in Spinning Films

For solidification and aggregation the difference in concentration across the film is an important parameter. For example this is most important when the concentration at which nucleation starts at the substrate interface and in the bulk are very close. Depending on the desired outcome a rather high concentration gradient (top nucleation) or a homogeneous concentration across the film might be desired. As this entity scales with the initial concentration only the normalized values are presented in the following. Figure 20 a) shows that the heterogeneity $(\Delta c/c_0)_{max}$ within the film decreases with the diffusion constant D. Except for high evaporation, slow rotation and very slow diffusion (Stefan condition not fulfilled) the obtained graphs are linear in the double logarithmic plot and have the same negative slope. This means that a general power law $\Delta c_{\max} \propto D^{\alpha}$ exists.

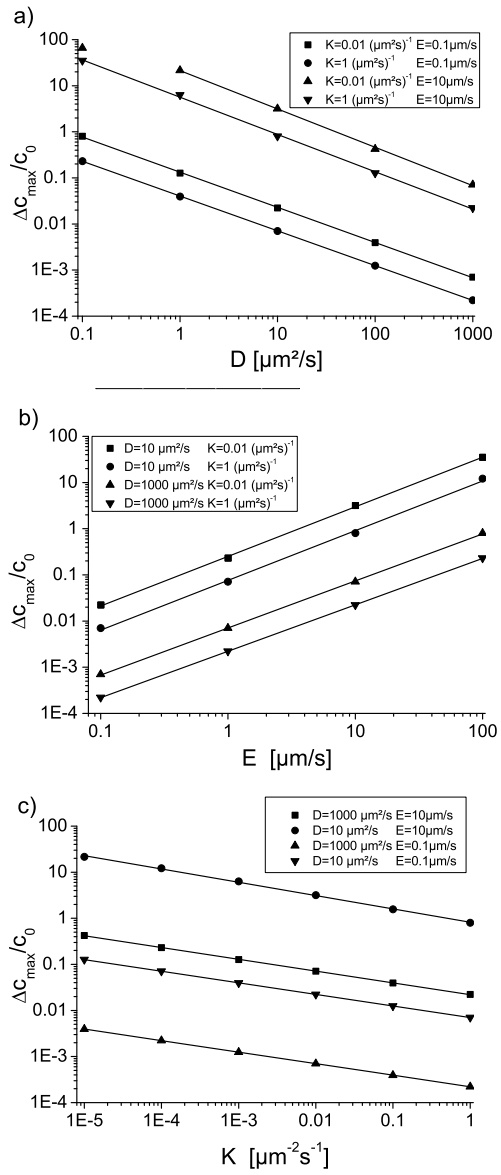

Figure 20: $\Delta c_{max}/c_0$ (Maximum of $\Delta c/c_0$ as a function of a) the diffusion constant *D*, b) the evaporation rate *E* and c) the spinning parameter *K* as double logarithmic plots. The solid lines are linear fits.

Analogous linear dependencies for the evaporation rate E and the spinning parameter *K* are found. The increase of $(\Delta c/c_0)_{max}$ with the evaporation rate is plausible because the evaporation rate determines directly the enrichment of solute at the liquid-vapor interface as shown in Figure 20 b). Even though it is found that $(\Delta c/c_0)_{max}$ decreases with increasing *K* and thus spinning speed because the solute enrichment at the surface will decrease due to 1.) spinning-off, which reduces the film thinning time and thus the time for the selective evaporative surficial solute enrichment time and 2.) more efficient diffusional transport because of a thinner film.

The amount of the concentration difference can be written as a simple equation

$$\Delta c_{\max} = c^* \cdot c_0 \cdot D^{\alpha} \cdot E^{\beta} \cdot K^{\gamma}. \qquad (24)$$

The parameter and exponents are obtained from the fits.

c*	0.49 ± 0.05
α	-0.79 ± 0.04
β	1.04 ± 0.04
γ	-0.26 ± 0.02

Assuming "even" exponents the equation writes as

$$\Delta c_{\max} \cong 0.5 \mu m^{-3/4} \cdot c_0 \cdot D^{-3/4} \cdot E \cdot K^{-1/4}. \qquad (25)$$

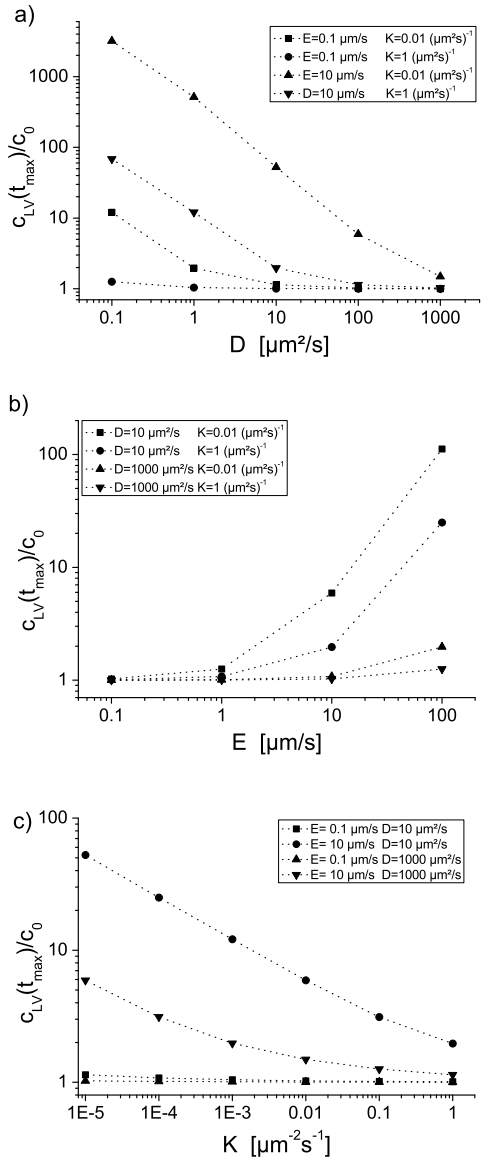

Figure 21: Concentration at the liquid-vapor interface in the moment of maximal concentration difference in the film as a function of a) the diffusion constant *D*, b) the evaporation rate *E* and c) the spinning parameter *K*.

The maximal concentration difference $(\Delta c/c_0)_{max}$ appears at the time t_{max}. For the description of concentration dependent processes as e.g. nucleation and growth the concentration c_{LV} at the liquid-vapor interface at the moment of maximal concentration difference t_{max} is most important.

It is found that the top concentration decreases with increasing diffusion constant D and increasing spinning parameter K. For increasing evaporation rate E the top concentration increases. The reasons for all three observations are basically the same as discussed before. Unlike for the concentration difference no easy scaling law is observed.

The film height in the moment t_{max} of maximal concentration difference $(\Delta c/c_0)_{max}$ is shown in Figure 22. Together with the actual difference this is a measure for the concentration gradient and thus for the inhomogeneity in the film (i.e. how far minimal and maximal concentration are apart). Furthermore the height gives the distance between the two active sites in the film. If for example a heterogeneous nucleation process at the substrate surface occurs at the same time as a nucleation process in the solute enriched top layer the height $H(\Delta c_{max})$ is the distance that separates them. If the height is rather big the two processes will not influence each other too much whereas close processes compete for the solute material.

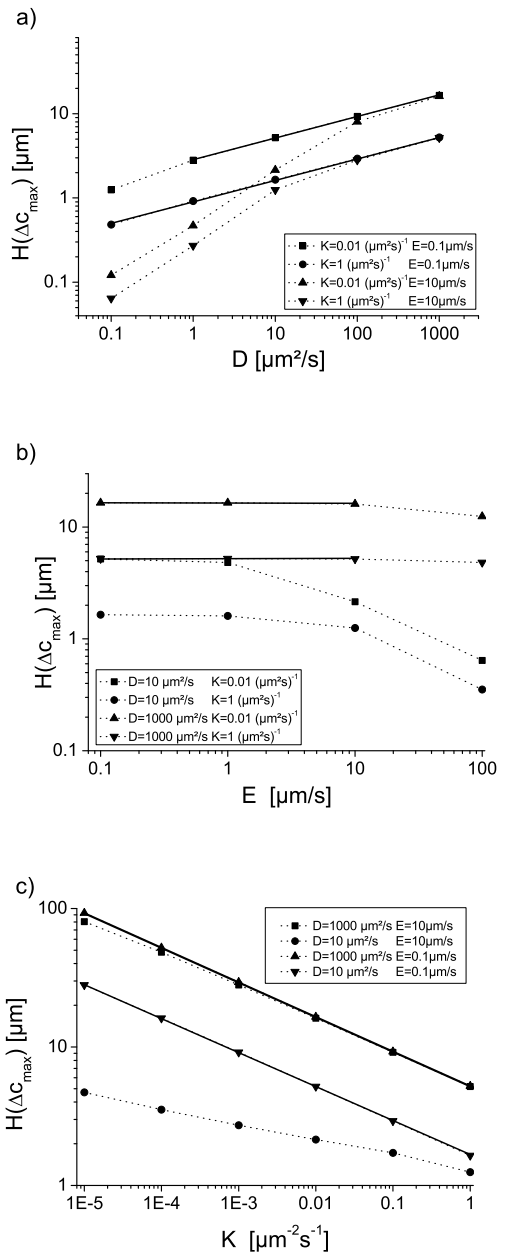

Figure 22: Film height at the time t_{max} of maximal concentration difference as a function of a) the diffusion constant *D*, b) the evaporation rate *E* and c) the spinning parameter *K*.

The heights $H(\Delta c_{max})$ increase for increasing diffusion constants (cf. Figure 22 a)). As the diffusion becomes more efficient with higher diffusion constants the transport of solute material is efficient even over longer distances. This effect is likewise observed in Figure 22 b) where $H(\Delta c_{max})$ is independent of E if the diffusion constant is high enough. For smaller diffusion constants $H(\Delta c_{max})$ decreases with increasing evaporation rate. Then the Stefan condition is not fulfilled. The general relation for $H(\Delta c_{max})$ is that it decreases when the spinning parameter K increases (Figure 22 c)). Straight lines with similar slope are observed if the evaporation rate is not too high and the diffusion constant is high enough. If the Stefan condition is fulfilled (straight lines in Figure 22) the relation writes as

$$H(\Delta c_{\max}) = H^* \cdot D^{\lambda} \cdot K^{\tau}. \qquad (26)$$

Out of the fit the following parameters are obtained.

H^*	1.01 ± 0.02
λ	0.246 ± 0.031
τ	-0.257 ± 0.008

Therefore the height of maximal concentration difference for ideal evaporation and diffusion conditions is

$$H(\Delta c_{\max}) = D^{1/4} \cdot K^{-1/4} \qquad (27)$$

As discussed before height and time are bijective and can be used to describe the process analogously. The moment when the maximum occurs is important as concentration dependent processes like nucleation and growth are time dependent as well. Therefore the time t_{max} indicates how much time is left for the process to occur before the film is completely evaporated. These data are shown in Figure 23 normalized to the total spin-casting time t_∞ (cf. equation (17)). The time axis was chosen that the process starts at 0 % and 100 % t_∞ is the moment when all solvent is evaporated.

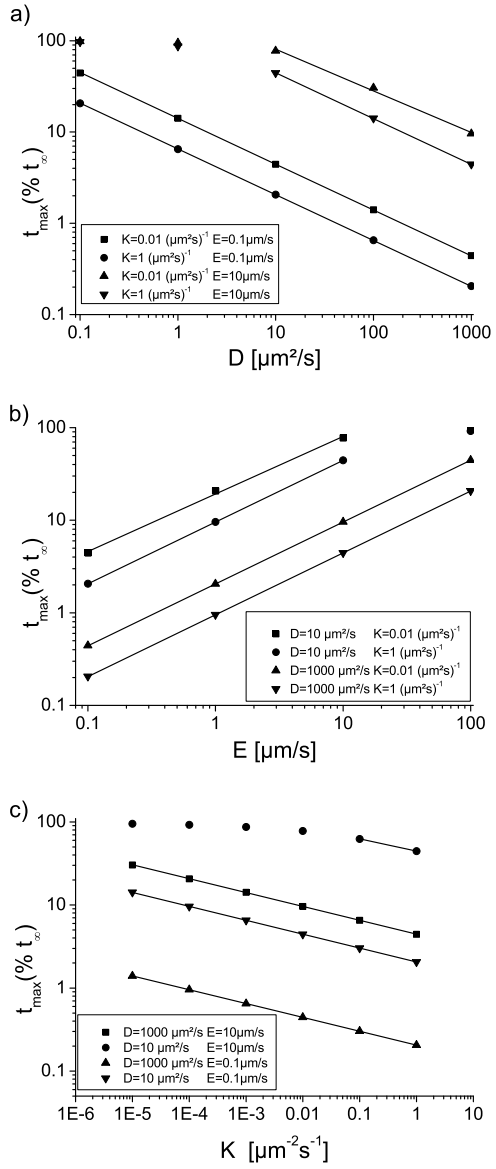

Figure 23: Times of maximal concentration normalized to the total process time as a function of a) the diffusion constant *D*, b) the evaporation rate *E* and c) the spinning parameter *K*.

The times in Figure 23 are transformed to fractions of t_∞ as this results in mostly linear graphs whereas the representation in real time is rather non-linear due to the complex structure of Equation (15). The time decreases (earlier with respect to the total time) if the diffusion constant D or the spinning parameter K is increased. Furthermore high diffusion constants effectively homogenize the solute concentration and with higher diffusion this is most effective even for thicker films and thus earlier. For higher evaporation rates the top enrichment is higher and the film has to be thinner for effective diffusion through the film. Therefore the maximal concentration difference shifts to later times with higher evaporation rates. In the case of the higher spinning parameter K the film thins much faster. Hence the diffusion is effective more early.

Another important fact is that the general appearance of the graphs is comparable to the one of the maximal concentration differences. This means high concentration differences coincide with late appearance. This results from the fact that the later the maximum is reached the longer the top layer was fed and therefore the concentration is higher.

The logarithmic dependences are valid if the maximum appears before approximately 80 % t_∞. Only the data before this time were used for the fit as indicated in the plots. The relation can be written as

$$t(\Delta c_{\max}) = t^* t_\infty \cdot D^\delta \cdot E^\varepsilon \cdot K^\kappa . \qquad (28)$$

Out of the fit the following parameters are obtained.

t^*	1.46 ± 0.02
Δ	-0.489 ± 0.023
E	0.656 ± 0.023
κ	-0.162 ± 0.010

With “even” exponents the equation is written as

$$t(\Delta c_{\max}) \cong 1.46 \mu m^{1/6} s^{1/12} \cdot t_{\infty} \cdot E^{2/3} \cdot K^{-1/6} \cdot D^{-1/2} . \tag{29}$$

4.6 Analytical Solution of Spin-Casting[c]

Complementary to the simulation the process was described analytically. In the scope of an ideal Newtonian liquid with no-slip at the solid substrate and no stress at the free surface the radial velocity field u (r and z are the radial and vertical coordinates) is given as[51]

$$u(r,z) = 3Krz\left(H - \frac{z}{2}\right). \tag{30}$$

The spin-off parameter K and the film height H are used analogously to chapter 4.3. The corresponding radial volumetric flux Φdz is

$$\begin{aligned} \Phi dz &= 2\pi r u(r,z) dz \\ &= 6\pi K r^2 z H\left(h - \frac{z}{2}\right) dz \end{aligned} \tag{31}$$

The continuity equation has to be fulfilled and the vertical movement of the stream lines due to thinning is obtained

$$\frac{dZ}{dt} = -\frac{1}{2\pi r}\int \partial_r \Phi dz = -Kz^2(3H - z). \tag{32}$$

This equation describes all stream lines across the spinning film and in particular the vertical motion of the topmost streamline $z = H$ which is equal to the height evolution of a spinning film[51]

$$\frac{dH}{dt} = -2KH^3 . \tag{33}$$

When the evaporation rate is subtracted equation (13) is obtained. The concentration equation for the spinning film is

$$\partial_t c = D\partial_z^2 c - \frac{dZ}{dt}\partial_z c = D\partial_z^2 c + Kz^2(3H - z)\partial_z c . \tag{34}$$

The boundary conditions for this differential equation are

[c] The analytical solution was developed in cooperation with Stefan Karpitschka.

$$D\partial_z c\big|_{z=H} = Ec\big|_{z=H}, \tag{35}$$

$$\partial_z c\big|_{z=0} = 0. \tag{36}$$

This means that the vertical diffusion at the free surface is equal to the evaporation (Stefan condition) and no solute diffuses through the substrate. When the differential equation is solved in its present form problems arise due to the moving boundary condition (equation (35)). This can be avoided by introducing the rescaled coordinate $y = z/H$ ($y \in [0, 1]$, from substrate to surface)

$$(\partial_t y)\partial_y c + \partial_t c = D\left((\partial_z^2 y)\partial_y c + (\partial_z y)^2 \partial_y^2 c\right) - \frac{dZ}{dt}(\partial_z y)\partial_y c. \tag{37}$$

Substituting known relations yields

$$\partial_t c = \frac{D}{H^2}\partial_y^2 c + \left(KH^2 y^2 (3-y) - \frac{y}{H}\left(2KH^3 + E\right)\right)\partial_y c. \tag{38}$$

The first term in this equation results from the diffusion, the second from the vertical motion of the stream lines and the third from virtual vertical motion due to the rescaling of z.

As no explicit dependence $H(t)$ is known (cf. discussion in chapter 4.3) this equation cannot be solved directly. Using the bijective property of $H(t)$ the time variable is changed to H. Then the equation does not describe the concentration at a given time but at a given height H. It can afterwards be transferred into time using equation (15). As the height is constantly falling the time-to-height relation is biunique.

$$\partial_h c = -\frac{DH^{-2}}{2KH^3 + E}\partial_y^2 c - \left(\frac{KH^2 y^2 (3-y)}{2KH^3 + E} - \frac{y}{H}\right)\partial_y c \tag{39}$$

The adopted boundary condition is

$$\frac{D}{H}\partial_y c\big|_{y=1} = Ec\big|_{y=1}. \tag{40}$$

As ideal solutions are assumed the initial concentration is a pure factor and the initial condition is

$$c\big|_{H=H_0} = 1. \tag{41}$$

Equation (39) can be solved rather easily with standard software. The results perfectly match the ones of the completely numerical simulation. The obtained parameters are given in Table 4.

Table 4: Comparison of the analytic and simulation results for the spin-casting process.

Analytical results	Results from simulation
$\frac{N}{A} \cong 0.8 \cdot c_0 \cdot K^{-1/3} \cdot E^{1/3}$	$\frac{N}{A} \cong 0.8 \cdot c_0 \cdot K^{-1/3} \cdot E^{1/3}$
$\Delta c_{\max} \cong 0.46 \mu m^{-3/4} \cdot c_0 \cdot D^{-3/4} \cdot E \cdot K^{-1/4}$.	$\Delta c_{\max} \cong 0.5 \mu m^{-3/4} \cdot c_0 \cdot D^{-3/4} \cdot E \cdot K^{-1/4}$
$t(\Delta c_{\max}) \propto \left(E / K^{1/4}\right)^{0.7} \cdot K^{-1/6} \cdot D^{-1/2}$	$t(\Delta c_{\max}) \cong 1.46 \mu m^{1/6} s^{1/12} \cdot t_\infty \cdot E^{2/3} \cdot K^{-1/6} \cdot D^{-1/2}$
$H(\Delta c_{\max}) = D^{1/4} \cdot K^{-1/4}$	$H(\Delta c_{\max}) = D^{1/4} \cdot K^{-1/4}$

4.7 Experimental Results on Nucleation Processes During Spin-casting

4.7.1 General Aspects of Nucleation in Inhomogeneous Films

The simulations reveal that within a film of solution that is spun and subject to evaporation a concentration difference evolves during the spin-casting process. Depending on its magnitude the concentration gradient across the film may give rise to interesting effects. One effect might be the *inversion of the nucleation*. As described in chapter 2.2 the nucleation is favored by wetting surfaces as the nucleation barrier is decreased drastically. Therefore in systems with wetting interfaces the heterogeneous nucleation will always dominate over homogeneous nucleation as long as the physical and chemical conditions are uniform. In a flat film on a wetting substrate this will be at the solid-liquid interface. If instead the concentration is non-uniform and the solute enriches at the surface the homogeneous nucleation in the top region of the film might be favored over homogeneous interface nucleation. A third option is the nucleation at the top liquid-vapor interface which is heterogeneous as well. Still this represents a nucleation inversion if the contact angle of the solute at the solid interface is smaller than the contact angle at the liquid-vapor interface.

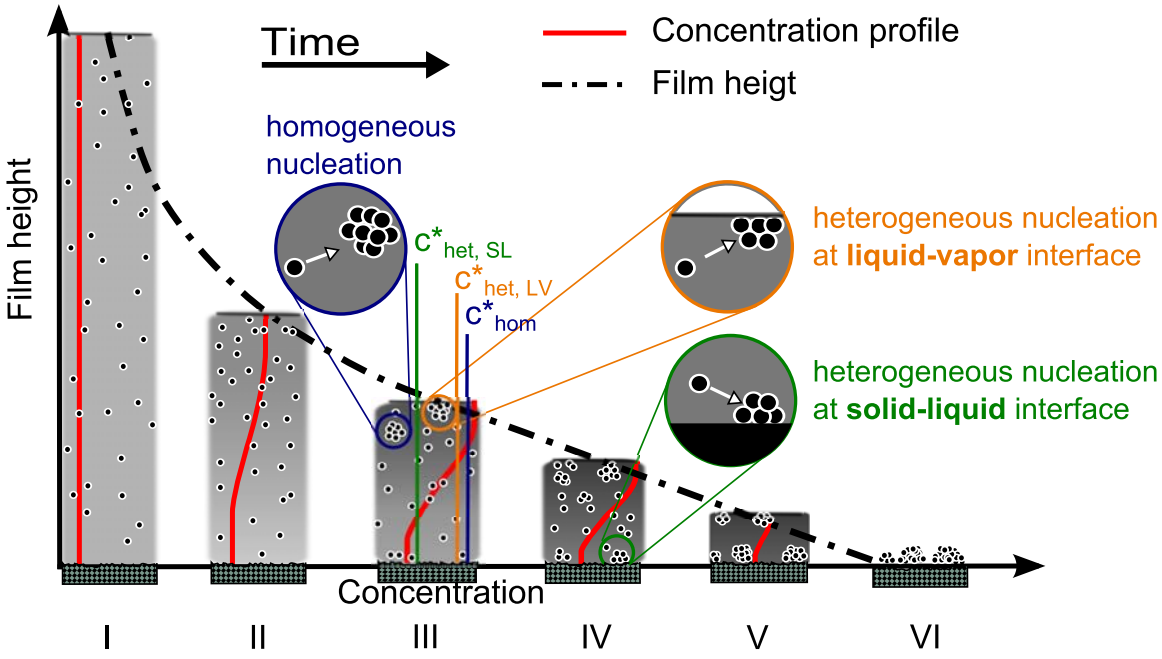

Figure 24: Scheme of inversed nucleation during spin-casting (cf. Figure 12 on page 20). The concentration profiles across the film are shown in red, the critical concentration for heterogeneous nucleation at the solid-liquid interface $c^*_{het,SL}$ is marked in green, critical concentration for heterogeneous nucleation at the liquid-vapor interface $c^*_{het,LV}$ is marked in orange and the critical concentration for homogeneous nucleation in the bulk c^*_{hom} is indicated in blue.

Figure 24 shows schematically the stages of an inversed nucleation process during spin-casting. In the beginning (stage I) the film has a uniform concentration well below the critical concentrations for nucleation. When the evaporation is significant versus the spin-off a concentration gradient evolves across the film (stage II). The film decreases in height and the top concentration increases above the critical concentration for both, homogeneous nucleation c^*_{hom} and heterogeneous nucleation at the liquid-vapor interface $c^*_{het,LV}$ (stage III). Now the heterogeneous nucleation at the liquid-vapor interface and homogeneous nucleation start and aggregates or crystals grow in the top layer of the film while no nucleation takes place at the solid-liquid interface. With progressing time the film gets thinner and the total concentration increases (stage IV). Now the concentration at the bottom passes the critical concentration for heterogeneous nucleation at the substrate $c^*_{het,SL}$. Then the nucleation and growth processes act at the same time and compete for solute (stage V). When all solvent is evaporated the aggregates or crystals from all processes are deposited on the substrate.

4.7.2 AFM Results

The challenge when trying to prove or disprove the hypothesis of inversed nucleation is that one has to be able to differentiate between the species originating from either of the three nucleation pathways. This is in particular difficult as nuclei are very small in size. Furthermore stable nuclei continue growing, so the initial nucleus is buried in the aggregate. As long as the two processes do not result in different aggregate or crystal types (and there is no a priori argument why they should do so) the two types can not be distinguished from their structure. The only difference might be in shape or size if one nucleation process is more efficient or the growth process is either hindered or favored by the concentration conditions. In the case of spin-casted fullerenes (C_{60} in toluene

solution, spin-casted at 3000 rpm in flow hood) the analysis of the aggregates shows a bimodal distribution of the sizes. This is shown in Figure 25.

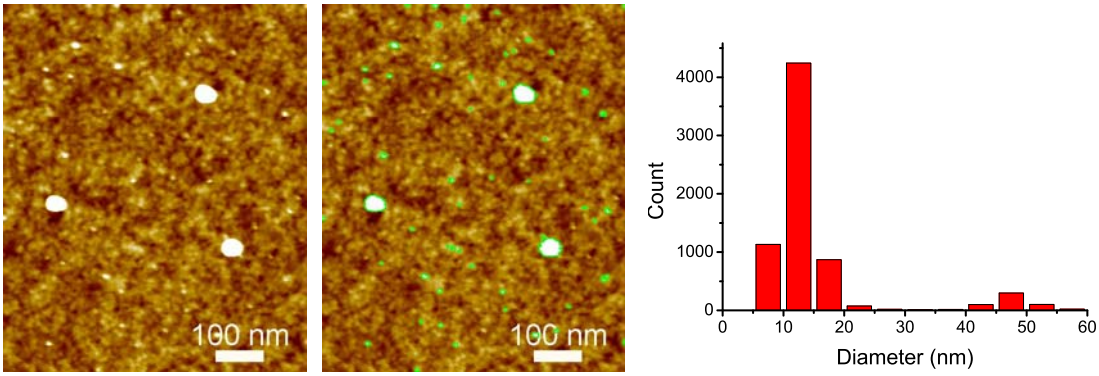

Figure 25: AFM scan of C_{60} fullerenes spin-casted on hydrophilic silicon oxide wafer (left), with indicated aggregates (center) and statistical analysis of the sizes of the aggregates (right).

The total area analyzed for the statistics is more than 250 µm² scanned with a pixel resolution of 2 nm! The two populations are clearly separated by approximately 35 nm in radius. Obviously small and big aggregates originate from two different processes. The question which of the two species was nucleated where can be answered by carefully investigating the obtained aggregates as some of the big ones have small aggregates sitting on top as seen in Figure 26. This proves that the small aggregates are built in higher regions of the spin-casted film.

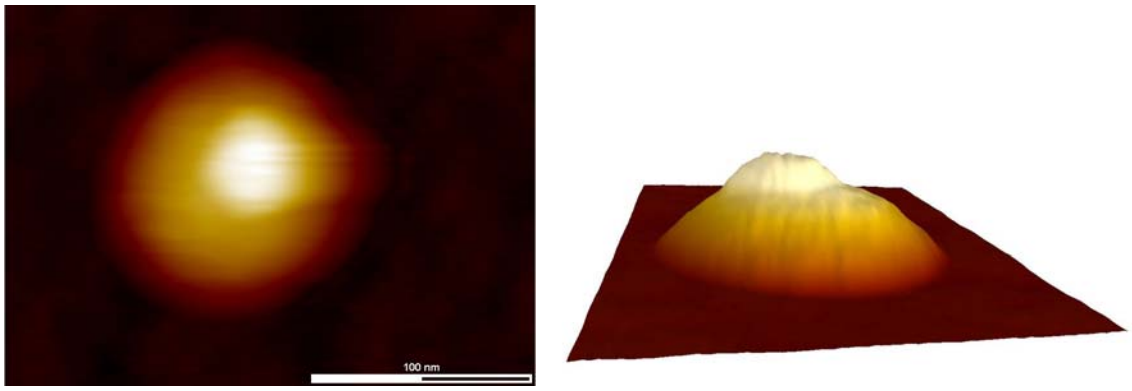

Figure 26 Left: AFM image of C_{60} fullerene aggregate produced by spin-casting with additional aggregate sitting on top. Right: 3D image of the same aggregate. The z-axis is stretched by 2.

Three scenarios are possible to obtain nuclei in different height regions:

1.) The big aggregates are nucleated at the substrate and the small ones are built in the high concentrated top region of the spin-casted film by *homogeneous* nucleation in the bulk or

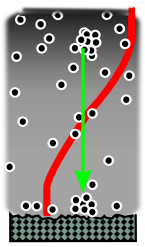

cf. Figure 24

2.) the big aggregates are nucleated at the substrate and the small ones are built in the high concentrated top region of the spin-casted film by *heterogeneous* nucleation at the liquid-vapor interface or

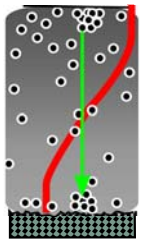

3.) the big aggregates are formed homogeneously in the high concentrated bulk region and the small ones are formed heterogeneously at the liquid-vapor interface.

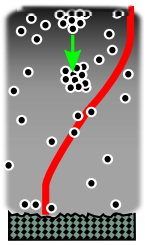

The third option is rather unlikely as the final aggregate is obviously frozen in a non-equilibrium state. The time for a complete fusion process is obviously not enough before all solvent is evaporated. But in scenario 3 the two initial aggregates should fuse and no boundaries should be visible.

4.7.3 Voronoi Analysis

In order to distinguish between the first two options further analysis is needed. One way is to analyze the influence of the distance of the aggregates on their size as the competition of neighboring aggregates for supply will result in a relation between size and distance. The distance in the two dimensions is represented by the Voronoi cell. This technique allocates to each particle the area where the particle is the closest. A Voronoi cell can be considered as the collection area for each aggregate due to diffusion. An example is shown in Figure 27 when all or only big particles are considered.

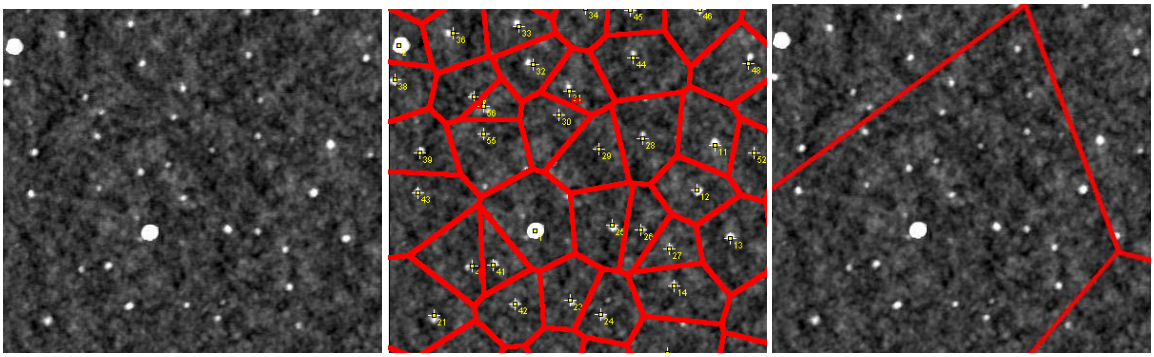

Figure 27 Left: AFM image with distribution of C_{60} aggregates. Middle: Voronoi cells for all aggregates higher than 1 nm without selection of the size. Right: Voronoi cells of aggregates bigger than 40 nm in diameter.

The growth of the aggregates is fed by diffusing particles. The area or volume out of which the diffusing particles can contribute to the aggregate growth is spherical or circular with the diffusion length as radius. If the nucleation sites are closer than the diffusion length the spherical or circular areas overlap and the result are the Voronoi cells. For complete aggregation of the particles the result will always be Voronoi cells as in a

region that is not part of an existing cell the increasing concentration will lead to a new nucleus and a new cell.

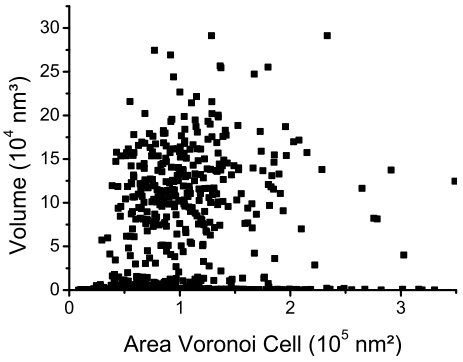

Figure 28: Volume of C_{60} aggregates as a function of the attributed Voronoi cell area. No preselection of the analyzed particles was conducted.

If a simple hit-and-stick mechanism for the aggregates is assumed the aggregate volume should scale with the Voronoi area as it is linked to the size of the reservoir. The resulting graph for the Voronoi analysis of all C_{60} aggregates is shown in Figure 28. No obvious relation is detected if all particles are considered. The particles with bigger radius (higher volume) are found for a broad range of Voronoi cell areas but seem to be centered around 10^5 nm². No clear tendency is visible.

If the analysis is divided and performed independently for the two populations of aggregates (small and big, cf. Figure 25) the result is different. The graphs are shown in Figure 29.

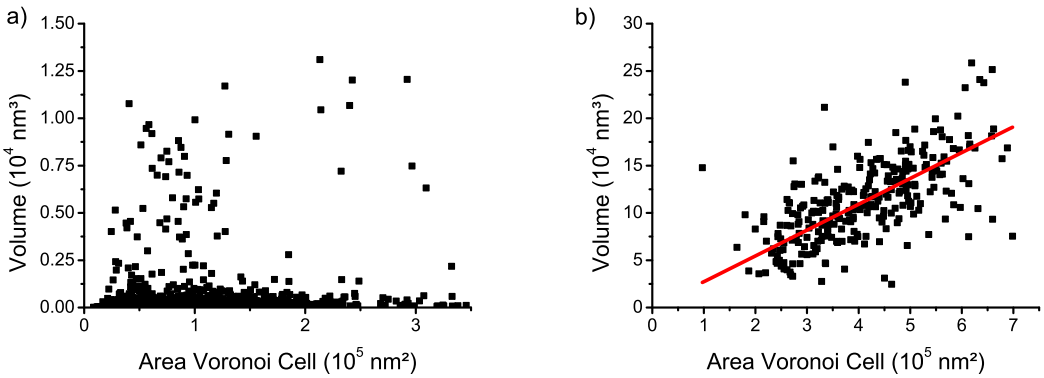

Figure 29: Volume of C_{60} aggregates as a function of the attributed Voronoi cell area. Only particles with a radius of a) less than 30 nm or b) more than 40 nm were analyzed. The red line is a linear fit of the particles though the origin.

Again, the plot obtained for particles smaller than 30 nm in radius (Figure 29 a)) does not show any specific order. In general the particles are significantly smaller in volume but the Voronoi cells are of comparable size as in Figure 28. In contrast the Voronoi cells for the individually analyzed particles with a radius bigger than 40 nm (Figure 29 b)) are much bigger. This is due to the fact that the total area is divided in far less cells. But more important the volume scales with the Voronoi cell area. Despite the variation of the

obtained volumes a linear fit (red line) with a slope of 0.027 nm seems suitable. However, the scaling law is not obvious.

For heterogeneous and homogeneous nucleation the finally obtained distribution of aggregates is fundamentally different. If the aggregates are initiated by *homogeneous* nucleation the corresponding volume that feeds the growth is the 3D Voronoi cell. Hence it is the 3D Voronoi cell volume that determines the final size of the aggregate as shown in Figure 30 (left). When the aggregates are deposited at the surface the information of the initial distance/volume is lost as indicated in the right sketch of Figure 30. This effect is comparable to the fact that the distance of stars cannot be deduced from its apparent distance on the sky.

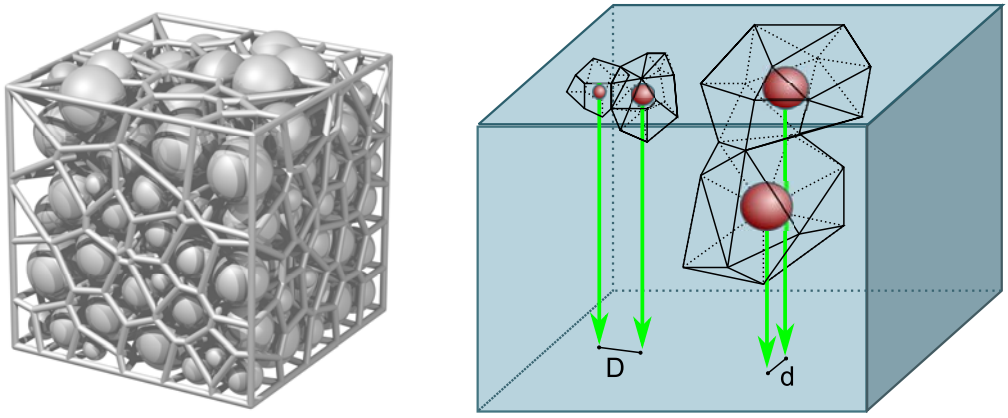

Figure 30 Left: Example of 3D Voronoi tessellation (from: http://math.lbl.gov/voro++/examples/). The size of the spheres in the cells corresponds to the cell volume. The size of the spheres is exaggerated compared to the aggregate volume. Right: Projection of the Voronoi cells onto the surface. The distance on the surface is not a measure for the initial distance in the bulk ($d < D$).

For *heterogeneous* nucleation at a surface with a thick liquid bulk film two general behaviors have to be distinguished as shown in Figure 31. In the typical case the aggregate grows by particles that attach from the bulk film (3D diffusion). Then the volume of attraction is hemispherical and the scaling law is $V \propto A^{3/2}$. 2D diffusion is obtained if it is energetically favorable for the particles to attach to the substrate surface without chemical bonds. Then they remain mobile and the movement of the attached particle is then limited to the surface. The size of the aggregates then scales linearly with the area of the Voronoi cell.

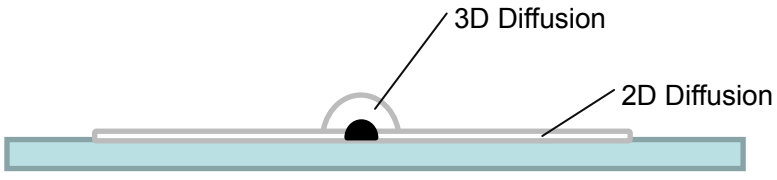

Figure 31: Ideal diffusion behavior of particles that feed the growth of surface nucleated aggregates. In the 3D case the collection region for diffusing particles is a hemispherical space around the particle. In the 2D regime the particles attach to the surface while remaining mobile.

Even though a straight line is obtained in Figure 29 b) which indicates 2D diffusion this conclusion might fall short in the specific case of spin-casting. The confined geometry might influence the 3D diffusion scaling law. As discussed the maximal distance of the nuclei is the diffusion length (Figure 32 a)). Usually the nucleation sites will be closer

than the diffusion length and the hemispheres overlap laterally. In a film this results in pillars with the Voronoi cell as ground area and a curved top surface (Figure 32 b)). Already this will give a scaling law that is more linear than the initially predicted $V \propto A^{3/2}$. If the film in the moment of nucleation is thinner than the diffusion length all pillars have the same height (Figure 32 c)). Then their volume and hence the final aggregate volume scales only with the ground area which is the Voronoi cell. It is therefore most likely that the population of big aggregates was nucleated at the interface of the solid substrate but the regime of 3D nucleation was maintained.

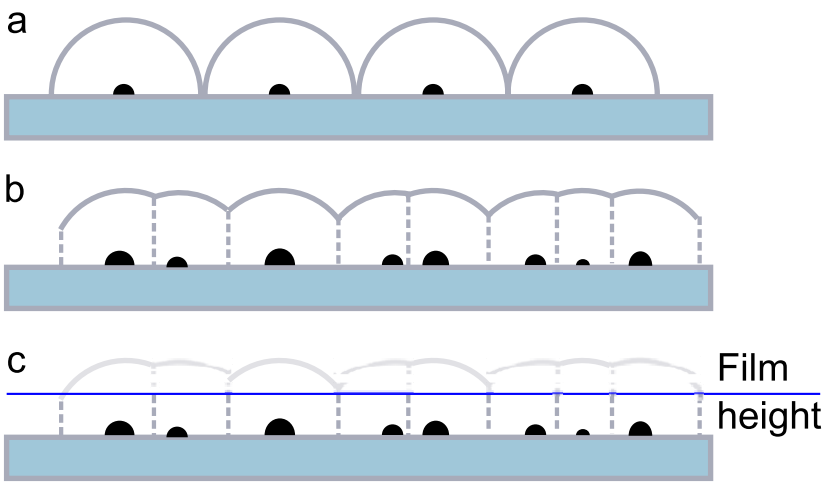

Figure 32: a) Close packing of hemispherical diffusion regions. b) Overlapping hemispheres resulting in pillars with Voronoi cells at the solid interface and curved top surfaces. c) Confined geometry in thin films leads to pillars of equal height and Voronoi cell as base area.

The presented arguments apply in particular for the presented data of spin-casted C_{60} fullerenes. Their diffusion constant in organic solvents as benzene is 91 µm²/s[64] (should be similar for toluene). For typical setup (3000 rpm, 10^{-6}M C_{60} in toluene on SiO_2, contact angle 30°) the critical concentration at the solid surface is[64]

$$c_{crit,het} = c_{crit,\mathrm{hom}} \cdot f(\theta) = 0.8 \cdot 10^{-4} \frac{Mol}{l} \cdot f(30°) = 1.03 \cdot 10^{-5} \frac{Mol}{l}. \quad (42)$$

Here $f(\theta)$ is the influence of the contact angle on the nucleation barrier (cf. equation (5), page 5). The critical concentration is reached at the solid interface 0.01 s before the film completely vanishes at a film height of 312 nm. If this value is compared to the 954 nm the fullerene can diffuse in the given time, the assumption of a confined geometry depicted in Figure 32 is correct.

It remains to differentiate the two possible nucleation pathways for small aggregates that are built above the big ones either by heterogeneous or homogeneous nucleation. If the nucleation is *heterogeneous* at the top interface the same arguments as discussed above apply. Again the nuclei are formed at an interface and the relation between aggregate volume and Voronoi cell should be dependent. The obtained distribution of aggregates from the liquid-vapor interface is deposited on the distribution of big aggregates at the solid-liquid interface as depicted in Figure 33. This deposition maintains the distribution for each population but results in random Voronoi cells if both populations are analyzed at the same time.

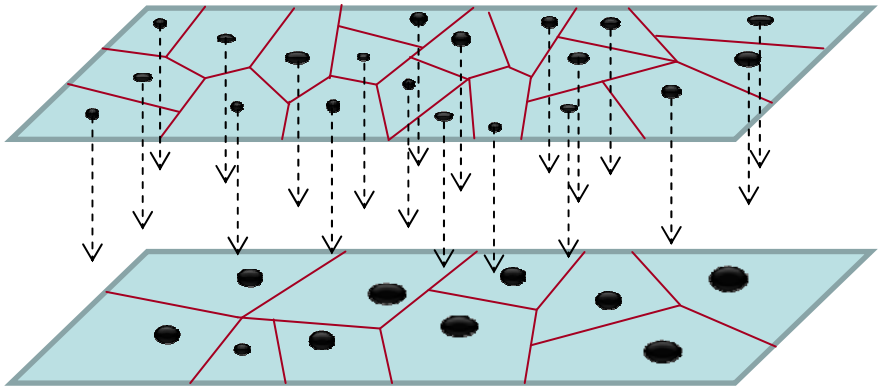

Figure 33: The heterogeneously nucleated aggregates at the liquid-vapor interface are deposited onto the aggregates at the solid surface. The volume-to-area relation for each distribution is maintained.

This process assumes that the particles remain at the relative position of nucleation. This is true to some extent as the spreading due to spinning is already negligible when the concentration rises to relevant regions. Even if spin-off would still be relevant it would in general result in a global enlargement of the Voronoi cells but conserve its general structure. However, no contribution of the diffusion was yet included. As the initial stable nuclei are rather small this can lead to the loss of the distance structure. An estimation whether the diffusion is relevant can be obtained when the typical distance of the nuclei and the diffusion length are compared. According to Einstein[65] the distance l a particle typically diffuses in 3D within a given time t is

$$l^2 = 6Dt\,. \tag{43}$$

An aggregate with a diffusion constant of 1/10 D_{C60} moves approximately 740 nm in 0.01 s. This is considerably more than the typical distance of Voronoi cell centers ($l_{Voro} \approx \sqrt{\text{Area Voronoi Cell}} = \sqrt{20000\ nm^2} = 141\ nm$). This would explain the random distribution obtained for the small aggregates (as seen in Figure 29 a)). Another explanation of this distribution is the origin from homogeneous nucleation (cf. Figure 30). Hence with the provided data no clear conclusion can be drawn as long as the contact angle of fullerenes at the liquid-vapor interface is unknown.

4.8 Discussion and Outlook

The results obtained for spin-castings via simulation and analytical treatment match perfectly. However, only ideal cases are treated so far. But the most important properties of real solutions are certainly recovered in the present form. They offer the possibility to explain different species of aggregates in otherwise homogeneous films. The findings provide easy scaling laws for the final coverage and the maximum concentration difference across the film as well as the time and the height when the maximum concentration is reached. The presented results are also relevant for further deposition techniques that involve drying from a solution as spray- or dip-coating or doctor-blading. Future applications of the simulation will include the possibility to deal with concentration dependent parameters for the viscosity or to model nucleation in the film.

In the experimental part it was essentially shown that C_{60} fullerenes form two distinct species of aggregates when deposited from spin-casting. The two kinds do not only differ in size but also in their relation of volume and the distance to the neighbors. Out of these distributions it was concluded that the big particles are formed by heterogeneous nucleation at the solid substrate interface whereas the small aggregates are most likely formed by homogeneous nucleation in the bulk liquid. The provided data are consistent with this theory. Still it has to be noted that the discussion was limited to ideal nucleation types. From the provided data further options of aggregate formation cannot be excluded. For example the small particles could originate from heterogeneous nucleation at impurities in the bulk solution. This was tried to exclude by using high grade solvents for HPLC but even some fractions of a percent in weight would provide enormous amounts of nucleation sites. Another source of different aggregate types would be chemical reactions of C_{60} fullerenes. As C_{60} tend to cross-link in the presence of oxygen one could think of aggregates that form at the liquid-vapor interface due to oxidation. Then the requirement of a critical size does not apply as the chemical bond inhibits the disintegration. However, one would expect higher contact angles for cross-linked aggregates as their internal structure is more rigid which will constrain the attachment to the solid surface. Though the concept of homogeneous and heterogeneous nucleation seems most likely but further experiments are necessary to finally exclude other possibilities.

Future experiments will include spin-casting in controlled atmospheres. Then the vapor pressure and thus the evaporation rate can be influenced which will prove or disprove its influence. The influence of the nucleation at the liquid-vapor interface can be investigated by venting the chamber with water vapor. This polar molecule alters the interactions and therefore the contact angle at the liquid-vapor interface. Additionally the hypothetical influence of cross-linking could be excluded by spinning in an oxygen-free atmosphere. Furthermore the temperature should be monitored during spin-casting as in particular for fullerenes the solubility is temperature dependent. Other molecules than C_{60} should be considered additionally in future experiments. The very limited choice of applicable solvents for C_{60} limits the possibility to change the solvent. This would allow changing the diffusion constant of the solute.

Additionally the theoretical discussion should be broadened and kinetics should be included. As the rate at which the supersaturation is reached at the top and bottom interface is known it should be possible to predict the respective nucleation rates. The amount of obtained nuclei can then be analyzed and used to test the validity of the theoretical predictions.

5 Size-dependent contact angles of sessile droplets[d]

5.1 Summary

Although contact angles are often considered and applied as system immanent constants more and more research focuses on the deviation from this oversimplification. In general this is described with a line tension effect. Here a new approach is presented where the deviations in the contact angle are derived from the interactions on a molecular level. The considered interaction is the disjoining pressure and the obtained interaction parameter can be identified with the reduced Hamaker constant if the interactions are non polar. The Hamaker constant for sessile droplets on planar wetting substrates can be calculated very easily from the contact angle as shown in the third section of this chapter. Then the well-known concept of line tension is repeated followed by the presentation of the newly developed concept of size-dependent contact angles as a consequence of disjoining pressure. Finally both approaches are compared to experimental results.

[d] Some of the experimental results are published by Berg, Weber and Riegler in PRL[50].

5.2 Introduction

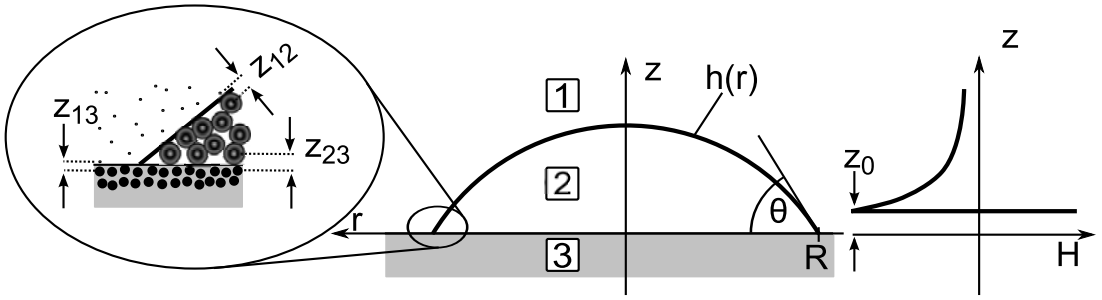

Figure 34: Spherical cap shaped droplet consisting of phase 2 in a medium 1 on a solid surface 3. The droplet has a profile *h(r)*, a contact angle θ, a cut-off length z_0 and is influenced by a disjoining pressure *H*.

In partially wetting systems (spatially limited gas or liquid phase 2 attached to a flat solid surface 3, surrounded by a gas or liquid phase 1 as shown in Figure 34) the most important parameters to describe the shape of the sessile droplets are its radius and contact angle. According to Young[66] the contact angle can be calculated from interfacial tensions which are material constants. Hence the contact angle can be considered as a system parameter. It is therefore used in lots of theoretical physical relations as well as technological applications. The value used for both purposes is usually the *macroscopic* contact angle θ_∞ (obtained from macroscopic drops) which is considered to be universal. More close investigations of the stability of sessile droplets show that the calculations leading to Young's equation are somehow oversimplified and ignore effects that make the *microscopic* contact angle θ (contact angle of small drops) size-dependent. The consequences of size-dependent contact angles are especially crucial for nucleation as the energy barrier of nucleation depends on the contact angle (c.f. equation (5)) and a growing nucleus will always pass the relevant size regions.

5.3 Relation of Contact Angle and Hamaker Constant in Partial Wetting

If the intermolecular interactions are limited to dispersion forces, the surface tensions as well as the interaction Hamaker constant of the three-phase system can be expressed as Hamaker constants of the individual interfaces[67,68]

$$\gamma_{ij} = \frac{A_{ii} + A_{jj} - 2A_{ij}}{24\pi z_{ij}^{\,2}} \tag{44}$$

$$A_{ijk} = A_{jj} + A_{ik} - A_{ij} - A_{jk} \tag{45}$$

where i ,j ,k represent the phases 1, 2 and 3. The separation in z-direction of the centers of the interacting molecules z_{ij} is determined by the size of the molecules (building blocks) of the involved phases (cf. magnification in Figure 34) and is called cut-off length[67] in the following. The Hamaker constant for dissimilar materials can be expressed as the *harmonic* mean of the individual constants

$$A_{ij} = \frac{2A_{ii}A_{jj}}{A_{ii} + A_{jj}}. \tag{46}$$

This formula follows from the London equation and is exact. Unfortunately an inaccurate description using the *geometrical* mean is commonly accepted. Probably this dates back to Overbeek[69] who used the geometrical mean to simplify a binomial equation and stated: *"It has been assumed that* $A_{12} = \sqrt{A_{11}A_{22}}$*, which, though not exact, is certainly approximately correct."* Since then this approximation has spread widely and is even though used in standard textbooks. Still equation (46) should be used preferably.

The macroscopic contact angle can be expressed as a function of the surface energies (Young's equation). If the labeling of phases is chosen as shown in Figure 34 the macroscopic contact angle can be written as

$$\alpha = \cos(\theta_\infty) = \frac{\gamma_{13} - \gamma_{23}}{\gamma_{12}}. \tag{47}$$

If the phases consist of molecules of equal size $z_{ij} = z_0$ equations (44)-(47) can be combined and reduced dramatically. It is found that the ratio of Hamaker constant and interfacial tension (*reduced Hamaker constant*) can be written simply as

$$\frac{A_{123}}{\gamma_{12}} = 12\pi \cdot z_0^{\,2}(1-\alpha). \tag{48}$$

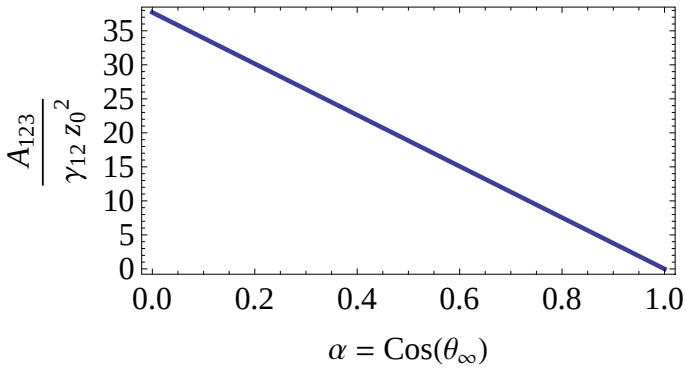

Figure 35: Reduced Hamaker constant as a function of the macroscopic contact angle.

This means a universal relation exists between the ratio of Hamaker constant A_{123} and surface tension and the macroscopic contact angle for a given cut-off length. The result is similar to the relation derived by Israelachvili[70] who again used the geometrical mean for the Hamaker constants instead of equation (46) followed by complex integration over the adsorbed films. Equation (48) is found but only as the first term in a series. In the above presented approach equation (48) is complete while the derivation is far easier.

The calculation holds for systems that consist of molecules of equal sizes and have then similar cut-off lengths. As discussed by Israelachvili[67] rather good predictions for the surface tension can be obtained for a universal cut-off length of 0.165 nm for a variety of liquids. This means that equation (48) is rather universal. If the involved substances have significantly different sizes the cut-off lengths in the surface tension definition will differ. If the molecule sizes of phase 1 and 3 are similar the only different cut-off length is the one for the 1-3 interface as shown in the inset of Figure 34. If it is assumed that

$z_{12} = z_{23} = z_0$ and $z_{13} = z_0/k$ the Hamaker constants do not cancel out and the contact angle can only be used to eliminate one of the Hamaker constants. Figure 36 shows the ratio A_{123}/γ_{12} for a given macroscopic contact angle of 30° and a molecular size factor k of 5. The change of the ratio is most pronounced, if the Hamaker constant of the vapor (phase 1) or the substrate (3) gets small.

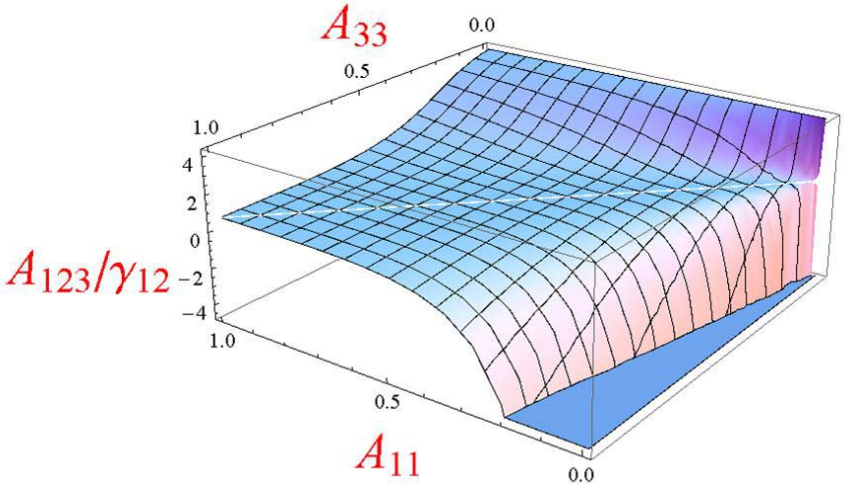

Figure 36: A_{123}/γ_{12} for different molecule sizes, a given contact angle of 30°, a liquid cut-off length of 0.4 nm and $k = 5$.

5.4 Classical Line Tension Approach

A condensed phase in equilibrium will always adopt the shape of the (local) energetic minimum. This requires the minimization of all involved energies including interfacial energies. As the latter are always positive the energy minimization implies the minimization of the interfacial area. Hence liquids or soft amorphous solids with no energetic contribution from crystallinity will have curved surfaces and will be spherical in the absence of further forces (steric hindrance, gravitation, etc.). If a liquid or soft amorphous matter is attached to a flat solid surface (sessile droplet) the energetic minimum is a spherical cap shaped droplet. For a droplet at energetic minimum the force balance at the three-phase line where all three interfaces meet results in Young's equation for the contact angle

$$\alpha = \cos\theta_\infty = \frac{\gamma_{13} - \gamma_{23}}{\gamma_{12}}. \qquad (47)$$

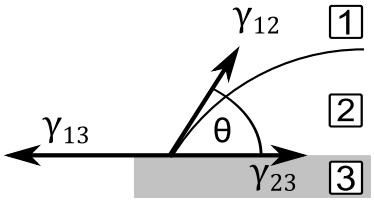

Figure 37: Force diagram resulting in Young's equation.

When Gibbs derived this equation in his famous work[71] he introduced dividing surfaces and compared the two kinds of energies of molecules: 1.) in the bulk and 2.) at the interfaces. He realized that the argument for positive interfacial tension (missing bonds at the interface) should consequently be extended to the molecules at the three-phase-line and wrote in a footnote: *"These lines might be treated in a manner entirely analogous to*

that in which we have treated surfaces of discontinuity. We might recognize linear densities of energy, of entropy, and of the several substances which occur about the line, also a certain linear tension." At the three-phase line the molecules miss even more bonds to their own phase but have contact to both other phases. It is not a priori obvious whether this energetic contribution is positive or negative. The calculations including the contribution from the three-phase line were made in 1968 by McLaughlin[72] and later by Gaydos and Neumann[73]. The additional energy term results in the line tension τ and the Modified Young's Equation is obtained

$$\cos\theta = \cos\theta_\infty - \frac{\tau}{\gamma_{12} R} = \cos\theta_\infty - \frac{\tau}{\gamma_{12}} \cdot \kappa \tag{49}$$

where R is the radius of the solid-liquid contact circle (three-phase line) and its inverse is the curvature κ. This equation is widely accepted and deviations of the macroscopic contact angle were subsequently attributed to the line tension. "Line Tension Effect" was even used synonymously for size-dependent contact angles. Still this equation remained under discussion and amongst others in 2007 Schimmele, Napiórkowski and Dietrich pointed out that the rather easy form of the Modified Young's Equation is thermodynamically inconsistent. A thorough analysis yields

$$\cos\theta - \cos\theta_\infty = -\frac{1}{\gamma_{12} R}\left\{\left(2\delta_{12}^T \gamma_{12} - \frac{d\tau}{d\theta}\right)\sin\theta_\infty \cos\theta_\infty - \tau - R\frac{d\tau}{dR}\right\}. \tag{50}$$

The additional parameters are δ_{12}^T the Tolman length of the liquid-vapor interface and the stiffnesses of the line tension against deformation $\frac{d\tau}{d\theta}$ and $\frac{d\tau}{dR}$. Even though equation (50) is consistent from a theoretical point of view its application for experimental data is very limited as the values for the stiffnesses depend of the applied choice of dividing interfaces and the Tolman length can only be obtained from theoretical computations. Therefore the line tension effect for size-dependent contact angles will be described via equation (49) were the line tension τ is considered the leading term approximation of equation (50).

Still, both equations describe a non-constant contact angle θ that deviates from the macroscopic contact angle θ_∞ in particular for small droplets. Besides nucleation[74,75], line tension is found to affect for instance droplet formation[76–78], attachment of small particles to fluid interfaces[75,79], formation of foam films[80], and the organization within biomembranes[81,82]. Theoretical studies[83–85] conclude that τ should be on the order of 10^{-10} J/m. Based on the theoretically estimated strength, line tension would only influence the contact angles of nanometer size droplets but most of the experimental studies up to now did not investigate droplets below radii of 100 nm.

5.5 Non-constant Contact Angles as a Consequence of Disjoining Pressure[e]

5.5.1 Derivation without slope dependent external energy

For a droplet with circular three-phase line on a planar surface with Van-der-Waals interaction the total energy E is

$$E(h) = 2\pi \left(\underbrace{\gamma_{12} \int_0^R r \sqrt{1 + \left(\frac{\partial h(r)}{\partial r} \right)^2}\, dr}_{\text{Surface}} + \underbrace{(\gamma_{13} - \gamma_{23}) \frac{R^2}{2}}_{\text{Interface}} + \underbrace{\int_0^R r H(h(r)) dr}_{\substack{\text{Disjoining} \\ \text{Pressure}}} \right) \tag{51}$$

where $h(r)$ is the height profile of the droplet, R the radius of the three-phase contact line and γ_{ij} the tensions of the surfaces dividing solid, liquid and vapor, respectively (e.g. 1-vapor, 2-liquid, 3-solid, cf. Figure 34). $H(h(r))$ is the excess energy[86] resulting from the interactions of molecules in the involved phases (e.g. dispersive, polar and electrostatic force). The first integral represents the interfacial energy of the curved top surface of the droplet, the second term is the energy of the planar interface of solid and liquid. The last integral describes the interaction (excess) energies. In the presented form $H(h(r))$ is used instead of $H\left(h(r), \left. \frac{\partial h(r)}{\partial r} \right|_{r=R} \right)$. This means the energy is limited to the contribution that acts through the droplet (internal energy[68]) and the dependence on the contact angle at the contact line is ignored. Therefore the derivation strictly holds true only for small macroscopic contact angles. With these simplifications the disjoining pressure is written as

$$H(h(r)) = -\frac{C}{12\pi (h(r) + z_0)^2} \tag{52}$$

where C is the interaction constant and z_0 the cut-off length. If the interaction is pure London dispersion force C equals A_{123} (Hamaker constant).

In the following equation (51) is transformed and its minimum is found. For simplification and without losing generality the energy functional is scaled in order to keep the contact line *mathematically* constant. As a circular footprint is assumed the droplet is rotationally symmetric. Then all parameters scale with the droplet volume which is a function of the radius R.

[e] The calculations in this chapter were developed in cooperation with Stefan Karpitschka.

$$\rho = r / R \tag{53}$$

$$\zeta = h / R \tag{54}$$

$$V = 2\pi R^3 \int_0^1 \rho\zeta(\rho) d\rho \rightarrow R = \left(\frac{V}{2\pi \int_0^1 \rho\zeta(\rho) d\rho} \right)^{1/3} \tag{55}$$

Furthermore the macroscopic contact angle θ_∞ is introduced and further substitutions for the interaction parameter, the cut-off length and the energy are made

$$\alpha = \cos\theta_\infty = \frac{\gamma_{13} - \gamma_{23}}{\gamma_{12}} \tag{56}$$

$$\beta = \frac{C}{\gamma_{12}} \frac{1}{12\pi} \left(\frac{2\pi}{V} \right)^{2/3} = D \frac{1}{12\pi} \left(\frac{2\pi}{V} \right)^{2/3} \tag{57}$$

$$\lambda = z_0 / R \tag{58}$$

$$\varepsilon = \frac{E(r)}{2\pi\gamma_{12}} \left(\frac{2\pi}{V} \right)^{2/3} \tag{59}$$

which leads to the energy functional

$$\varepsilon(\zeta) = \underbrace{\left(\int_0^1 \rho\zeta(\rho) d\rho \right)^{-2/3}}_{\text{Volume}} \left(\underbrace{\int_0^1 \rho \sqrt{1 + \left(\frac{\partial\zeta(\rho)}{\partial\rho} \right)^2} d\rho}_{\text{Surface}} + \underbrace{\frac{\alpha}{2}}_{\text{Interface}} \right) - \underbrace{\beta \left(\int_0^1 \frac{\rho}{(\zeta(\rho) + \lambda)^2} d\rho \right)}_{\text{Disjoining Pressure}} . \tag{60}$$

The general structure of the equation remains the same as in equation (51). The second integral still represents the top surface energy, $\alpha/2$ represents the liquid-solid surface energy and the last term results from the disjoining pressure resulting from the Van-der-Waals interaction. The *reduced interaction parameter* $D = C/\gamma_{12}$ in β (equation (57)) is a system immanent parameter that turns out to be the reduced Hamaker constant if the interaction is only due to dispersive forces. D has the unit m² and can be described as a characteristic area. Up to now no assumptions for the profile of the liquid-vapor surface were made. If the shape of the droplet is assumed to be a spherical cap[23] the height profile can be written as

$$\zeta(\rho) = \sqrt{\sin(\theta)^{-2} - \rho^2} - \cot(\theta) . \tag{61}$$

If the microscopic contact angle is replaced with $\cos(\theta) = a$ the contour of the droplet transforms to

$$\zeta(\rho)=\frac{-a+\sqrt{1-(1-a^2)\rho^2}}{\sqrt{1-a^2}}\,. \tag{62}$$

Using this, the first (volume) integral in equation (60) becomes

$$\int_0^1 \rho\zeta(\rho)d\rho=\frac{\sqrt{1-a}(2+a)\pi}{3(1+a)^{3/2}} \tag{63}$$

and the second (surface) integral

$$\int_0^1 \rho\sqrt{1+\left(\frac{\partial\zeta(\rho)}{\partial\rho}\right)^2}\,d\rho=\frac{2\pi}{1+a}\,. \tag{64}$$

The third integral (excess energy) of the system can be written as

$$\int_0^1 \frac{\rho}{(\zeta(\rho)+\lambda)^2}\,d\rho=\frac{\left(a-\sqrt{1-a^2}z_0\right)}{z_0\left(\sqrt{1-a^2}+(1+a)z_0\right)}+Log\left(1+\frac{1-a}{\sqrt{1-a^2}z_0}\right). \tag{65}$$

With these integrals the total energy ε is obtained.

$$\varepsilon(\zeta)=\left(\frac{\sqrt{1-a}(2+a)\pi}{3(1+a)^{3/2}}\right)^{-2/3}\left(\frac{2\pi}{1+a}+\frac{\alpha}{2}\right)- \tag{66}$$
$$-\beta\left(\frac{\left(a-\sqrt{1-a^2}z_0\right)}{z_0\left(\sqrt{1-a^2}+(1+a)z_0\right)}+Log\left(1+\frac{1-a}{\sqrt{1-a^2}z_0}\right)\right)$$

For equilibrium conditions equation (66) is derived and set to zero. This leads to a rather complex relation between the contact angle and the droplet radius for different reduced interaction parameters D.

$$D=\frac{\left(3\left(2-3a+a^3\right)^{1/3}R+3^{2/3}\left((1-a)(2+a)^2\right)^{1/3}\pi^{1/3}z_0\right)^2 z_0(a-\alpha)}{\left(-6\left((1-a)^4(2+a)^2\right)^{1/3}R^2+3\cdot 3^{2/3}\left(-2+a+a^2\right)\pi^{1/3}z_0R-3^{1/3}(2+a)\left(2-3a+a^3\right)^{1/3}\pi^{2/3}z_0{}^2\right)}\cdot \tag{67}$$

$$\cdot\frac{-12\pi\left((1-a)\left(\frac{3}{\pi}\right)^{1/3}R+\left(2-3a+a^3\right)^{1/3}z_0\right)}{3(1-a)^{2/3}(2+a)^{1/3}}$$

This equation links the microscopic contact angle α and the radius for a given reduced interaction constant D which is determined by the system parameters. Unfortunately this equation cannot be transformed to an explicit equation for the microscopic contact angle α as it cannot be inversed.

A plausible approximation for the complex formula for the contact angle (equation. (67)) is

$$D = 6\pi\left(z_0\left(\frac{3-3a}{2\pi + a\pi}\right)^{1/3} + \frac{3}{2}\left(\frac{z_0}{R}\right)^2\right)(a-\alpha)\,. \tag{68}$$

Both equations provide solutions for positive and negative D which correspond to attractive and repulsive interactions. The mathematical results of equation (67) and the validity of the approximation (equation (68)) are shown in Figure 38 in blue and red, respectively. The graphs are divided in a part with linear and logarithmic scaling of the x-axis in order to illustrate the behavior for small and large radii, respectively. The data are calculated for a small cut-off length (top, $z_0 = 0.4$ nm, close packing c.f. Israelachvili[67]) and for a cut-off length that corresponds to the molecular diameter of fullerene molecules (bottom). As the aggregates are assumed to be amorphous the two presented cut-off lengths represent the extrem values for molecules of 1 nm diameter as fullerenes. The real cut-off length will be somewhere between crystallinity (close packing) and maximal molecular distance. It is obvious, that higher cut-off lengths lead to more asymmetric curves for small radii. Moreover, the interaction parameter necessary to obtain a similar effect increases with z_0.

The approximation works perfectly well for $z_0 = 0.4$ nm. For bigger cut-off lengths the region of small radii and small disjoining pressures is not perfectly covered as a non-existing unphysical solution is obtained.

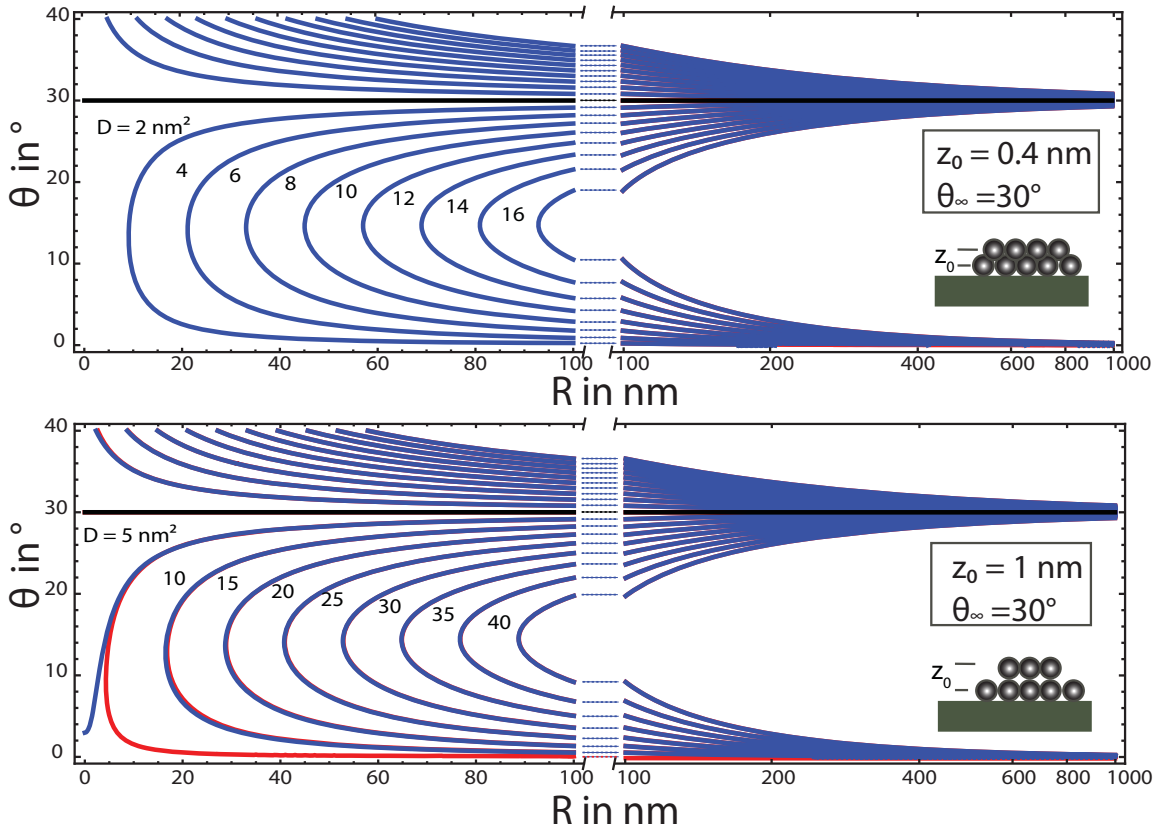

Figure 38: Comparison of exact (blue) and approximate (red) solution for different interaction parameters *D*. The calculations were made for $z_0 = 0.4$ nm (top) and $z_0 = 1$ nm (bottom) for an infinite contact angle of 30°.

5.5.2 Physically Relevant Solutions

The general consequence of attractive or repulsive interactions on the equilibrium shape of sessile drops is sketched in Figure 39. It is obvious that the contact angle changes significantly especially for small radii. For a decreasing radius and a positive or negative interaction constant the contact angle becomes smaller or bigger, respectively.

For positive Hamaker constant a shrinking drop will eventually encounter a critical minimal radius where the slope for the corresponding equipotential line in Figure 38 becomes infinite. Then the drop collapses to a film as indicated in Figure 39. A growing nucleus will first form an adsorbed film that, at a certain size, can jump to a cap shaped droplet. For a given equipotential line above the critical radius R_{crit} two solutions of equation (67) are mathematically possible. The lower one represents a transition to a wetting regime where films are formed and thus the description of a cap-shaped droplet does not apply. Therefore this solution is considered unphysical. The occurrence of a critical radius depends on the cut-off length. For big molecules the lower unphysical branch can be suppressed.

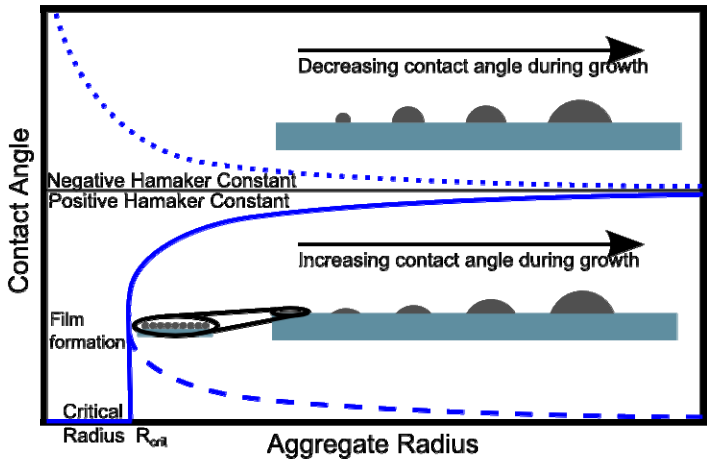

Figure 39: Schematic drawing of the effect of positive or negative Hamaker constants on the contact angle of growing sessile droplets. For negative Hamaker constants (repulsive regime, dotted line) the contact angle decreases for growing droplets. For positive Hamaker constants (attractive regime, solid line) the molecules are first attached as a film to the surface and transform into a droplet at the critical radius R_{crit}. The contact angle of the growing droplet increases.

Although equation (67) provides a solution for repulsive interaction this does not describe a physically stable state. As the surface tension is always positive, the interaction parameter C and the reduced interaction parameter D will always have the same sign. Negative Hamaker constants A_{123} (and analogously interaction parameters C) are only obtained for the given system if the individual Hamaker constant A_{11} is intermediate between A_{22} and A_{33}[87]. This contradicts the condition for partial wetting where A_{33} has to intermediate between A_{11} and A_{22}[67]. Hence a sessile droplet with repulsive interaction can only be metastable due to further effects like pinning that are not included in the presented stability calculation.

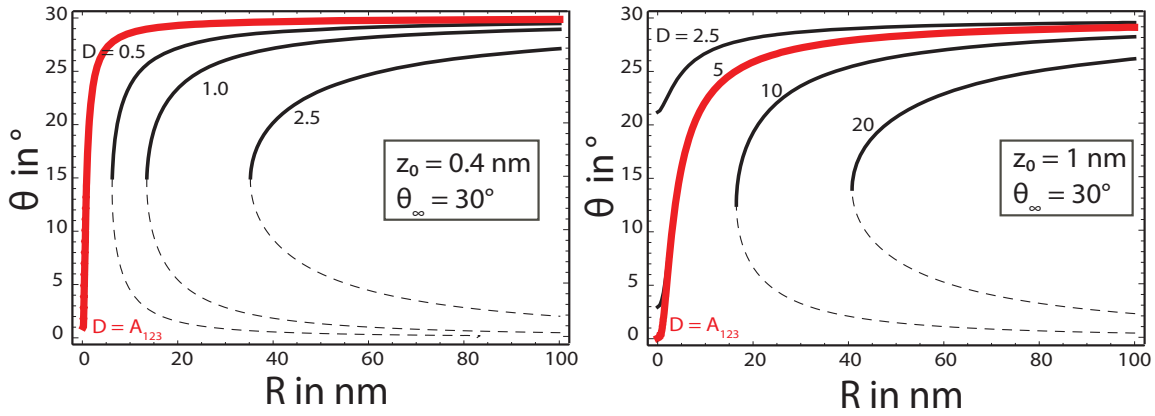

Figure 40: Contact angle as a function of the droplet radius for different reduced interaction parameters *D*. The lines are equidistant. The shown example is calculated for a cut-off length z_0 of 0.4 nm(left) and 1 nm (right) and a macroscopic contact angle of 30°. The physical solutions are shown with solid, the non-physical with dashed lines. The red line shows the solution for pure London dispersion interaction ($D = A_{123}/\gamma_{12}$)) and equally sized molecules.

The relevant choice of appropriate Hamaker constants can be further limited by applying the findings of chapter 5.3. If the molecules are equally sized and the interaction is only caused by London dispersion forces the reduced interaction constant D is determined by

$$D = A_{123}/\gamma_{12} = 12\pi\, z_0^{\,2}(1-\alpha) \tag{69}$$

(cf. Equation (48)). This limits the set of curves to the one shown in red in Figure 40. All unphysical solutions are dotted.

The critical radius depends on the given macroscopic contact angle as seen in the left graph of Figure 41 where different systems with the same strength of attractive interaction ($D = 2$ nm²) but different infinite contact angles are compared. The critical radius where the drop collapses to a film (marked with colored lines) shifts to higher values as the infinite contact angle decreases.

The critical radii for systems of a given reduced interaction parameter D and an infinite contact angle are shown on the right side of Figure 41. For the sake of completeness the radii are given for contact angles up to 90° even though the approximation for the disjoining pressure is only accurate for small contact angles and the results are less reliable for big contact angles. As an example the interaction parameter used in the left graph is indicated shown as a black dashed line. The critical radius is obtained at the intersection with the lines of the given macroscopic contact angle.

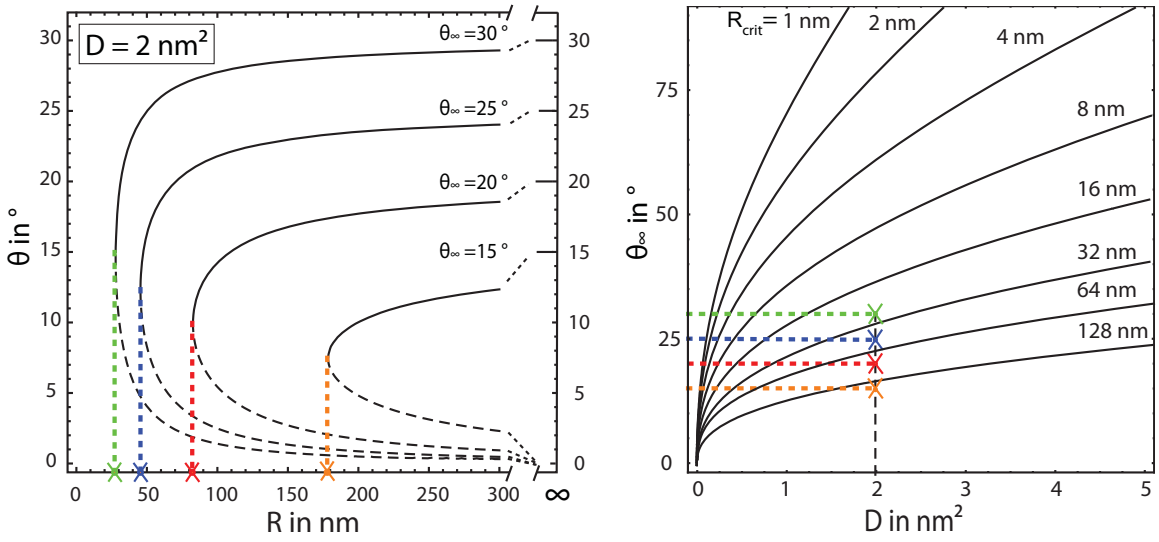

Figure 41 Critical contact angles. Left: Equipotential lines of systems with a Hamaker constant calculated for an interaction parameter $D = 2$ nm² and $z_0 = 0.4$ nm for different infinite contact angles. The critical minimal radii where the transition to wetting films occurs are marked with colored lines. Right: Critical minimal radii of sessile droplets as function of the interaction parameter and macroscopic contact angle. The minimal radius is obtained when the line of the interaction parameter (e.g. $D = 2$ nm², marked with black dashed line) meets the line (colored as in the left graph) for the macroscopic contact angle.

5.5.3 Comparison With Slope Dependent External Energy

The derivation for the size-dependent contact angle due to disjoining pressure was done up to now with an interaction energy that only considered the thickness of the droplet and ignored the contact angle dependent terms that have to be included for a complete derivation according to Dai et al. [68]. For a more exact result the contact angle has to be taken into account. The total energy changes then to

$$E(h) = 2\pi \left(\gamma_{LV} \int_0^R r \sqrt{1 + \left(\frac{\partial h(r)}{\partial r} \right)^2}\, dr + (\gamma_{SL} - \gamma_{SV}) \frac{R^2}{2} + \int_0^R rH(h(r), \underbrace{\left. \frac{\partial h(r)}{\partial r} \right|_{r=R}}_{\text{Contact Angle}}) \, dr \right) \tag{70}$$

and the disjoining pressure is written as

$$H(h, \left. \frac{\partial h(r)}{\partial r} \right|_{r=R}) = -\frac{A_{slv}}{12\pi (h(r) + z_0)^2} \left(1 + \frac{3}{4} \left(\frac{\partial h(r)}{\partial r} \right)^2 \right). \tag{71}$$

The derivation of the energy functional was performed analogously to that already presented in the limit of the spherical cap approximation. The obtained equations are even more complex and it was found that the corrections for small and especially attractive Hamaker interactions are minor. In Figure 42 the influence of the reduced interaction parameter D, respective β (size corrected reduced interaction parameter, cf. equation (57)) on the contact angle is shown for the simplified calculation used in this

thesis (solid) and the complete calculation (dashed). As both curves nearly overlap the used approximation can very well be used for small contact angles.

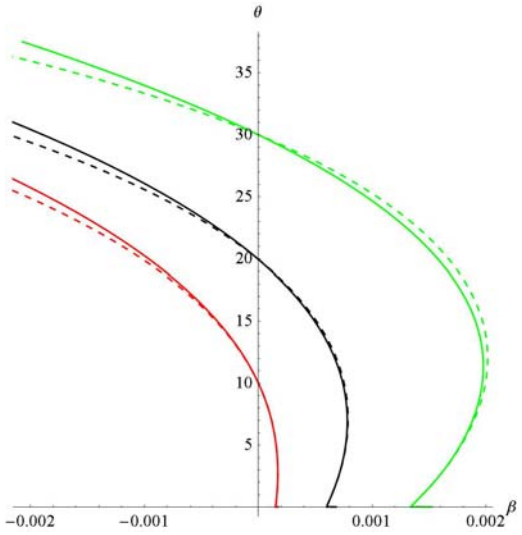

Figure 42: Comparison of Hamaker interaction without (solid) and including (dashed) slope depending terms for a droplet of a radius with ten times the cut-off length.

5.6 Comparison of the Effects of Disjoining Pressure and Line Tension

The result can be compared to the phenomenological approach of the Modified Young's Equation (equation (49)) that transforms in this notation to

$$Cos(\theta) - Cos(\theta_\infty) - \frac{\tau}{\gamma_{12} R} = a - \alpha - \frac{\tau}{\gamma_{12} R} = 0 . \tag{72}$$

The equipotential lines are described as

$$\frac{\tau}{\gamma_{12}} = R(a - \alpha) . \tag{73}$$

Both relations, obtained from disjoining pressure and line tension, are compared in Figure 43 for a macroscopic contact angle of 30°. Two branches are shown for the line tension (dashed line) as positive (top curve) or negative line tensions might be obtained. The general behavior of the two curves resulting from disjoining pressure and negative line tension are similar. For shrinking droplets both concepts predict decreasing contact angles. The obvious difference between the two approaches is that for the disjoining pressure unphysical solutions for attractive interactions occur. This is to some respect comparable to the discussion presented by Milchev[88] even though the radius used in this work is the radius of curvature of the spherical cap. Still the results of both approaches are generally similar. Both have a critical radius in the wetting regime. In the case of line tension the transition to an absorbed film is continuous, in the case of disjoining pressure it is not. For an energetically unfavored three-phase line (positive line tension) the contact angle increases and eventually goes to 180° (complete dewetting) if the droplet gets

smaller. This is the critical radius in the dewetting regime as a shrinking drop will eventually detach from the substrate surface.

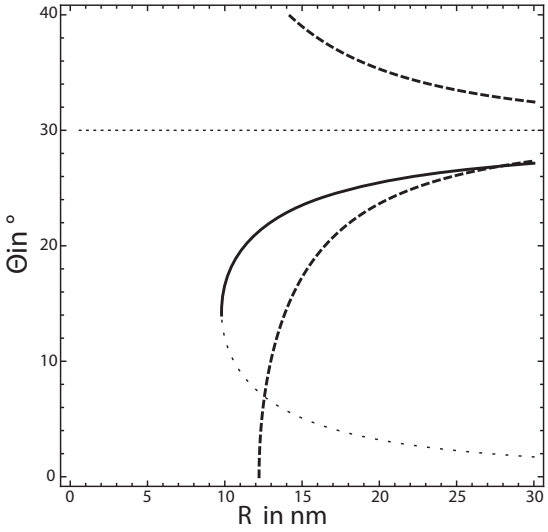

Figure 43: Qualitative comparison of size-dependent contact angle from disjoining pressure (solid) and the phenomenological approach with line tension (dashed) for a macroscopic contact angle of 30°.

Despite the fact that both approaches originate from different fundamental concepts the results are size-dependent contact angles. Both derivations have in common that the molecules at the three-phase line are in a different energetic state. Therefore one could argue that these are two explanations for one effect and should therefore be identified. Doing so and developing in a series in τ up to first order yields

$$\tau = 48\pi A_{123} \frac{R}{z_0\left(3z_0 + 2R\left(\frac{3-3a}{2\pi+\pi a}\right)^{1/3}\right)} \tag{74}$$

which then results in a line tension that depends on R $\tau \rightarrow \tau(R)$. If a pure London interaction is assumed and C is replaced by the Hamaker constant (equation (48)) one finds

$$\tau_{VdW} = -48\pi z_0 \gamma_{12} \frac{(a-1)R}{3z_0 + 2R\left(\frac{3-3a}{2\pi+\pi a}\right)^{1/3}}. \tag{75}$$

This means that the line tension is only depending on the macroscopic contact angle, the cut-off length and the interfacial tension of phase 1 and 2 (vapor-liquid). Hence the line tension effect is independent of the substrate if the macroscopic contact angle is the same.

5.7 Experimental Results

5.7.1 Atomic Force Microscopy

The above predicted deviations of the contact angle of sessile droplets are significant for radii in the nm range. As a model system fullerenes on molecularly smooth and amorphous substrates were investigated. C_{60} fullerenes are ideal molecules as they are rather big, perfectly spherical, homoatomic and do not possess intrinsic dipole moments. Hence the approximation of pure London contribution to the Van-der-Waals interaction is valid. The preparation of fullerene aggregates of nanometer size is rather simple by spin-casting from low-concentrated solutions (c.f. Material and Methods chapter). Furthermore their vapor pressure is very low and they stick to the substrate at ambient conditions after deposition. C_{60} fullerenes partially wet inorganic substrates, and spherical cap shaped droplets (aggregates) form when deposited. The aggregates were investigated with AFM in tapping mode / non-contact mode. The images are scanned line wise and each scan represents an equipotential line. The AFM images of fullerene aggregates show spherical caps with indication of faceting or crystallization only for aggregates of sizes well above 100 nm. Therefore the concept of an amorphous "liquid" or glassy state is applicable. The aggregates are stable against deformation when scanned with tapping mode or non-contact mode AFM. The images are semi-automatically analyzed as described in section 3.1.2. For this analysis a spherical cap approximation is used in agreement with the calculations above.

Figure 44 shows representative AFM images, a 3D representation of a big and a small aggregate as well as a cross-section of a small and a big radius for fullerene aggregates on different substrates. Only the aggregates that meet the filter conditions described in the Methods section (marked in green) are used for analysis. As the distribution of droplets size varies with the position of the sample and the spin-casting conditions usually not the whole range of aggregate sizes is visible in one image. The 3D insets have a width of 400 nm. The images also provide typical height profiles that show cross-sections of droplets of different sizes and do not necessarily show the aggregates from the 3D image. In the 3D representation and in the cross-section the height axis has the same scaling as the lateral axes. The 3D images show therefore the "real" shape.

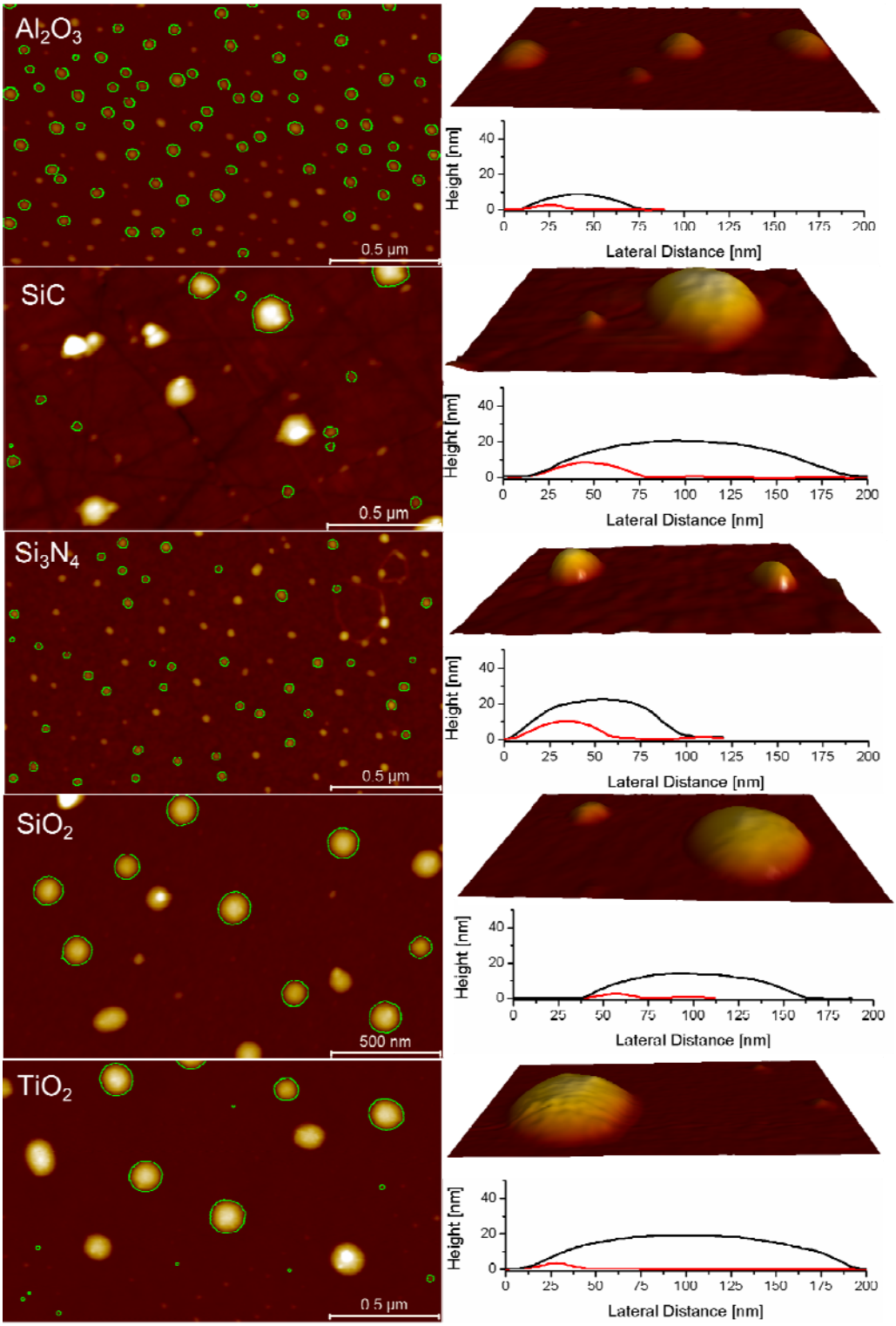

Figure 44: AFM images of C_{60} on different substrates. The images are 2 µm in width and the color scales from -5 nm to 20 nm from black to white which corresponds to 0 nm to 20 nm from brown to white. The aggregates used for the analysis are marked with green. The 3D image shows a magnification with big and small droplets. The graphs show cross-sections of a small and a big droplet. Both, 3D image and cross-section are given in 1:1 scale for lateral and height axis.

The aggregates usually form nice caps. Still some of the droplets are caught in a state were two or more droplets merge or sit on surface defects. These non-spherical droplets are not analyzed. The horizontal stripes in some 3D images are due to the line-wise

scanning process of the AFM or the flattening process and do not represent physical features.

As already stated, the analysis was only done with individual caps that were sufficiently round, large and sitting on a smooth section of the substrate. The contact angle is derived from the diameter of the footprint as function of the measured aggregate volume (cf. Equation (8)) which is more accurate than using only cross-sections (cf. reference Berg, Weber and Riegler[50]).

In general the contact angle decreases for shrinking aggregates and accordingly increases for growing aggregates. The macroscopic contact angle θ_∞ varies with the substrates but is always between 20 and 30 degrees and thus the assumed small angle regime (cf. section 5.5) is valid for all substrates. The obtained data are further analyzed with both approaches, disjoining pressure and line tension on the left and right side of Figure 45, respectively. A large number of data points of contact angles as function of their contact area radius is shown. The left plot (disjoining pressure) shows the obtained data in a contact angle versus radius representation. A further experimental limit is shown as a gray line. It represents the apparent contact angle calculated from height and radius of hypothetical molecularly flat aggregates. This line is a lower limit where the spherical cap approximation is invalid. With the chosen filter parameters the obtained data are well above this limit. The data points are fitted twice. The difference is the cut-off length that is used for the fit. The red line represents the fit for the strength of the disjoining pressure (or characteristic area D) with $z_0 = 1$ nm which corresponds to the molecular size of the fullerenes. This is the approximation where *hard spheres* are assumed and the arrangement is random. Then the distance of the mass centers of molecules on top of each other is the molecular diameter. The green line represents a fit with a cut-off length of $z_0 = 0.4$ nm. This is the distance in z-direction of the mass centers of the fullerene molecules if *close packing* is assumed. The first fit overestimates the cut-off length as not all molecules will lie directly on top of another molecule and the second fit underestimates the distance, as close packing would imply crystallinity which is not observed. The real cut-off length is therefore between the two fits. A representation where the graph is transformed in a straight line is impossible due to the complex structure of equation (67). The numerical results of both fits are given in Table 5. For both methods the fit was performed manually as the unequally distributed sizes overemphasize some regions and nearly ignore others. The reduced interaction parameter D can be transformed in an interaction parameter C (cf. equation (57)) with the surface tension of fullerenes $\gamma_{12} = 0.05$ J/m² [89]. This parameter C can be regarded as an effective Hamaker constant (cf. equation (52)).

Unlike for the disjoining pressure the plots for the line tension (right plot) can be linearized. The obtained graphs are presented as $\cos\theta$ vs. $1/R$ which comes out of the Modified Young's Equation (49). The slope of the obtained data corresponds to the characteristic length τ/γ_{12} and can be transformed to the line tension with the known surface tension of fullerenes.

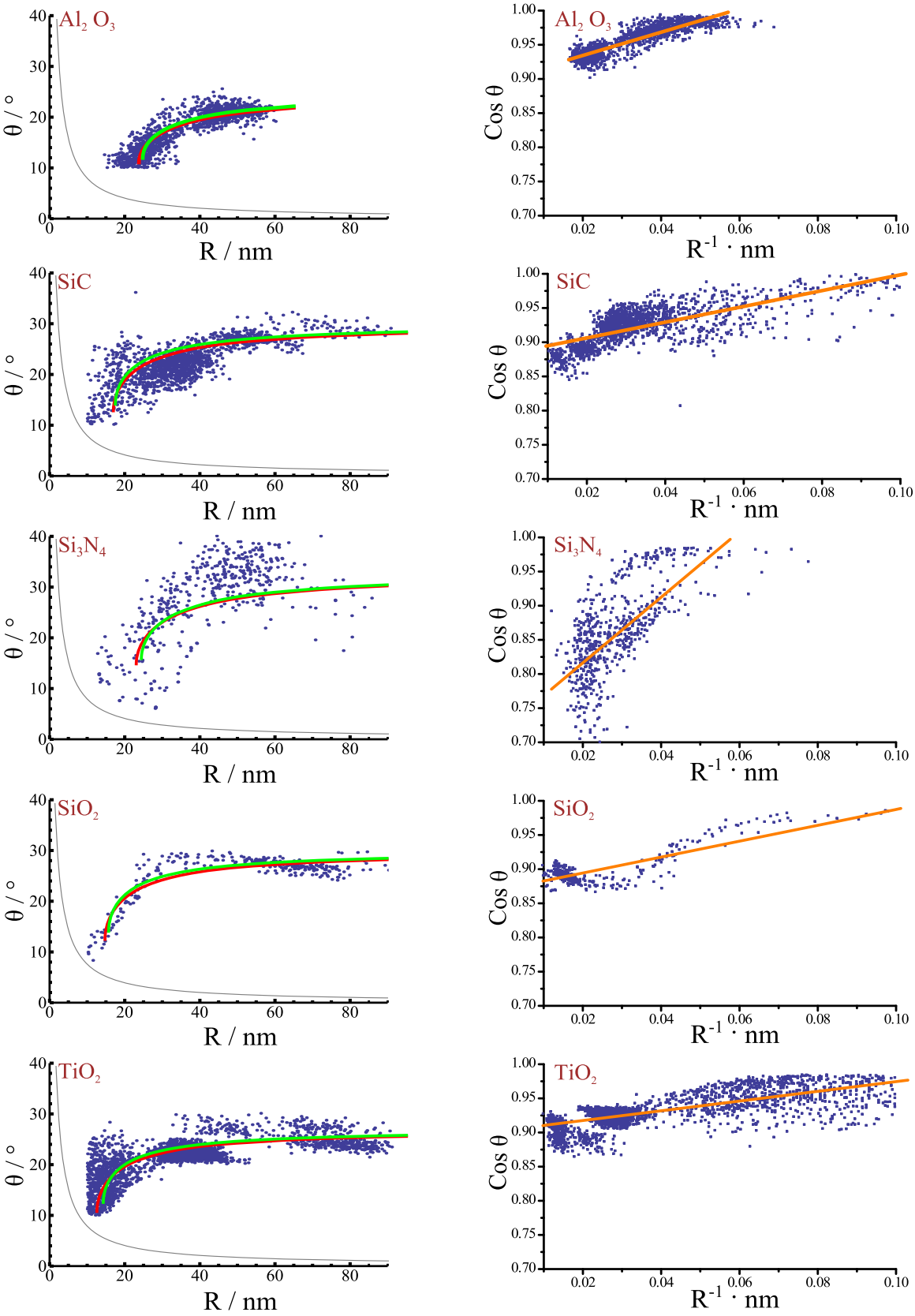

Figure 45: Experimental results obtained with AFM. Left: Contact angles of C_{60} aggregates on different substrates. The data points are fit with a hard sphere approximation (z_0=1 nm) in red and close packing (z_0=0.4 nm) in green. The data range defined by the apparent contact angel of molecularly flat disks of given radius is excluded and shown in gray. Right: Contact angles shown as cosθ vs. curvature 1/R. The orange line is a fit assuming a size independent line tension.

5.7.2 Scanning Electron Microscopy

Complementary to the obtained data with AFM C_{60} aggregates were deposited at standard spin-casting conditions on TEM grids and investigated by scanning electron microscopy. The scans were performed at high vertical tilt angles. Figure 46 shows preliminary results taken at 70°. As the substrate could not be treated with piranha the surface is less well defined as for the AFM images. The contact angle is generally higher as on hydrophilic SiO_2 substrates. The higher roughness of the substrate does not allow for the identification of smaller aggregates.

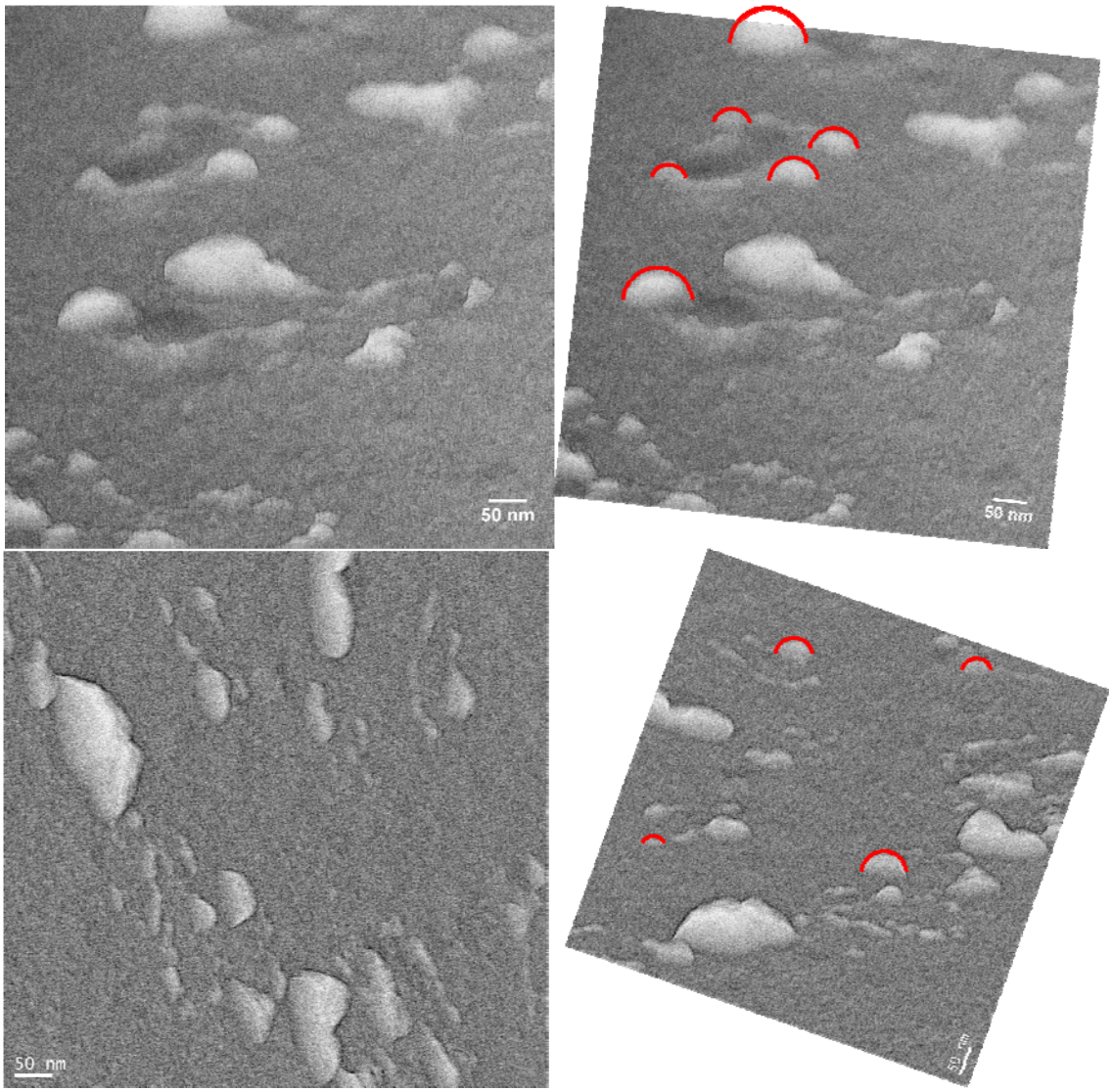

Figure 46: SEM images obtained at high tilt. Left: Raw image, Right: Images with fitted circles.

Spherical cap shaped aggregates could be identified and were fitted with circles. The obtained results of contact angle and radius were analyzed for the Hamaker constant and line tension and are shown in Figure 47 in the same representations as in Figure 45.

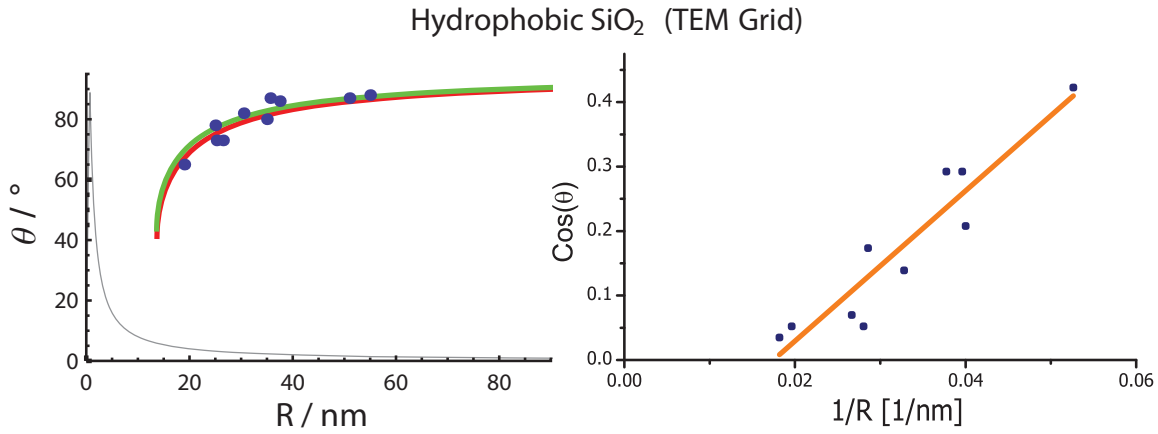

Figure 47: Contact angles obtained from SEM images in Figure 46. The fits of the interaction parameter and line tension are analogous to Figure 45.

5.7.3 Results

The results of the fits for the Hamaker constants are shown in Table 5 and the obtained line tensions are shown in Table 6.

Table 5: Macroscopic contact angle θ_∞, the reduced interaction parameter *D* and the interaction parameter *C* obtained from the left graphs of Figure 45. *D* and *C* are given for the fits assuming hard spheres (red curve) and close packing (green curve).

	θ_∞[°]	D [nm²] (hard sphere)	C [10^{-20} J] (hard sphere)	D [nm^2] (close packing)	C [10^{-20} J] (close packing)
Al_2O_3	25	8.3	41.5	2.9	14.5
SiC	30	10.2	51	3.4	17
Si_3N_4	33	16.0	80	5.8	29
SiO_2	30	9.3	46.5	3.1	15.5
TiO_2	27	6.6	33	2.2	11
SiO_2 (TEM Grid)	95	120	600	42	210

Table 6: Characteristic length τ/γ_{12} and the resulting line tension τ obtained from the graphs on the right side of Figure 45.

	τ/γ_{12} [nm]	τ [10^{-11} J/m]
Al_2O_3	-1.7	-8.5
SiC	-1.2	-6.0
Si_3N_4	-4.8	-24
SiO_2	-1.2	-6.0
TiO_2	-0.7	-3.5
SiO_2 (TEM Grid)	-11.7	-58.5

5.8 Discussion and Outlook

In general the theoretical calculations recover the experimental data of the size-dependent contact angle. Nevertheless some simplifications are used that might turn out to be relevant. As discussed above the limitation to the internal energy and slope independent interactions limit the accuracy to small contact angles. This is already questionable for the results of the electron microscopy on untreated TEM grids. Even though further correction terms would ameliorate the predicted result, the minor amount of experimental data from electron microscopy is the limiting factor for the accuracy. Another shortcoming of the calculation is the assumption of a spherical cap shaped drop. Although consistent with the analysis of the experimental data (where spherical caps are assumed as well) this is not perfectly accurate on a small scale. The proper way to obtain the equilibrium shape would be to (numerically) minimize equation (60) with a free surface. Anyway one would have to fit a sphere to the obtained result in order to compare it with the experimental data.

Even though AFM experiments are crucial to tip effects, no tip deconvolution was performed as the tip radius of 2 nm will only play a significant role for aggregates of equal size which were excluded in the analysis. The accessible region for data points can be estimated geometrically by moving a sphere with the radius of the tip over a spherical cap of given radius. The non-accessible contact angle regions as well as the range of obtained data points are shown in Figure 48 for both used data representations. It is clear that the obtained data ranges do not overlap for 2 nm and would be accessible even with a standard AFM tip of 10 nm radius. Indeed measurements with AFM tips with radii of 10 nm show only minor deviations compared to 2 nm tips.

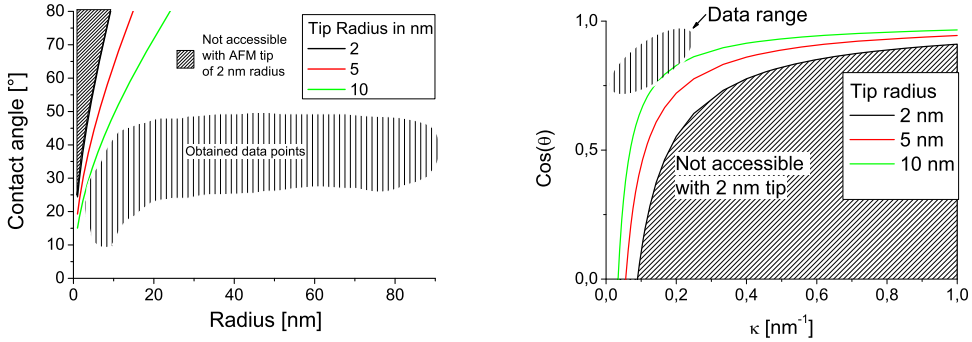

Figure 48: Range of contact angles that cannot be measured with AFM tips of given radius due to geometric hindrance. The experimentally obtained data range is marked with vertical shading.

The conclusion that the measured size effect is not caused by AFM tip artifact is supported by the presented SEM images. Even though they are preliminary and the deduced data is limited the trend of decreasing contact angle with the aggregate size is obvious. Ongoing experiments with more data will provide more exact results.

The interpretation of the size-dependent contact angle as a consequence of a line tension effect yields values in the range of 10^{-11} – 10^{-10} J/m. This is well in the range that was theoretically predicted. Unfortunately a further comparison to literature values is not possible due to the lack of experiments with the investigated system of fullerenes on silicon oxide. Furthermore the reliability of line tension data in the literature is questionable[50]. Interestingly all values are negative. This implies that it is energetically favorable for a molecule to be at the three-phase line. This results in a tendency to maximize the three-phase line.

In the scope of disjoining pressure equation (48) predicts a Hamaker constant that is independent of the actually involved materials but can be calculated from the contact angle for infinitely large droplets and the droplet surface tension. The relation between the reduced Hamaker constant and the cosine of the contact angle θ is predicted to be linear. The actually measured relations for the investigated materials are shown in Figure 49 together with a linear fit (solid line) and the line predicted (dotted).

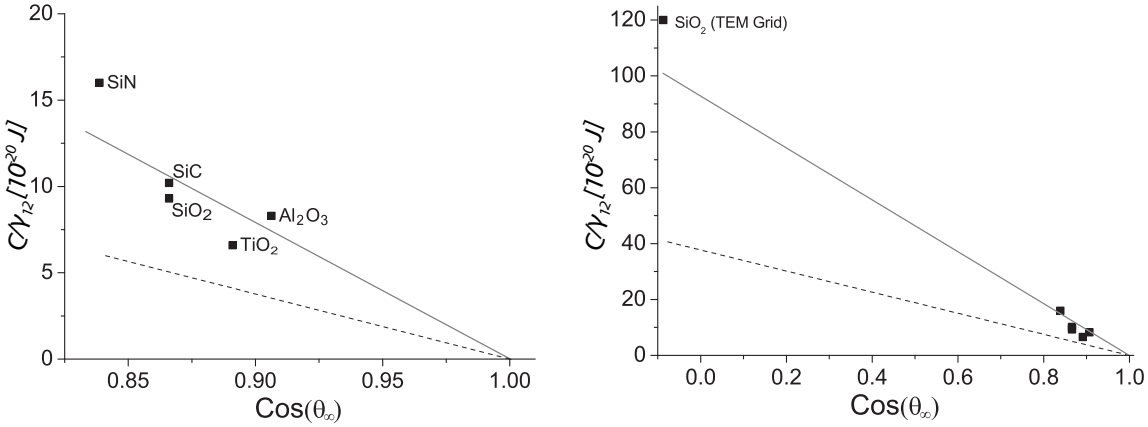

Figure 49: Disjoining pressure for close packing as function of the macroscopic contact angle. The data are obtained from AFM (left) and from AFM and SEM (right). The dotted line represents pure Van-der-Waals interaction with a cut-off length of 1 nm (c.f. equation (48), page 46). The solid line is a linear fit of the experimental data.

The linear fit of the obtained values seems plausible despite their obvious derivations. Still the slope of the fit is roughly doubled compared to the theoretically predicted one. This may have different reasons. First, equation (48) was derived from the assumption of pure London interaction. This means that no permanent dipoles are involved in the interaction. While this holds true for fullerenes (homo-atomic molecules) the substrates consist of atoms with different electronegativities. For the chosen substrates the difference in electronegativity is between 0.7 and 2.0. This results in permanent dipoles in the bonds and the Van-der-Waals force is not of pure London type. Hence the actual interaction is supposed to be stronger than predicted as observed in Figure 49. Still it has to be admitted that no relation between the difference of the experimentally obtained interaction parameter C and the theoretically predicted Hamaker constant A_{123} and the corresponding electronegativity is found. On one hand the ratio is highest for Si_3N_4 (2.6) which has a modest difference of electronegativity (1.2). On the other hand the ratio is smallest for TiO_2 (1.6) which has one of the highest differences in electronegativity (2). Obviously the electronegativity is not the only influence. Further effects that influence the Hamaker constant might be density, shielding effects, conductivity or surface effects.

Besides physical origin the deviations might result from the applied simplifications used for the derivations of both, equation (48) and equation (67). The first was derived from formulas that assume a constant and size independent contact angle. As shown by plenty experimental data this is not true for small aggregates. Hence the validity of the used formulae is questionable. The latter equation was derived without contributions from the contact angle to the internal excess energy and lacks completely the external excess energy. Both approximations are correct for small contact angles but might have a certain influence. Furthermore all equations were derived in the scope of spherical cap shaped droplets. Even though close to reality, this again is an approximation with some influence. Finally it has to be admitted that both, disjoining pressure and line tension were treated exclusively. Still both effects have distinct physical origin and can very well happen at the same time. Unfortunately the accuracy of the data does not allow distinguishing between the two effects. But if the effect of the line tension was comparable to the one of the disjoining pressure the experimental fit in Figure 49 would rather perfectly match the theoretical prediction.

It was shown that size-dependent contact angles can be explained as a consequence of both concepts, disjoining pressure and line tension. No a priori physical argument or experimental result so far favors either concept. However, one important difference in the interpretations of size-dependent contact angles is the stability of molecularly thin films. If the contact angle decreases with the size of the drop, the film thickness eventually becomes equal to the molecule size. Whereas the influence of the disjoining pressure stops then (assuming incompressible molecules), the line tension becomes even more important. For this configuration the maximal surface for a given volume is reached. Anyway the negative line tension favors more three-phase line which drives the molecules apart and disintegrates the droplet. This might be competed by additional stiffnesses or a Tolman length as discussed for equation (50). But as already stated these values are hardly obtainable experimentally. Still one has to admit that the validity of the whole line tension concept which was derived for continuum is rather questionable when applied to individual molecules.

To answer the questions raised above future experiments should include systematic studies of other molecules that will have:

1.) different sizes which results in a different cut-off lengths and

2.) different surface tensions of the liquid-vapor interface.

These molecules should be partially wetting on planar surfaces. Further results might help to segregate the two effects as the cut-off length only influences the disjoining pressure effect whereas the surface tension influences both effects.

6 Nucleation at structured substrates

6.1 Summary

In this chapter purely geometric surface modifications that induce nucleation are analyzed. The technical details to obtain these modifications by indentation or scratching of flat surfaces with AFM are described. The technique to find the patterned area after aggressive chemical cleaning and deposition of C_{60} fullerenes is provided. The results are analyzed thoroughly and discussed with respect to its influence on nucleation. It is found that the patterning works best if the distance of the surface features is chosen close to the average distance of the aggregates on flat substrates. This "natural" distance can be chosen by the spin-casting conditions. Together with the findings of chapter 4 the provided technique in this chapter allows for the production of aggregate arrays of freely selectable dimensions.

6.2 Introduction

The typical process for solidification is nucleation and growth[1–3]. The quintessential property for this process is the nucleation barrier that has to be overcome in order to obtain a stable nucleus[90]. This barrier is dramatically influenced if the nucleation is heterogeneous and a wetting interface is involved. Usually this is employed to decrease the nucleation barrier[91–93] in order to obtain more or easier the desired product. Alternatively the nucleation barrier might be decreased in order to obtain either single crystals[94–96]or to inhibit phase changes at all[97,98]. A third route to manipulate nucleation is to limit its spatial occurrence to well-defined positions in order to end up with an array of selectable dimensions. While heterogeneous nucleation is rather unspecific in terms of the local arrangement on the surface it is possible to use inhomogeneous surfaces to direct the nucleation. The necessary differences in physical properties might stem from e.g. chemistry or topography. On one hand the efficiency of the specific surface features can be investigated[99]. Then the bare surface has to be compared with the surface after precipitation. As the involved features are on a nanometer scale this might be the crucial

part in the experiment. On the other hand a surface modification that is known to efficiently alter the nucleation barrier can be used to localize the nucleation.

In this chapter a technical approach is presented that allows for the preparation of topographic features, its detailed investigation, chemical cleaning, the particle deposition under well-known conditions and the investigation of the finally formed aggregates. The cleaning is done by piranha treatment that produces a silicon oxide surface completely covered with -OH end groups. The integral process is therefore the optimal tool to investigate nucleation and growth processes induced by topographic features. It is used to show the optimal conditions for the production of surface aggregates in preselected arrangements. Possible applications are the production of chips where the conductive parts grow at the desired positions instead of etching away material. Due to the application of spin-casting it is cheap, fast and can be scaled to relevant sizes of chip production. Using the previous findings on spin-casting and aggregate stability the impact of surface modifications on a nanometer length scale on nucleation is shown. In contrast to chapter 4 only “large” aggregates are investigated that are shown to nucleate at the solid surface. The optimal conditions for shape and distance of the modification for a most perfect aggregation in a predetermined formation are provided.

6.3 General Aspects of Heterogeneous Nucleation at Structured Surfaces

For certain thermodynamic conditions a system will undergo a phase transition. This transition does not take place in the whole phase instantly but at certain points the natural fluctuations of the parameters will overcome the critical values. Here the new phase starts to grow. As described in section 2.2 the growing nucleus has to be bigger than a certain critical radius in order to be stable against disintegration. The stability of a nucleus is determined by the fact whether a nucleus gains energy if further molecules are attached. This depends amongst other properties on the geometry of the nucleus. If the nucleus forms at a wetting surface the size and the enthalpy of the critical nucleus are reduced. The exact amount of enthalpy reduction depends on the geometry of the involved surface. If the nucleus forms at an indent at a wetting surface the contact area with the favored surface increases whereas the interface to the unfavored third phase is decreased. Therefore the enthalpy that has to be overcome for the formation of a stable nucleus is decreased. Hence the critical concentration at which nucleation starts is lower for structured than for flat surfaces. For increasing concentration as for spin-casting the nucleation process will first happen at the indents as depicted in Figure 50. The depicted concentration gradient is analogous to the discussion about the spin-casting process in chapter 4. In the following discussion the nucleation at the indents will be termed “*primary nucleation*” and the nucleation at a flat surface “*secondary nucleation*” with respect to the temporal occurrence of the processes.

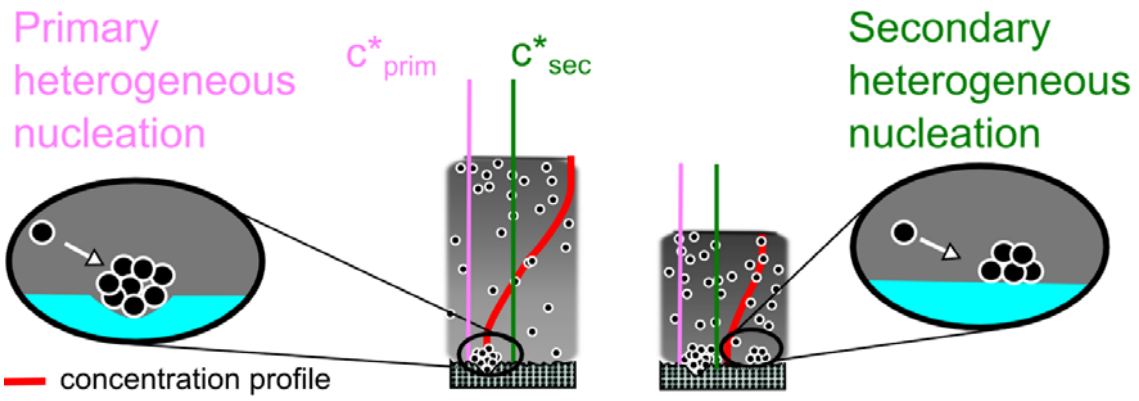

Figure 50: Comparison of the occurrence of primary (at surface features) and secondary (at flat surfaces) heterogeneous nucleation with increasing concentration during spin-casting (c.f. Figure 24 on page 36).

6.4 General Aspects of Surface Manipulation With AFM

SiO_2 substrates are structured on a nanometer scale by indentation or scratching with an AFM tip. The structuring is done with a diamond like carbon (DLC) coated AFM tip (Budget Sensors, Tap300DLC). The hardness of SiO_2 is around 5 Mohs and of diamond-like carbon is 9 Mohs. The tip radius of the used DLC tips is given as 15 nm and the spring constant is 40 N/m. The indentation happens when the tip is pressed on the surface while monitoring the cantilever bending. For the given setup a set point (diode signal) of 1V roughly corresponds to a bending of 45 nm and an applied force of 1.4 µN. This typically results in an indent with 20 nm radius and 1 nm depth. The depth can be changed to some extent by changing the set point between 0 and 4 V. Figure 51 shows an example of a force-distance curve. When the tip is lowered (blue curve) the deflection remains 0 until the tip reaches the surface at -115 nm. When the piezo is further lowered the cantilever is deflected proportionally to the lowering. At a preselected threshold of 1.9 V the approach stops and retracts (red curve). As the substrate was deformed inelastically the two curves do not overlap perfectly as long as the tip is in contact with the surface. This is more clear in the right graph were the data were transformed in a force-separation curve. The separation is the distance between tip and surface and the force is deduced from the cantilever's spring constant.

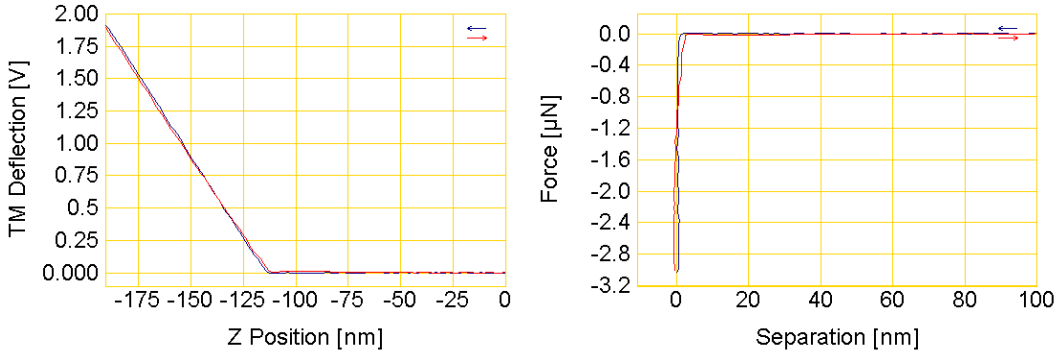

Figure 51: Sample force distance curve for indentation. The left graph shows the deflection of the cantilever vesus the z-position of the piezo. The right graph shows the deduced force put on the surface versus the tip-surface distance. In both graphs the blue curve is the approach, the retract is shown in red.

If the tip is moved while pressed at the surface a scratch is produced. Different types of indents or scratches can be produced by choosing the set-point and the direction of the scratch. The direction is important as rather high forces are exerted via the cantilever on the tip. The AFM software allows for the production of lines and arrays of surface modifications of variable distance. The reproducibility depends on the AFM tips which might change during the surface modification. Eventually the tip will become blunt if used for too long or at too high loads. Depending on the direction relative to the cantilever the exerted force the response of the cantilever may be a) buckling, b) bending or c) torsion as depicted in Figure 52.

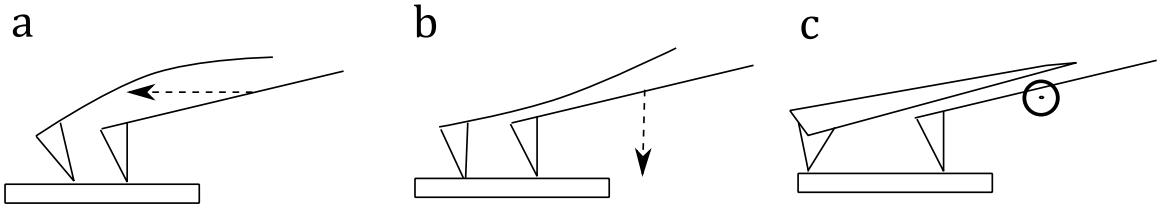

Figure 52: Responses of the cantilever to exerted forces of different directions: a) buckling, b) bending and c) torsion.

The produced modifications are intended to be pure geometric variations of the surface. In order to limit the experiment to the influence of the geometrical contribution, all chemical modifications of the surface have to be excluded. Therefore the substrate is treated with piranha cleaning (peroxysulfuric acid, >80°C, 20 min) 1.) before the high-resolution scanning of the blank surface and 2.) before the deposition. This treatment aggressively removes all organic contamination and ensures that all dangling bonds due to the scratching are saturated with -OH groups and a well-defined surface chemistry is ensured even in the scratches.

After indentation or scratching with the DLC-tip the produced modifications are investigated thoroughly (SSS tip, 2 nm radius and high pixel resolution) before and after the deposition of fullerenes.

The process requires the recovery of the modification both after the removal of the sample from the instrument and after tip change from DLC to SSS. As the modifications are in the range of nm they are invisible with optical methods. If a sample of 1 cm² is

scanned systematically with a 10 µm scanner the chance to find the modification is < 1:1 000 000. Anyway it is possible to retrieve them when it is produced close to macroscopic surface features. Still the recovery is impossible if scanned by AFM with a pixel resolution (scan size / number of pixels per line) that is not detailed enough. For example the pixel resolution to find a 20 nm feature has to be smaller than 10 nm. If the pixel number is too limited (e.g. maximal 512 for Veeco MultiMode III) this results in relatively small scan sizes of 5.12 µm and therefore lots of scans. With more modern instruments the amount of pixels can be chosen higher (e.g. 8192 for JPK NanoWizzard). The tradeoff is that the scan time per image scales quadratically with the pixel number. E.g. an 8192 pixel image scanned at the same resolution and speed as a typical scan (1 Hz at 512 pixels) needs 37:20 hours instead of 8:30 minutes. Still the modifications can be found in reasonable time if the scan parameters and the resolution are adapted reasonably. An example of an AFM scan showing different modifications of the surface is shown in Figure 53. In the presented image the quality is sufficient to retrieve the modifications but for a proper analysis further scans with higher resolution are required.

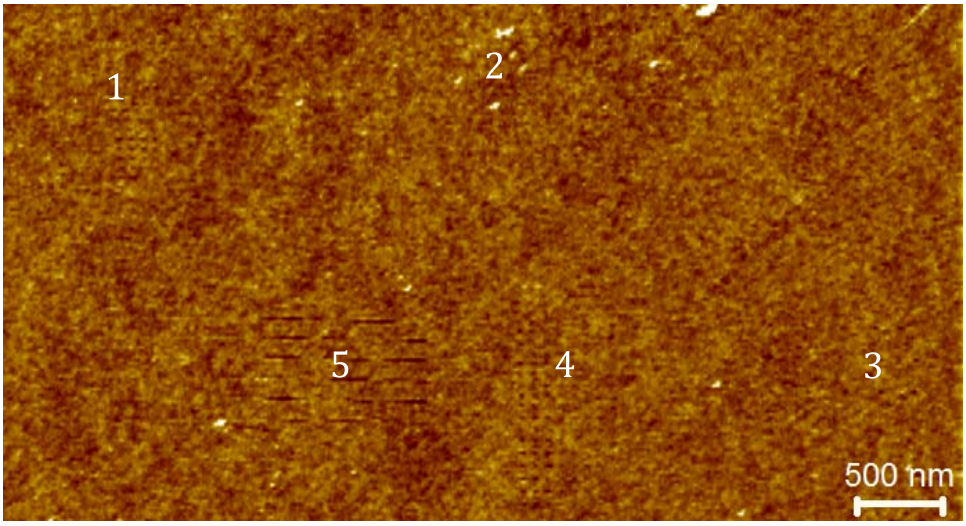

Figure 53: Representative overview scan of an area with different surface modifications (indents 1 - 3, indents with increasing depth 4 and scratches 5). The modifications are barely visible due to the system limitations in resolution of the AFM (512 pixels, Veeco MultiMode III) and are not a result of poor image processing.

6.5 Optimal Nucleation Conditions

6.5.1 General

An example of different rather big modifications as indents and scratches of different angle is shown in Figure 54. This figure comprises an image of the piranha cleaned substrate after modification a), an image after deposition of the C_{60} fullerenes with aggregates b) and the difference in height of both c).

The modifications labeled 1 to 3 correspond to the modification types displayed in Figure 52 labeled a) to c), respectively. The “quality” of the indents obviously depends on the parameters used to produce them. The indents (2) and the scratches done perpendicular to the cantilever (3) are rather uniform. The scratches in the direction of the cantilever (1)

are rather sharp and deep but go along with rather high amounts of debris deposited next to the scratch. This is consequence of the fact that while buckling the force exerted to the surface increases and is released abruptly. In the case of indents and scratches by torsion the cantilever can evade the high load and the force is transmitted more homogeneously.

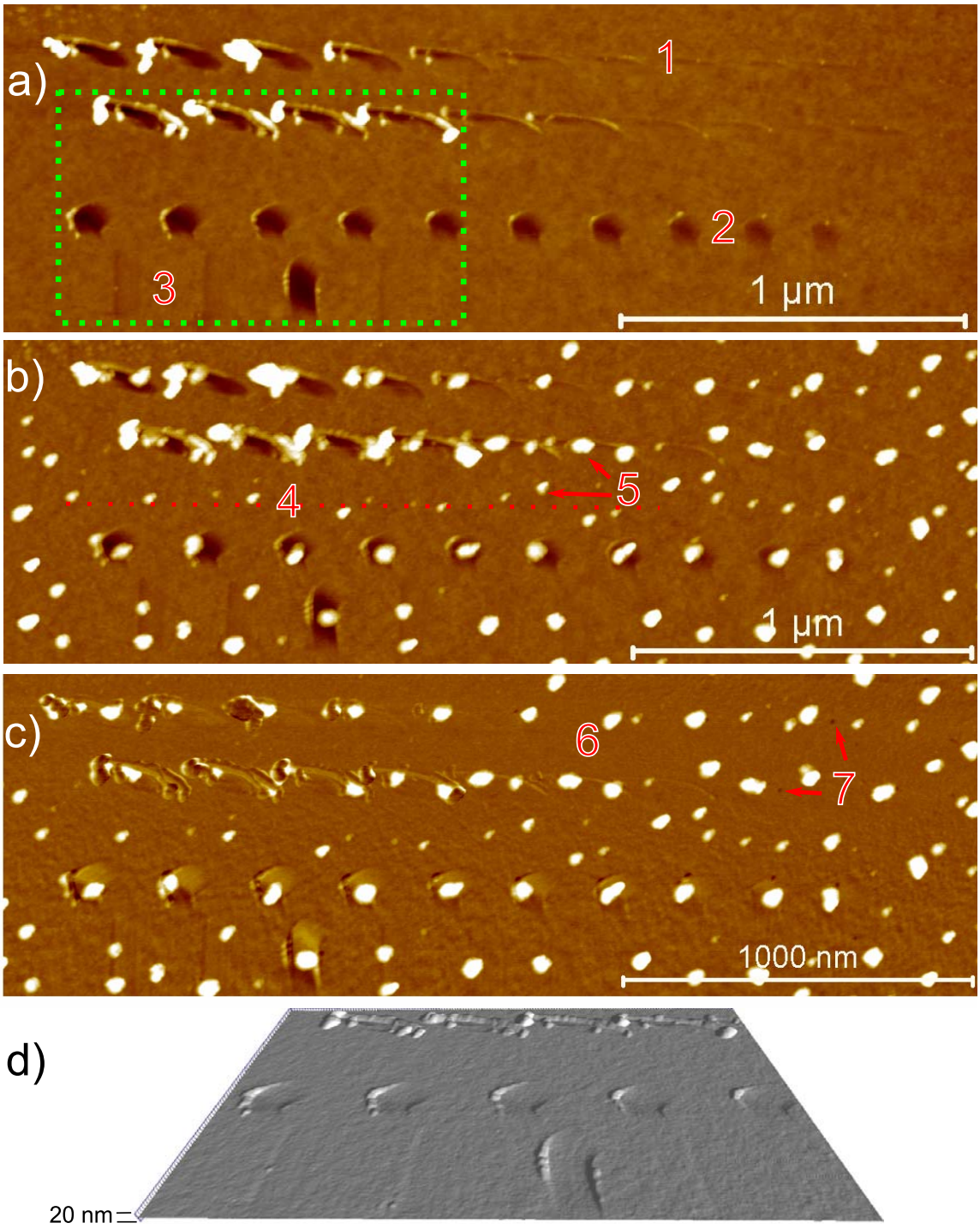

Figure 54: Assembly of different types of scratches (1 and 3) and indents (2) of different depth a) before and b) after deposition of C_{60} molecules. c) Difference in height of both images after alignment. The color scale for all images is 10 nm from black to white. d) 3D representation in 1:1 scale of the green marked are in a).

Figure 54 b) shows that the nucleation indeed prefers the artificial surface modifications (primary nucleation). This is somehow surprising as the depth of the provided indents and

scratches is rather small as shown in the 3D representation of the scan (d). Still lots of aggregates are formed away from artificial surface modifications on plain substrate (secondary nucleation). Interestingly a number of secondary aggregates (4) seem to have a more or less constant distance to the artificial modifications and appear to be aligned (dotted line) and are offset by half a period to the artificial modifications. This is most probably a result of the fact that the scratches favoring primary nucleation are made in a line. Consecutive secondary nucleation tries to maximize the distance to existing aggregates as described in the discussion about the Voronoi analysis of aggregates on unstructured surfaces (cf. section 4.8). Therefore the secondary aggregates between two lines of primary aggregates are favored on a line as well (close packing). Another observation is that the secondary aggregates on the blank substrate but between the surface modifications (4) are significantly smaller than the primary aggregates close by. This can be seen e.g. for the two aggregates labeled (5). Both aggregates are in a similar distance to a primary aggregate at a surface modification. Still the aggregate that was built on a modification is considerably larger than the one formed at the flat surface. These two facts, aggregate size and line-wise aggregation, indicate that the nucleation indeed first happens at the modifications as secondary nucleation would be at random positions if it would happen first.. Assuming that in nucleation and growth the latter is not influenced by the structure of the surface, it is clear that the primary nucleation has to start earlier as it results in bigger aggregates.

Additionally the difference in height of the two images is displayed (Figure 54 c)) which was calculated after carefully aligning both scans. Ideally the image should be monochrome and show only bright spots where material was deposited. This works rather well in the top part of the image (6) where nearly no background is visible. Hence the AFM perfectly recovers the surface before and after cleaning and deposition. This proves that the surface is not altered (besides minor removal of debris (7)) by these two steps! Unfortunately the AFM is not precise respectively stable enough to maintain this accuracy in y-direction. In the lower part of image c) the background is visible again even though the background features are broader than in the initial image. This means that one (or both) images are stretched a bit probably due to piezo effects. Therefore the images do not cancel out perfectly. Still the background is much flatter than the aggregates. This image is used for further analysis as the threshold can be set for the deposited material independent of the surface structure.

In order to identify the properties of the preferred nucleation sites different aspects are investigated as depicted in Figure 55. The top image (a) shows the regions that are deeper than 0.5 nm on the bare substrate marked in blue and the shapes of the aggregates higher than 2 nm in Figure 54 c in red. It is most obvious that all scratches with a depth of 0.5 nm or more resulted in aggregates as all blue labeled indents are in contact with at least one red labeled aggregate. Still lots of aggregates are formed at modifications that are flatter and that can be hardly distinguished from the background (e.g. (1) in a)). At other positions the inherent surface roughness has regions deeper than 0.5 nm that do not result in aggregates. Hence the height is an indication but not a proper measure to predict nucleation.

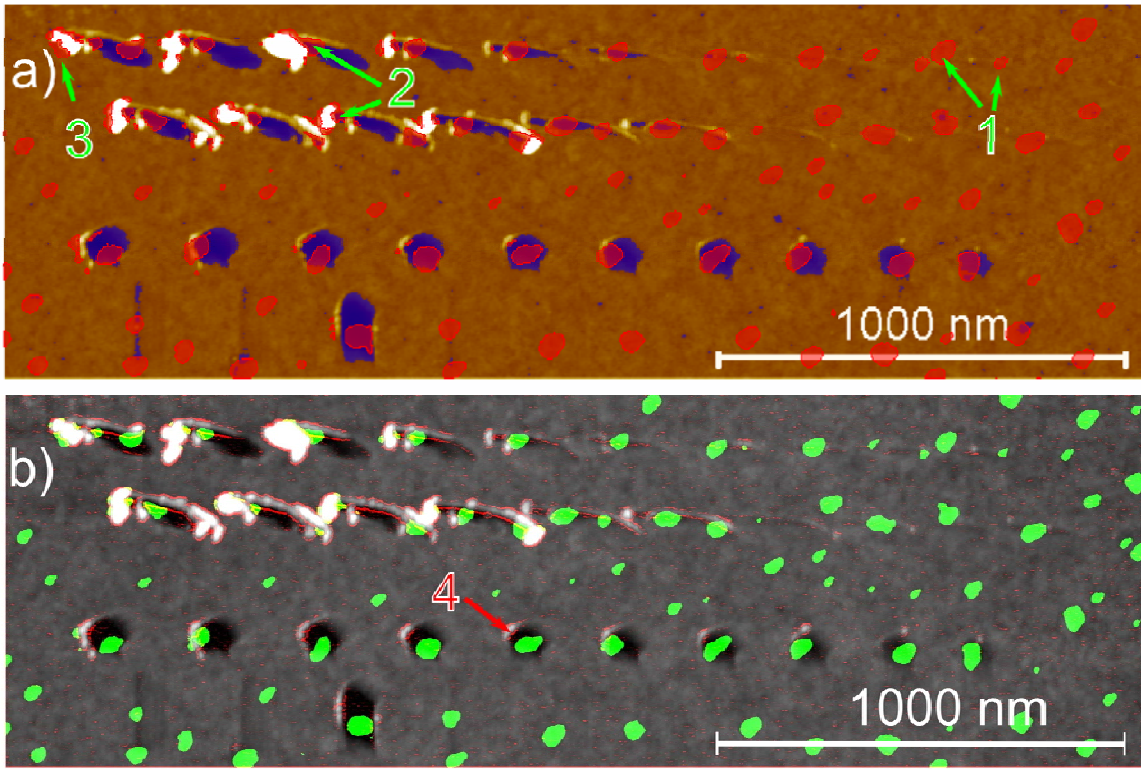

Figure 55: a) Shapes of the modifications (blue if deeper than 0.5 nm) and shapes of the formed aggregates (marked in red if higher than 2 nm in the difference image Figure 54 c) on the initially measured plain substrate. b) Bare scratched substrate in grey scale with shapes of the aggregates in Figure 54 c (green) and the areas with highest concave curvature (red).

If formed at modifications the aggregates often prefer the corners or edges. These are the areas of the highest concave curvature that is marked in red in the lower image of Figure 55. Other areas of high concave curvatures are next to debris from the scratch process where nucleation is induced as well. This works as well inside (2) as outside (3) artificial structures. Often the fullerenes "heal" the cracks or highly curved shapes of the debris and the final combined aggregate is smoother (3). Again if the curvature is high enough it definitely results in an aggregate but lots of aggregates are formed in rather flat areas (green does not touch red in image b) and "ignore" close by regions of high concave curvature (4).

In general it can be concluded from this experiment that two factors play a role if surface modifications induce primary nucleation:

1.) shape (depth and curvature) and

2.) distance.

Both parameters have to be optimized if the aggregation should be limited to the modified spots (primary nucleation). The modification has to be big enough to be efficient and small enough to nucleate only once. The distance of the modifications has to be chosen to match the spin-casting conditions (or vice versa). This will be analyzed in the following images. A single silicon wafer with artificial SiO_2 surface layer was scratched and indented with different depths and distances. Then the sample is piranha

cleaned and spin-casted with a 10^{-5} M C_{60} in toluene solution at 3000 rpm. The images are therefore comparable to each other.

6.5.2 Influence of the Curvature on Nucleation

The influence of the principle curvature can be studied best with long scratches. This is due to the fact that a scratch provides two different curvatures. In the center the surface is only curved in one dimension whereas the ends are curved in two dimensions. The curvature is calculated as

$$H = \frac{1}{2}\left(\frac{1}{R_1} + \frac{1}{R_2}\right). \tag{76}$$

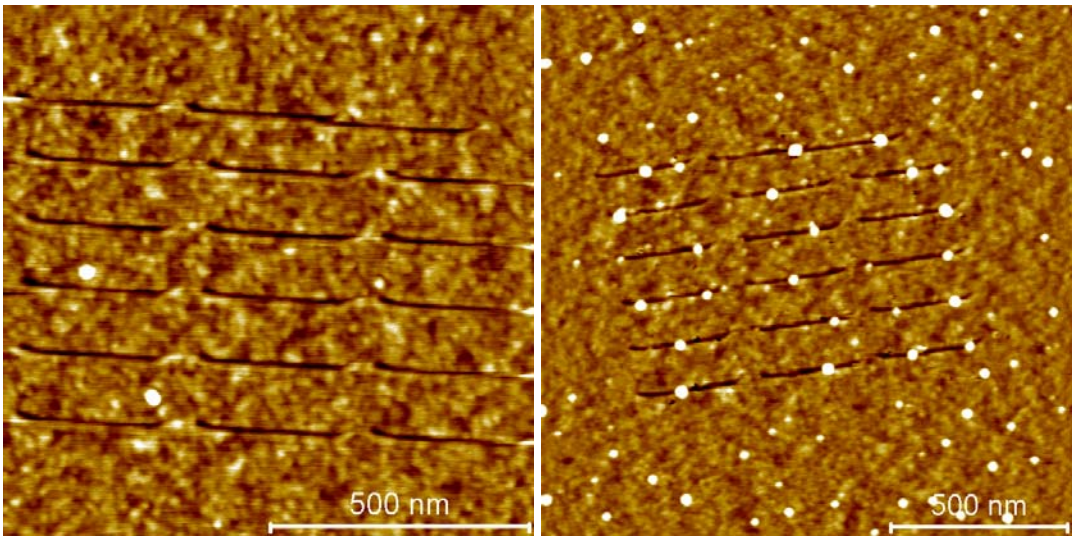

Figure 56: Array of 280 nm long scratches before (left) and after (right) deposition of C_{60}.

As shown in Figure 56 scratches work as nucleation centers. All aggregates in the array region are indeed primary aggregates as they are in direct contact with the provided scratches. But nucleation happens all over the scratch, the exact nucleation position in the scratch cannot be predicted. If the average profiles of both, parallel and perpendicular, profiles are circular fitted one obtains 131 nm and 12 nm radii, respectively. The curvature at the end of the scratches according to equation (76) is 0.09 nm^{-1}. The major contribution (92 %) of this curvature originates from the principal radius perpendicular to the scratch and the additional contribution from the curvature along the scratch is only 8 %. This is obviously not enough to offer a sufficiently high gain in energy to limit nucleation to the ends of the scratches.

A test of the influence of the indentation depth is done with an array of 17 lines along which the depth increases in 20 steps from 0 to 1 nm as shown in Figure 57. The left scan was performed before, the right scan after deposition of C_{60} fullerenes. It is obvious that the biggest aggregates did not form on the left side where the indents are deepest. Still some precipitation is visible (brighter) in the left region where the indents are deepest.

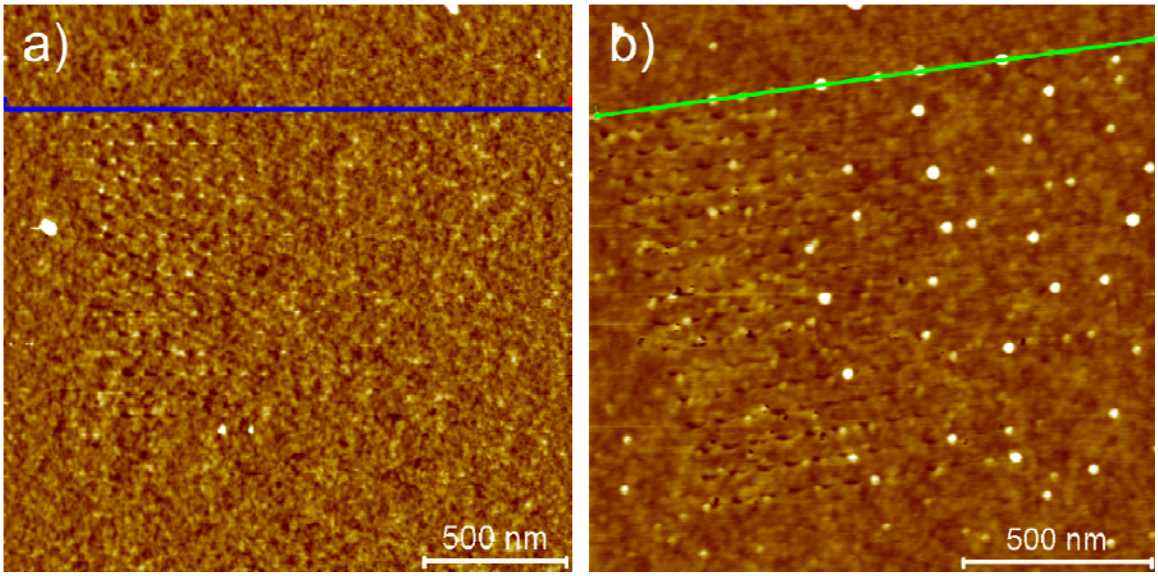

Figure 57: Array of indents with increasing depth before (a) and after (b) fullerene deposition.

The appearance of small aggregates is clear when the top scratched line is compared before and after aggregation (green or blue line, respectively). The two cross-sections are shown in Figure 58 a) displayed in the same colors and it is clear that nucleation and growth happens all over the scratched array. A more easy way to differentiate aggregates from the background is the amplitude image which is shown in Figure 58 b). Here the left side of the array appears rougher than both, the right side and the plane substrate. Hence more small aggregates are present even though not very obvious in the height image. Indeed more material is deposited in the area of deep indents. If the average height in the box marked in red in Figure 58 c) is compared to the line scan of the bare substrate (d) it is obvious that most of the material is deposited in the left 500 nm. Unfortunately this integration cannot be used to identify the most productive indents as the array is distorted due to piezo effects. Therefore positions of the indents in the line scan and the integral overlap only approximately.

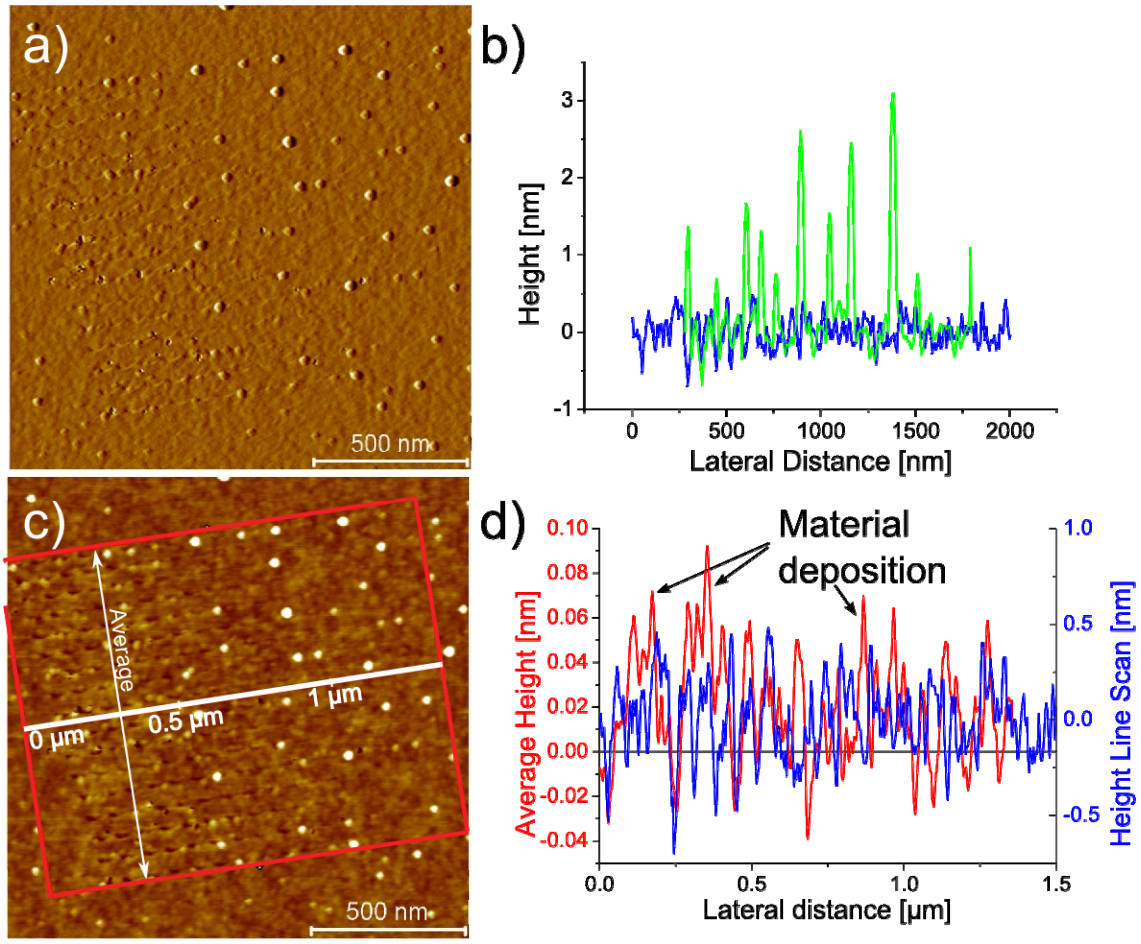

Figure 58: Analysis of the preferred surface modification for nucleation. a) Amplitude image of Figure 57 b) showing even small aggregates. b) Comparison of the cross-section of the same line before (blue) and after (green) C_{60} deposition. c) The area in the red box was averaged line-wise perpendicular to the bold center line. d) The graph shows the line scan (blue) of the pure substrate as indicated in Figure 57a and in red the average height obtained in c). High positive values indicate material deposition.

With the purpose of identifying the ideal scratch for nucleation the indents are analyzed individually. As the indents are usually longer than broad the highest curvature is along the y-direction. Figure 59a shows the bare substrate and the vertical line scans for the first indents of each row. All these scans and the resulting mean curve for the first indent are shown in the inset. The same analysis was performed for the first 10 indents (cf. numbers in a) of the array. The resulting average profiles of the indents are shown in Figure 59 b). The radius of a circle that was fitted in the curves and the corresponding curvatures are given in Figure 59 c). It is obvious that the depth of the scratch and its curvature are linked. The radius of curvature increases from 18 to 80 nm when the depth decreases from 1 to 0.2 nm. Figure 59 d) shows a comparison of the number of aggregates (red) for each indent and the average volume (green) of the resulting aggregate. Obviously the first 7 indents (depth > 0.4 nm and radius of curvature < 35 nm) are most effective. More than half of the indents provides an aggregate, some even more than one. Still the average volume of the resulting aggregate is minor. If the depth decreases and the radius of curvature increases the indents are less effective as nucleation centers as less aggregates are formed. Meanwhile the average volume of the final aggregate increases but the total volume is less than for the deep indents as shown in Figure 58d.

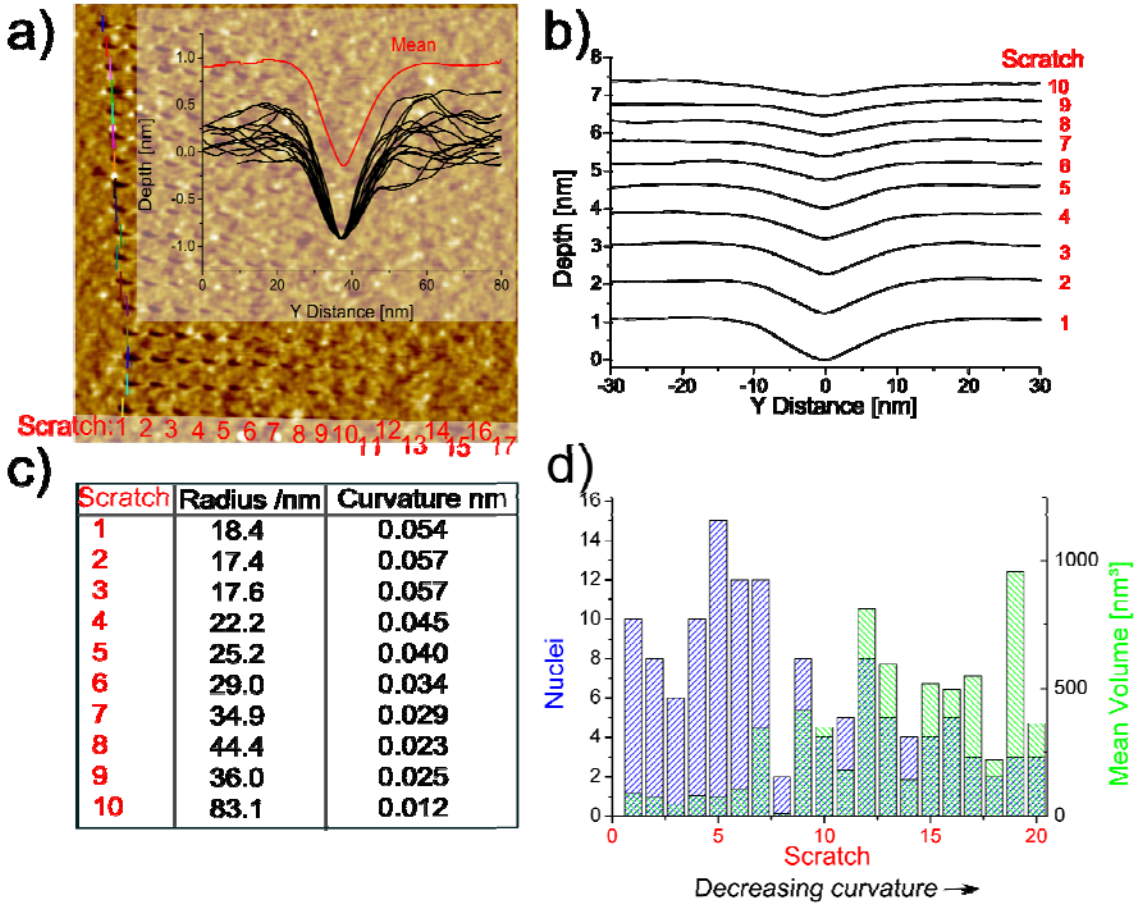

Scratch	Radius /nm	Curvature nm
1	18.4	0.054
2	17.4	0.057
3	17.6	0.057
4	22.2	0.045
5	25.2	0.040
6	29.0	0.034
7	34.9	0.029
8	44.4	0.023
9	36.0	0.025
10	83.1	0.012

Figure 59: Analysis of an array of scratches with decreasing depth. The numbers for the scratches are the same in all four images. a) Bare scratched substrate with the indicated first 17 scratches. The vertical cross-sections of the first scratch are shown in the inset together with the average cross-section in red. b) Mean vertical cross-sections of the first 10 scratches. c) Radii of curvature and curvatures fitted to the curves of b). d) Number of particles (red) in each line (cf. Figure 57 right) with same scratch depth and mean volume (green) of the final aggregates.

If an array of primary aggregates at preselected spots shall be created, the modifications have to be rather small – even on a small scale typical for AFM. Otherwise multiple nucleation centers are created.

6.6 Production of Regular Aggregate Arrays

In the following the influence of the distance of identical indents is analyzed. Figure 60 shows a 6 by 6 array of indents of 0.5 nm depth. As shown in the histogram d) the height is actually a distribution that overlaps with the natural roughness of the substrate. Hence the indents are well in the optimal range found above. The distance between the indents is 140 nm though strong piezo effects distort the rectangular array. The bare substrate after indentation is shown in a). As the indents are not significantly deeper than the background roughness the indents are marked in green in b). Again the influence of the piezo effect is apparent from the distortion of the rectangular array. This is most obvious in the top right corner (first indent made) where the indent is shifted left and overlaps with the next indent. The same array after piranha cleaning and spin-casting of C_{60} aggregates is shown in c).

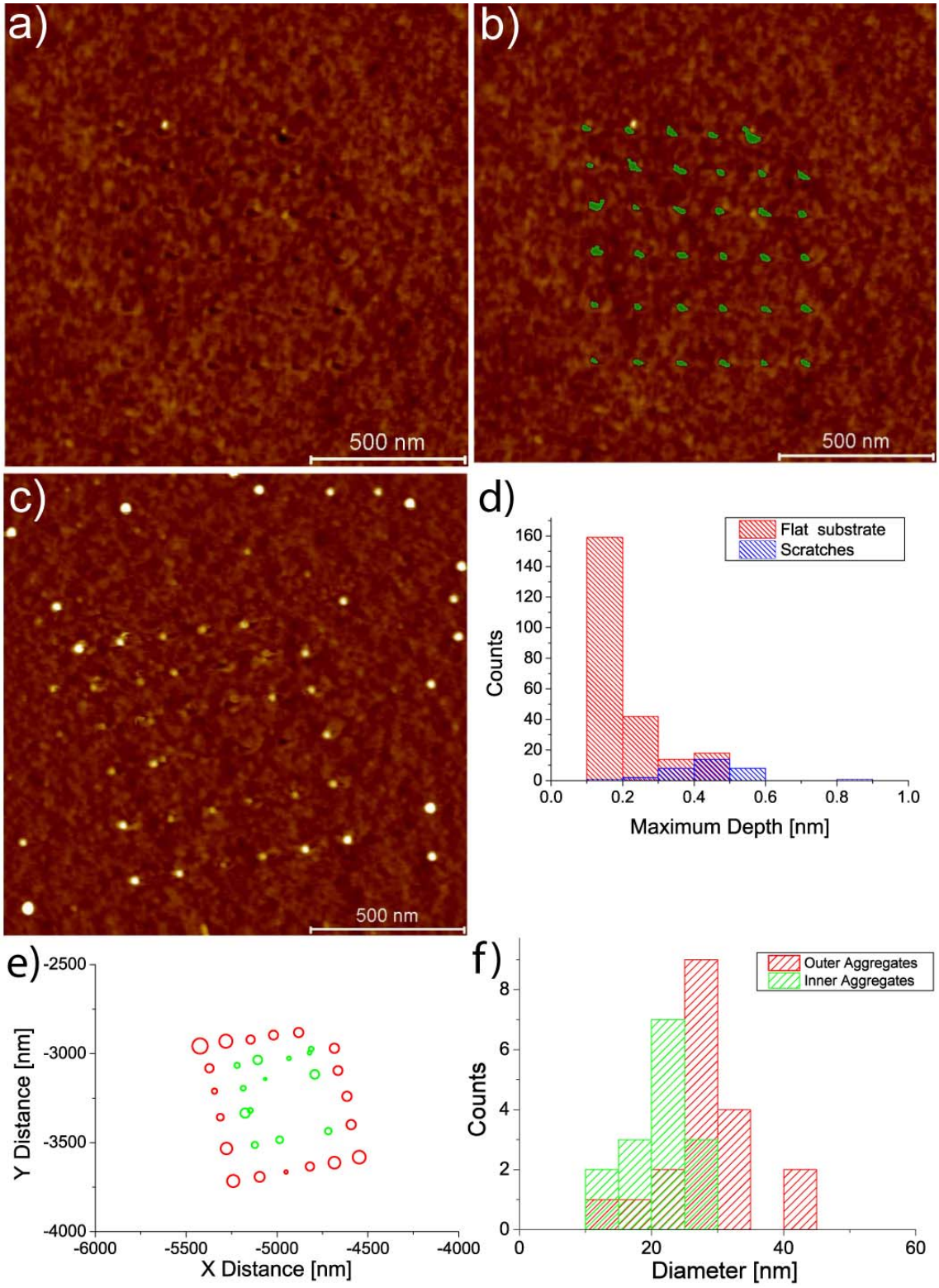

Figure 60: a) Array of 6x6 indents with a depth of 0.5 nm and a distance of 140 nm. b) Same as a) with marked indents. c) Identical location after piranha treatment and C_{60} deposition. d) Comparison of the depth of the natural and artificial dimples. e) Bubble diagram of the aggregate diameter. The inner aggregates are green, the outer aggregates are red. f) Histogram of the diameters of the aggregates formed within the array or at the border.

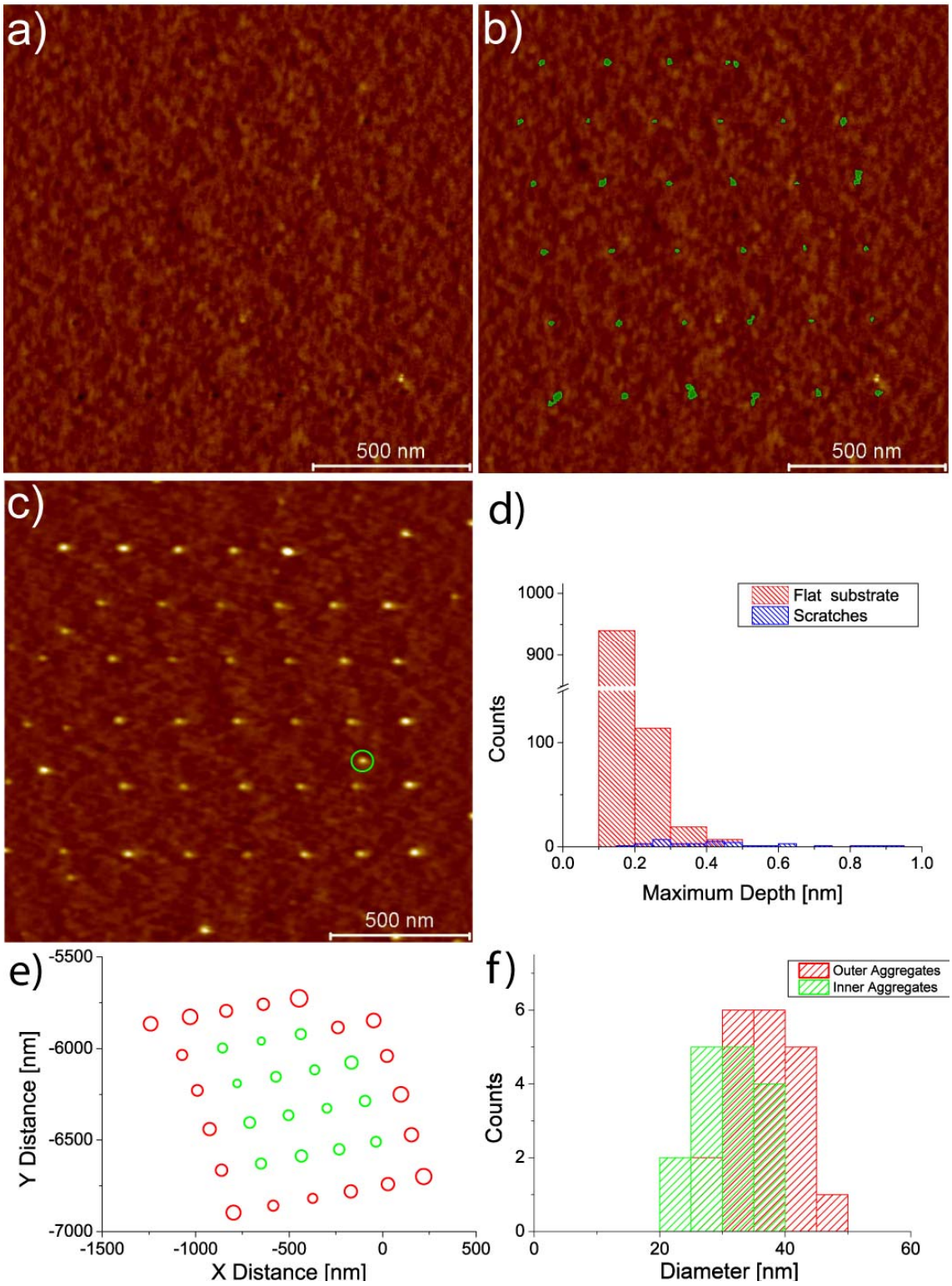

Figure 61: a) Array of 6 by 6 indents with a depth of 0.5 nm and a distance of 240 nm. b) Same as a) with marked indents. c) Identical location after piranha treatment and C_{60} deposition. d) Comparison of the depth of the natural and artificial dimples. e) Bubble diagram of the aggregate diameter. The inner aggregates are green, the outer aggregates are red. f) Histogram of the diameters of the aggregates formed within the array or at the border.

All formed aggregates are primary as they are formed at the provided manipulations in the vicinity of the array. Hence the indents are effective as nucleation centers. Nonetheless it is obvious that the size of the aggregate depends on the fact whether it is

formed within the array or at its exterior. The outer aggregates and in particular the ones at the corners are significantly bigger than the inner aggregates. This is due to the fact that the inner ones are closer together than the "natural" distribution determined by initial concentration and spin-casting conditions (cf. section 4.5.6). The outer aggregates have a bigger collection area (Voronoi cell, cf. analysis in section 4.7) and can therefore collect more molecules per particle. Within the array the supply of molecules is limited and the aggregates compete for it. For an infinitely large array one might still end up with a rather homogeneous size distribution as all inner nucleation spots are in the same surrounding and the border is infinitely far away.

A second experiment with bigger distance of 240 nm between the indentations is performed and the result is shown in Figure 61. As mentioned above the manipulated area was on the same wafer as above. Therefore all experimental parameters as tip properties for indent and measurement, cleaning and spin-casting are identical. The depth of the indents shows a distribution around 0.5 nm again which partly overlaps with the natural roughness. The primary nucleation is very effective and all nucleation sites result in an aggregate. This time one secondary aggregate is formed apart from an artificial modification on bare substrate (green circle in c)). The size distribution within the array is rather homogeneous but again the aggregates at the border are bigger. However the difference in size between inner and outer aggregate is less pronounced. On one hand the comparison between the two arrays of different distances shows that the aggregates in the 140 nm distance array are less homogeneous in size than for 240 nm as shown in Figure 62. The difference is very pronounced and even the error bars barely overlap. For the bigger distance the sizes are far more homogeneous and the outer aggregates are only slightly bigger than the inner ones. This indicates that this system is more close to "equilibrium" as the outer ones that can have far more space for their collection area (Voronoi cell) do not grow much bigger. On the other hand the secondary nucleation at non-modified places (green circle in Figure 61c)) started for 240 nm. Hence the distance of 240 nm might be slightly too large if the nucleation shall be limited to the predefined spots.

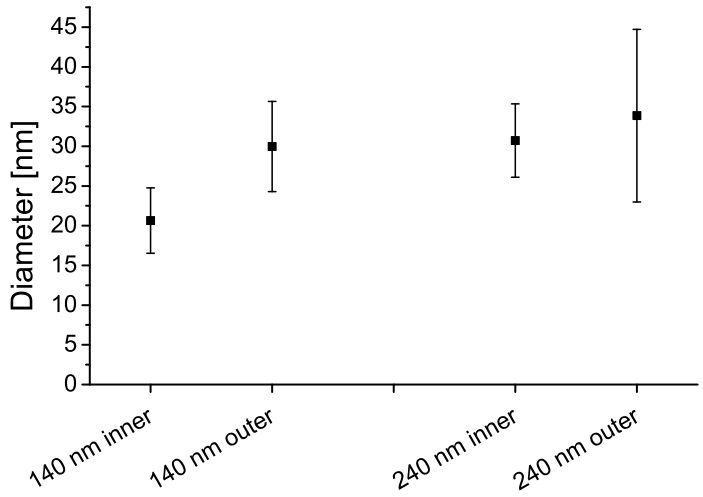

Figure 62: Average diameter of inner and outer aggregates for 140 nm and 240 nm spacing of the indents.

The previous findings indicate that the primary nucleation at predefined places is most efficient if the distance of the modifications is the same as in the unmodified case. Hence the average coverage of the surface has to agree with the predicted value from spin-casting (cf. equation (23)). Then the only limitation that is "forced" to the system is the arrangement of the nuclei which is anyway random for natural surfaces. The structured substrate just picks the one very unlikely but not impossible regular arrangement while the number of nuclei per area remains the same. Then the growth should proceed as in the random case. A comparison of the Voronoi cell areas of both arrays and a bare unscratched substrate is shown in the left image of Figure 63. It is quite obvious that the maximum of the 240 nm array perfectly matches with the bare substrate. The slight tendency to bigger cells might be the reason for the additional aggregate in the array area. The Voronoi cell areas for the 140 nm array are far smaller and barely happen naturally for the given spin-casting conditions. A similar result is obtained for the distribution of the aggregate volumes. For the bigger distance it resembles the one of the natural distribution and has the same preferred size whereas the aggregates for the more narrow indents are much smaller.

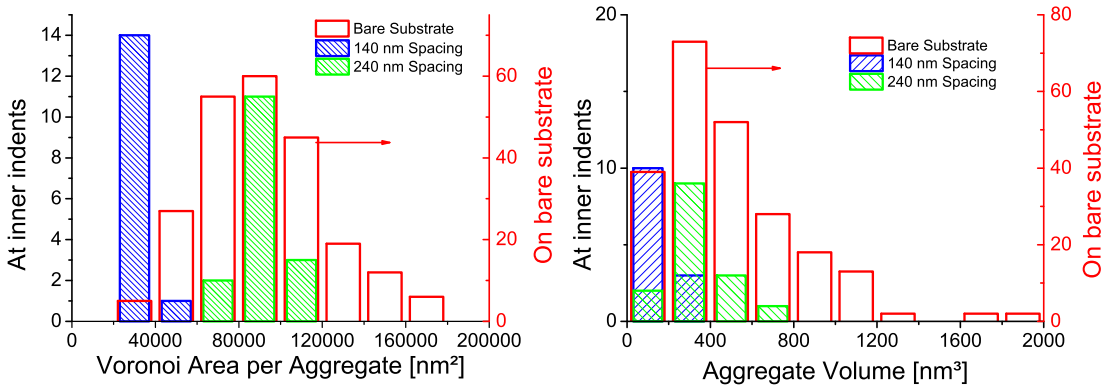

Figure 63: Histograms of the aggregate Voronoi area (left) and aggregate volume (right) for the inner aggregates of arrays with 140 nm (blue) and 240 nm (green) spacing. The red histogram shows the distribution of aggregates on the same substrate as the indents but on unaltered surface.

As assumed before the growth process following the nucleation is barely influenced if the conditions are close to the natural conditions. This is the case for the 240 nm array and consequently the size distribution closely resembles the one of the bare substrate. The limitation to equally sized Voronoi cells limits as well the size distribution as no very big aggregates form. In the case of the 140 nm array the nuclei are narrower distributed. Hence more nuclei compete for the same amount of material and as a result the aggregates are significantly smaller.

6.7 Discussion and Outlook

According to the classical nucleation model a certain energy barrier that is determined by the enthalpy gain from the solid bulk and the enthalpy loss due to surface energies has to be overcome (cf. section 2.2). If two nucleation processes are compared that differ only in the geometrical arrangement the difference in concentration can be calculated from the difference in energy for the flat and the structured surface[1]:

$$\frac{\Delta G}{RT} = V_{nuc} c_{nuc} \ln \frac{c_{crit,\sec}}{c_{crit,prim}}. \tag{77}$$

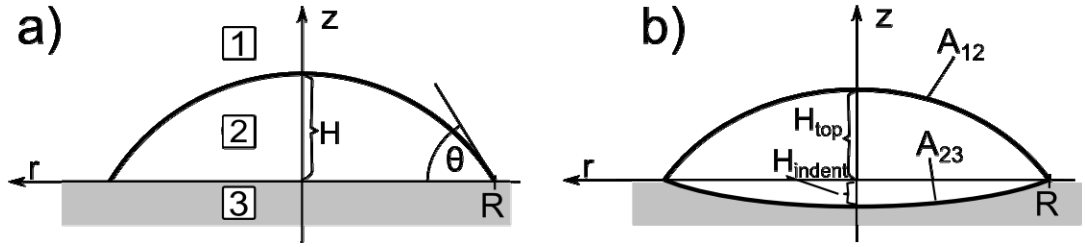

Figure 64: a) Drop on flat solid substrate with height H and contact angle θ. b) Drop with same volume on spherical indent of depth H_{indent}.

If the volume is identical the difference results solely from the interfaces

$$\Delta G = \left(\gamma_{12}\Delta A_{12} + \left(\gamma_{13} - \gamma_{23}\right)\Delta A_{23}\right). \tag{78}$$

Replacing the difference for the surface energies of the bottom area with the contact angle (Young's equation) results in

$$\Delta G = \left(\gamma_{12}\left(\Delta A_{12} + \cos\theta \cdot \Delta A_{23}\right)\right). \tag{79}$$

The volume and the surface area of a spherical cap are

$$V_{cap} = \frac{1}{6}\pi H\left(3R^2 + H^2\right) \tag{80}$$

and

$$A_{cap} = \pi\left(R^2 + H^2\right). \tag{81}$$

The restriction to a constant volume results in a height above the surface H_{top} (cf. Figure 64) that is a function of the indent depth H_{indent}. With geometrical transformations one obtains

$$\mathrm{H_{top}} = \frac{-2\cdot 2^{1/3} R^2 + 2^{2/3} k^2}{2k} \tag{82}$$

with

$$\mathrm{k} = \left(H^3 + 3R^2\left(H - \mathrm{H_{indent}}\right) - H_{indent}^3 + \right. \tag{83}$$
$$\left. + \sqrt{4R^6 + \left(H - \mathrm{H_{indent}}\right)^2\left(3R^2 + H^2 + H\cdot H_{indent} + H_{indent}^2\right)^2}\right)^{1/3}.$$

If inserted into equation (79) one obtains

$$\Delta G = \left(\frac{-\sqrt{3}}{2} H_{indent}^2 + \frac{\left(H^2 - \left(-2^{4/3} R^2 + 2^{2/3} k^2\right)^2\right)}{4k^2}\right)\gamma_{12}\pi \cdot \tag{84}$$

The result is shown in Figure 65 for the two cases of indents of different sizes and a constant depth of 1 nm (left) and a constant ratio H_{indent}/R of 1/20 (right).

For the indents of 20 nm diameter and 1 nm depth with a constant amount of nuclei the difference in enthalpy is 0.4 %. This is 16 % in concentration according to equation (77). As the concentration increases dramatically versus the end of the process this does not represent 16 % of the spin-casting time. In fact the simulation of the spin-casting process shows that this concentration difference is passed within 15 ms (cf. discussion on page 41).

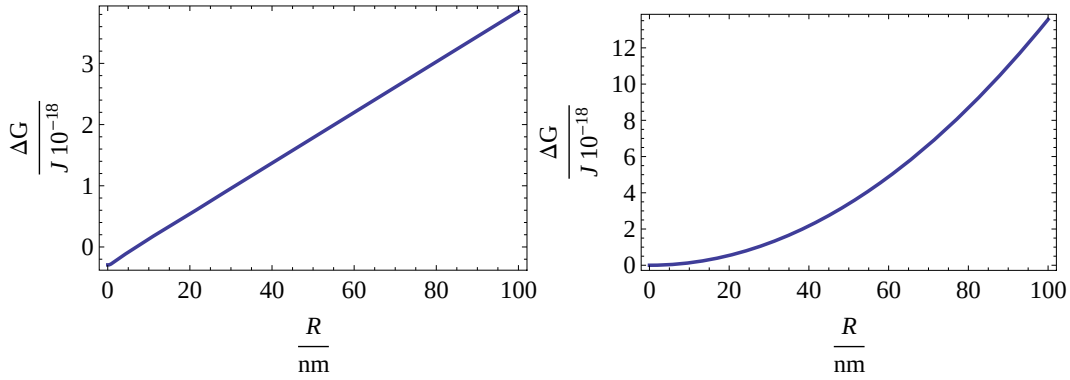

Figure 65: Gain in enthalpy versus indent radius for nucleation at an indent of constant depth of 1 nm (left) and 1/20 *R*. The surface tension γ_{12} is 0.05 J/m² and the contact angle is 30° (fullerenes on SiO_2).

According to equation (43, page 42) a fullerene with a diffusion coefficient of 91µm²/s can diffuse 1.67 µm in this time. Thus the nucleation at surface features is efficient and basically exclusive for the presented conditions if the distance of the features is less than 1.18 µm. This agrees very well with the experimental findings that a chosen structure can only be imposed to a system in a certain concentration regime. If the concentration is reduced the system immanent Voronoi cell area is increased.

The analysis of the aggregation at surface features is limited to the assumption that all aggregates nucleate at the interface. This seems to contradict the findings of chapter 4 but is in fact a result of the fact that the AFM images for this chapter were taken with a Veeco MultiMode IV which is limited in resolution. For example for the scan of the aggregates on the flat substrate the pixel resolution was typically 5 nm per pixel. Therefore the small aggregates presented in the analysis of chapter 4 are not visible respectively are not analyzed as they consist of only very few pixels. Therefore they are not appearing in the size distribution shown on the right side of Figure 63.

In contrast to the analysis in chapter 5.7 where enormous amounts of data were analyzed automatically the presented data in this chapter are rather limited. This is a general problem of microscopic experiment: a limited field of view is analyzed and considered to be general. But the presented experiment was repeated several times with similar results. In general the statistics of the aggregate size could be improved in future experiments by using larger arrays of scratches.

In general the presented technique for the production of well-ordered aggregates can be used for large scales. The most important limitation of the presented experiment is the time needed for the production of the indents or scratches. If it should be used for large scales multiple scratches should be done at the same time. For example a diamond-like carbon coated template can be used as a plunger. Alternatively the modifications could be produced via laser or ionic beam ablation. Both methods have the advantage that no piezo effects are involved. If the produced array is really rectangular with identical distances the distribution of size and Voronoi cell area should be narrower than in Figure 63. In order to inhibit nucleation it is probably best to use a density of manipulations slightly below the system inherent one. The consequence would be that the growing nuclei at the artificial nucleation centers “starve” a bit but completely consume the available molecules before secondary nucleation starts. Still this “overfeeding” with nucleation centers must be minor as a too high density will result in incomplete nucleation at the provided centers.

References

1. Mersmann, A. *Crystallization Technology Handbook*. (CRC Press: 2001).

2. Kashchiev, D. *Nucleation*. (Butterworth-Heinemann: 2000).

3. Kurz, W. & Fisher, D. J. *Fundamentals of Solidification*. (Trans Tech Publications Ltd: 2005).

4. Markov, I. V. *Crystal Growth for Beginners: Fundamentals of Nucleation, Crystal Growth and Epitaxy*. (World Scientific Pub Co (: 2003).

5. Mullin, J. W. *Crystallization, Fourth Edition*. (Butterworth-Heinemann: 2001).

6. Mader, H. M. *et al.* Experimental simulations of explosive degassing of magma. *, Published online: 03 November 1994; | doi:10.1038/372085a0* **372**, 85–88 (1994).

7. Van Liew, H. D. Simulation of the dynamics of decompression sickness bubbles and the generation of new bubbles. *Undersea biomedical research* **18**, 333 (1991).

8. Coffey, T. S. Diet Coke and Mentos: What is really behind this physical reaction? *American Journal of Physics* **76**, 551–557 (2008).

9. Gupta, N. N. D. & Ghosh, S. K. A Report on the Wilson Cloud Chamber and Its Applications in Physics. *Rev. Mod. Phys.* **18**, 225–290 (1946).

10. Kapusta, J. Nucleation rate for black holes. *Physical Review D* **30**, 831–832 (1984).

11. Fujiwara, M., Nagy, Z. K., Chew, J. W. & Braatz, R. D. First-principles and direct design approaches for the control of pharmaceutical crystallization. *Journal of Process Control* **15**, 493–504 (2005).

12. Kim, N. & Thomas, G. Effects of morphology on the mechanical behavior of a dual phase Fe/2Si/0.1C steel. *Metallurgical and Materials Transactions A* **12**, 483–489 (1981).

13. Dunitz, J. D. & Bernstein, J. Disappearing Polymorphs. *Accounts of chemical research* **28**, 193–200

14. Volmer, M. & Weber, A. Keimbildung in übersättigten Gebilden. *Zeitschrift für Physikalische Chemie* **119**, 277–301 (1926).

15. Fladerer, A. & Strey, R. Homogeneous nucleation and droplet growth in supersaturated argon vapor: The cryogenic nucleation pulse chamber. *The Journal of Chemical Physics* **124**, 164710–164710–15 (2006).

16. Kantelhardt, W. China: Die Regenmacher. *Die Zeit* (8:48 Uhr).at <http://www.zeit.de/online/2008/09/china-regen>

17. Bruintjes, R. T. *A Review of Cloud Seeding Experiments to Enhance Precipitation and Some New Prospects*.

18. Volmer, M. *Kinetik der Phasenbildung*. (Verlag von Theodor Steinkopff: 1939).

19. van der Waals, J. D. Molecular theory of a substance composed of two different species. *Zeitschrift für Physikalische Chemie* **5**, 133–173 (1890).

20. McLachlan, A. D. Retarded Dispersion Forces Between Molecules. *Proceedings of the Royal Society of London. Series A. Mathematical and Physical Sciences* **271**, 387 – 401 (1963).

21. Lifshitz, E. M. The Theory of Molecular Attractive Forces Between Solids. *Soviet Phys. JETP* **2**, 94–110 (31-DEC-56).

22. Hamaker, H.C. The London—van der Waals attraction between spherical particles. *Physica* **4**, 1058–1072 (1937).

23. Barchet, W. R. The Validity of the Spherical Cap Approximation in Heterogeneous Nucleation. *Journal of the Atmospheric Sciences* **26**, 112–114 (1969).

24. Rabe, J. STM and AFM Studies on (Bio)molecular Systems: Unravelling the Nanoworld. **285**, 77–102 (2008).

25. Horowitz, F., Yeatman, E., Dawnay, E. & Fardad, A. Real-time optical monitoring of spin coating. *Journal de Physique III* **3**, 5 (1993).

26. Gu, J., Bullwinkel, M. D. & Campbell, G. A. Solvent concentration measurement for spin coating. *Journal of Applied Polymer Science* **57**, 717–725 (1995).

27. Birnie III, D. P., Haas, D. E. & Hernandez, C. M. Laser interferometric calibration for real-time video color interpretation of thin fluid layers during spin coating. *Optics and Lasers in Engineering* **48**, 533–537 (2010).

28. Berg, J. K. *Size-dependent wetting behavior of organic molecules on solid surfaces*. (2011).

29. Karpitschka, S., Weber, C. M. & Riegler, H. Physics of Spin Casting Dilute Solutions. *arXiv:1205.3295* (2012).at <http://arxiv.org/abs/1205.3295>

30. Norrman, K., Ghanbari-Siahkali, A. & Larsen, N. B. 6 Studies of spin-coated polymer films. *Annu. Rep. Prog. Chem., Sect. C: Phys. Chem.* **101**, 174–201 (2005).

31. Al Akhrass, S. *et al.* Viscoelastic Thin Polymer Films under Transient Residual Stresses: Two-Stage Dewetting on Soft Substrates. *Phys. Rev. Lett.* **100**, 178301 (2008).

32. Erber, M. *et al.* Glassy Dynamics and Glass Transition in Thin Polymer Layers of PMMA Deposited on Different Substrates. *Macromolecules* **43**, 7729–7733 (2010).

33. Lai, J. H. An investigation of spin coating of electron resists. *Polymer Engineering & Science* **19**, 1117–1121 (1979).

34. Drury, C. J., Mutsaers, C. M. J., Hart, C. M., Matters, M. & de Leeuw, D. M. Low-cost all-polymer integrated circuits. *Applied Physics Letters* **73**, 108 (1998).

35. Frederik C., K. Fabrication and processing of polymer solar cells: A review of printing and coating techniques. *Solar Energy Materials and Solar Cells* **93**, 394–412 (2009).

36. Kuipers, E. W., Laszlo, C. & Wieldraaijer, W. Deposition of nanocrystals on flat supports by spin-coating. *Catalysis Letters* **17**, 71–79 (1993).

37. Zhao, Y. & Marshall, J. S. Spin coating of a colloidal suspension. *Physics of Fluids* **20**, 043302 (2008).

38. Jiang, P. & McFarland, M. J. Large-Scale Fabrication of Wafer-Size Colloidal Crystals, Macroporous Polymers and Nanocomposites by Spin-Coating. *J. Am. Chem. Soc.* **126**, 13778–13786 (2004).

39. Jung, J.-Y., Kang, Y. T. & Koo, J. Development of a new simulation model of spin coating process and its application to optimize the 450 mm wafer coating process. *International Journal of Heat and Mass Transfer* **53**, 1712–1717 (2010).

40. Yanagisawa, M. Slip effect for thin liquid film on a rotating disk. *Journal of Applied Physics* **61**, 1034–1037 (1987).

41. Melo, F., Joanny, J. F. & Fauve, S. Fingering instability of spinning drops. *Phys. Rev. Lett.* **63**, 1958–1961 (1989).

42. Fraysse, N. & Homsy, G. M. An experimental study of rivulet instabilities in centrifugal spin coating of viscous Newtonian and non-Newtonian fluids. *Physics of Fluids* **6**, 1491 (1994).

43. Holloway, K. E., Habdas, P., Semsarillar, N., Burfitt, K. & de Bruyn, J. R. Spreading and fingering in spin coating. *Phys. Rev. E* **75**, 046308 (2007).

44. Jenekhe, S. A. & Schuldt, S. B. Coating flow of non-Newtonian fluids on a flat rotating disk. *Ind. Eng. Chem. Fund.* **23**, 432–436 (1984).

45. Britten, J. A. & Thomas, I. M. Non□Newtonian flow effects during spin coating large□area optical coatings with colloidal suspensions. *Journal of Applied Physics* **71**, 972–979 (1992).

46. Bornside, D. E. *et al.* The effects of gas phase convection on mass transfer in spin coating. *Journal of Applied Physics* **73**, 585–600 (1993).

47. de Gennes, P.-G. Solvent evaporation of spin cast films: crust effects. *arXiv:cond-mat/0111117* (2001).doi:10.1140/epje/i200101169

48. Münch, A., Please, C. P. & Wagner, B. Spin coating of an evaporating polymer solution. *Physics of Fluids* **23**, 102101 (2011).

49. Brookshier, M. A., Chusuei, C. C. & Goodman, D. W. Control of CuO Particle Size on SiO2 by Spin Coating. *Langmuir* **15**, 2043–2046 (1999).

50. Berg, J. K., Weber, C. M. & Riegler, H. Impact of Negative Line Tension on the Shape of Nanometer-Size Sessile Droplets. *Phys. Rev. Lett.* **105**, 076103 (2010).

51. Emslie, A. G., Bonner, F. T. & Peck, L. G. Flow of a Viscous Liquid on a Rotating Disk. *Journal of Applied Physics* **29**, 858–862 (1958).

52. Acrivos, A., Shah, M. J. & Petersen, E. E. On the Flow of a Non□Newtonian Liquid on a Rotating Disk. *Journal of Applied Physics* **31**, 963–968 (1960).

53. Meyerhofer, D. Characteristics of resist films produced by spinning. *Journal of Applied Physics* **49**, 3993–3997 (1978).

54. Sukanek, P. C. Dependence of Film Thickness on Speed in Spin Coating. *J. Electrochem. Soc.* **138**, 1712–1719 (1991).

55. Lawrence, C. J. Spin coating with slow evaporation. *Physics of Fluids A: Fluid Dynamics* **2**, 453 (1990).

56. Flack, W. W., Soong, D. S., Bell, A. T. & Hess, D. W. A mathematical model for spin coating of polymer resists. *Journal of Applied Physics* **56**, 1199–1206 (1984).

57. Tsamopoulos, J. A., Chen, M. E. & Borkar, A. V. On the spin coating of viscoplastic fluids. *Rheologica Acta* **35**, 597–615 (1996).

58. Parmar, N. H., Tirumkudulu, M. S. & Hinch, E. J. Coating flow of viscous Newtonian liquids on a rotating vertical disk. *Physics of Fluids* **21**, 103102 (2009).

59. Ohara, T., Matsumoto, Y. & Ohashi, H. The film formation dynamics in spin coating. *Physics of Fluids A: Fluid Dynamics* **1**, 1949 (1989).

60. Schubert, D. W. & Dunkel, T. Spin coating from a molecular point of view: its concentration regimes, influence of molar mass and distribution. *Materials Research Innovations* **7**, 314–321 (2003).

61. Bornside, D. E., Macosko, C. W. & Scriven, L. E. Spin coating: One-dimensional model. *Journal of Applied Physics* **66**, 5185–5193 (1989).

62. Sparrow, E. M. & Gregg, J. L. Mass transfer, flow, and heat transfer about a rotating disk. *Journal of Heat Transfer* **82**, 294–302 (1960).

63. Karpitschka, S., Weber, C. M. & Riegler, H. Controlling Supersturation near Interfaces: Physics of Spin-Coating Small Molecules from Dilute Solutions. *to be submitted*

64. Bezmel'nitsyn, V. N., Eletskii, A. V. & Okun', M. V. Fullerenes in solutions. *Physics-Uspekhi* **41**, 1091–1114 (1998).

65. Einstein, A. Über die von der molekularkinetischen Theorie der Wärme geforderte Bewegung von in ruhenden Flüssigkeiten suspendierten Teilchen. *Annalen der Physik* **322**, 549–560 (1905).

66. Young, T. An Essay on the Cohesion of Fluids. *Phil. Trans. R. Soc. Lond.* **95**, 65–87 (1805).

67. Israelachvili, J. N. *Intermolecular and Surface Forces*. (Academic Press: 2011).

68. Dai, B., Leal, L. G. & Redondo, A. Disjoining pressure for nonuniform thin films. *Phys. Rev. E* **78**, 061602 (2008).

69. Overbeek J.Th.G. Interparticle forces in colloid science. *Powder Technology* **37**, 195–208 (1984).

70. Israelachvili, J. N. van der Waals dispersion force contribution to works of adhesion and contact angles on the basis of macroscopic theory. *J. Chem. Soc., Faraday Trans. 2* **69**, 1729–1738 (1973).

71. Gibbs, J. W., Bumstead, H. A., Van Name, R. G. & Longley, W. R. *The collected works of J. Willard Gibbs*. (Longmans, Green and Co.: 1902).at <http://books.google.de/books?id=xCJWAAAAMAAJ>

72. Mclaughlin, B. . & De Bruyn, P. . The dynamics and thermodynamics of solid-fluid-fluid three-phase contact. *Journal of Colloid and Interface Science* **30**, 21–33 (1969).

73. Gaydos, J. & Neumann, A. W. The dependence of contact angles on drop size and line tension. *Journal of Colloid and Interface Science* **120**, 76–86 (1987).

74. Auer, S. & Frenkel, D. Line Tension Controls Wall-Induced Crystal Nucleation in Hard-Sphere Colloids. *Phys. Rev. Lett.* **91**, 015703 (2003).

75. Schmidt, V., Senz, S. & Gösele, U. Diameter-Dependent Growth Direction of Epitaxial Silicon Nanowires. *Nano Lett.* **5**, 931–935 (2005).

76. Wang, J. Y., Betelu, S. & Law, B. M. Line tension approaching a first-order wetting transition: Experimental results from contact angle measurements. *Phys. Rev. E* **63**, 031601 (2001).

77. Pompe, T. & Herminghaus, S. Three-Phase Contact Line Energetics from Nanoscale Liquid Surface Topographies. *Phys. Rev. Lett.* **85**, 1930–1933 (2000).

78. Winter, D., Virnau, P. & Binder, K. Monte Carlo Test of the Classical Theory for Heterogeneous Nucleation Barriers. *Phys. Rev. Lett.* **103**, 225703 (2009).

79. Vandecan, Y. & Indekeu, J. O. Theoretical study of the three-phase contact line and its tension in adsorbed colloid-polymer mixtures. *The Journal of Chemical Physics* **128**, 104902–104902–5 (2008).

80. De Feijter, J. A. & Vrij, A. I. Transition regions, line tensions and contact angles in soap films. *Journal of Electroanalytical Chemistry and Interfacial Electrochemistry* **37**, 9–22 (1972).

81. Baumgart, T., Hess, S. T. & Webb, W. W. Imaging coexisting fluid domains in biomembrane models coupling curvature and line tension. *Nature* **425**, 821–824 (2003).

82. Lipowsky, R. Budding of membranes induced by intramembrane domains. *Journal de Physique II* **2**, 16 (1992).

83. Schimmele, L., Napiórkowski, M. & Dietrich, S. Conceptual aspects of line tensions. *The Journal of Chemical Physics* **127**, 164715 (2007).

84. Getta, T. & Dietrich, S. Line tension between fluid phases and a substrate. *Phys. Rev. E* **57**, 655 (1998).

85. Pompe, T. Line Tension Behavior of a First-Order Wetting System. *Phys. Rev. Lett.* **89**, 076102 (2002).

86. Wu, Q. & Wong, H. A Slope-Dependent Disjoining Pressure for Non-Zero Contact Angles. *Journal of Fluid Mechanics* **506**, 157–185 (2004).

87. J., V. On Hamaker constants: A comparison between Hamaker constants and Lifshitz-van der Waals constants. *Advances in Colloid and Interface Science* **3**, 331–363 (1972).

88. Milchev, A., Milchev, A. & Binder, K. Nanodroplets on a solid plane: wetting and spreading in a Monte Carlo simulation. *Computer Physics Communications* **146**, 38–53 (2002).

89. Yusuke, T. *et al.* Surface free energy and wettability determination of various fullerene derivative films on amorphous carbon wafer. *Japanese Journal of Applied Physics* **47**, 5730–5733 (2008).

90. Gilmer, G. H. & Bennema, P. Computer simulation of crystal surface structure and growth kinetics. *Journal of Crystal Growth* **13-14**, 148–153 (1972).

91. Kulmala, M. How Particles Nucleate and Grow. *Science* **302**, 1000–1001 (2003).

92. Winkler, P. M. *et al.* Heterogeneous Nucleation Experiments Bridging the Scale from Molecular Ion Clusters to Nanoparticles. *Science* **319**, 1374–1377 (2008).

93. Ramaswamy, V. *et al.* Synthesis of Nearly Monodisperse Embedded Nanoparticles by Separating Nucleation and Growth in Ion Implantation. *Nano Lett.* **5**, 373–377 (2005).

94. Mitchell, C. A., Yu, L. & Ward, M. D. Selective Nucleation and Discovery of Organic Polymorphs through Epitaxy with Single Crystal Substrates. *J. Am. Chem. Soc.* **123**, 10830–10839 (2001).

95. Benton, W. J., Collins, I. R., Grimsey, I. M., Parkinson, G. M. & Rodger, S. A. Nucleation, growth and inhibition of barium sulfate-controlled modification with organic and inorganic additives. *Faraday Discussions* **95**, 281 (1993).

96. Ludwig, A., Wagner, I., Laakmann, J. & Sahm, P. R. Undercooling of superalloy melts: basis of a new manufacturing technique for single-crystal turbine blades. *Materials Science and Engineering: A* **178**, 299–303 (1994).

97. Du, N., Liu, X. Y. & Hew, C. L. Ice Nucleation Inhibition: Mechanism of Antifreeze by Antifreeze Protein. *J. Biol. Chem.* **278**, 36000–36004 (2003).

98. Raymond, J. A., Wilson, P. & DeVries, A. L. Inhibition of Growth of Nonbasal Planes in Ice by Fish Antifreezes. *PNAS* **86**, 881–885 (1989).

99. Page, A. J. & Sear, R. P. Heterogeneous Nucleation in and out of Pores. *Phys. Rev. Lett.* **97**, 065701 (2006).

Acknowledgement

This thesis would not have been possible without the contributions of so many people.

First I would like to thank Prof. Helmut Möhwald for the opportunity to perform this thesis at his department. I very much enjoyed the scientific and personal atmosphere at the institute.

I would like to thank my supervisor Dr. Hans Riegler for his time and support. I very much appreciate his broad mind and his attitude to question the obvious.

I would like to thank the IGRTG 1524 for the founding and in particular the members Prof. Regine von Klitzing, Prof. Martin Schoen, Daniela Fliegner and Petra Erdmann for the support. Furthermore I am very grateful to Prof. Richard Spontak who allowed me to visit his group at the North Carolina State University and to learn a lot on electron microscopy.

I thank Stefan Karpitschka for his constant willingness to solve mathematical problems as well as Andreas Vetter and John Berg for the good collaboration for the simulation. Last but not least I want to thank all group members, colleagues and the technicians for the good and productive time I had at the Max Planck Institute for Colloid and Interfaces Sciences.